Soft Inflatable Robots for Safe Physical Human Interaction

Siddharth Sanan

CMU-RI-TR-13-23

Submitted in partial fulfillment of the requirements for the degree of Doctor of Philosophy in Robotics

THE ROBOTICS INSTITUTE
CARNEGIE MELLON UNIVERSITY
PITTSBURGH, PENNSYLVANIA 15213

August, 2013

Thesis Committee:
Christopher G. Atkeson (Chair)
Howie Choset
Steven H. Collins
J. Edward Colgate, Northwestern University

To my parents,

Neeta and Sammi Sushil Sanan

Abstract

Robots that can operate in human environments in a safe and robust manner would be of great benefit to society, due to their immense potential for providing assistance to humans. However, robots have seen limited application outside of the industrial setting in environments such as homes and hospitals. We believe a very important factor preventing the cross over of robotic technology from the factory to the house is the issue of safety. The safety issue is usually bypassed in the industrial setting by separation of human and robot workspaces. Such a solution is clearly infeasible for robots that provide assistance to humans. This thesis aims to develop intrinsically safe robots that are suitable for providing assistance to humans.

We believe *intrinsic* safety is important in physical human robot interaction because unintended interactions *will* occur between humans and robots due to: (a) sharing of workspace, (b) hardware failure (computer crashes, actuator failures), (c) limitations on perception, and (d) limitations on cognition. When such unintended interactions are very fast (collisions), they are beyond the bandwidth limits of practical controllers and only the intrinsic safety characteristics of the system govern the interaction forces that occur. The effects of such interactions with traditional robots could range from persistent discomfort to bone fracture to even serious injuries. Therefore robots that serve in the application domain of human assistance should be able to function with a high tolerance for unintended interactions. This calls for a new design paradigm where operational safety is the primary concern and task accuracy/precision though important are secondary.

In this thesis, we address this new design paradigm by developing robots that have a soft inflat-

able structure, i.e, inflatable robots. Inflatable robots can improve intrinsic safety characteristics by being extremely lightweight and by including surface compliance (due to the compressibility of air) as well as distributed structural compliance (due to the lower Young's modulus of the materials used) in the structure. This results in a lower effective inertia during collisions which implies a lower impact force between the inflatable robot and human. Inflatable robots can essentially be manufactured like clothes and can therefore also potentially lower the cost of robots to an extent where personal robots can be an affordable reality.

In this thesis, we present a number of inflatable robot prototypes to address challenges in the area of design and control of such systems. Specific areas addressed are: structural and joint design, payload capacity, pneumatic actuation, state estimation and control. The CMU inflatable arm is used in tasks like wiping and feeding a human to successfully demonstrate the use of inflatable robots for tasks involving close physical human interaction.

Acknowledgements

I would like to thank my advisor, Chris Atkeson, for all the support and guidance he has provided during my thesis work. He has been a constant source of inspiration throughout the work presented in this thesis and to me as a roboticist. I would also like to thank my thesis committee members, Howie Choset, Steve Collins and Ed Colgate (Northwestern) for their insightful questions and advice during my thesis research.

I would like to thank everyone at the Quality of Life Technology Center (QoLT) for supporting the work in this thesis from its very beginnings and for all the other enriching experiences I have had because of QoLT. I would also like to thank my external collaborators, Pete Lynn and Saul Griffith at Otherlab, and Annan Mozeika at iRobot for specific work in this thesis that was carried out with their help.

Thank you to Mike Ornstein, Alex Kan May and Justin Moidel for spending their summers in the lab and helping with so much of the intricate work that has gone into making inflatable robots a reality. I would also like to thank all my friends at CMU and lab-mates at the CGA lab. Its been fun learning so much from all of you.

I would also like to thank my advisors prior to joining CMU, G.K. Ananthasuresh (IISc), Madhava Krishna (IIIT) and Sartaj Singh (CAIR) for guiding me when I was a budding researcher. Thank you to my friends at Manipal for being the team that we were.

Thank you to my fiancée, Gracee Agrawal, for her love and support through the years. I could not have made it without you. Thank you to my parents, Neeta and Sammi Sanan, for always supporting me and encouraging me to follow my dreams and passions. Thank you for everything.

Contents

Chapter 1

Introduction

The use of robots in assistive roles will be an increasingly significant application for robotics. The application of robots in these roles has unique demands from a mechanical and control design perspective, which have not been thoroughly addressed in the past. Safety, as stated by [3], is of prime importance when humans are involved. The paradigm shift thus needed in the way we design robots is a unique departure from the way humans have thought about machines in the past. The robot must minimize the risk of injury to others during its operation. This thesis deals with the development of soft inflatable robots that for providing assistance to humans.

1.1 Motivation

Robots designed and controlled with a traditional approach that stems from industrial automation may not be the best answer to robots in human environments. These robots are often designed with the objective of improving accuracy of the system. This demand for functional performance has lead most robots to have rigid links and high stiffness, in part due to the availability of accurate modeling techniques, advanced control methods and simple mechanical design techniques for rigid body systems. Due to this, the approach towards human safety in the presence of robots has largely

involved the use of segregation methods to keep human and robots in non-intersecting workspaces. However, this approach fails when humans and robots need to work in physically close spaces, such as in tasks involving robots assisting humans. New approaches in the design and control of robots need to be developed which incorporate the shift from performance oriented systems to safe systems, needed for robots in human environments.

A large proportion of prior research related to improving characteristics of human robot interaction has been devoted to compliant control of robots. Compliant control of robot manipulators [46, 89] aims to reduce the impedance of the robot as seen from the contact end. However, limitations due to the bandwidth of the controller prohibit impedance control at high frequencies. This limitation is a crucial drawback from the standpoint of safety in physical human robot interaction (pHRI). Impacts are a primary risk in pHRI , and the interaction during impacts is at high frequencies. Without impedance control at high frequencies, the interaction between human and robot cannot be controlled during impacts. This leads to a very high risk situation. The interaction at higher frequencies is therefore mostly dependent on the open loop (uncontrolled) characteristics of any practical robot manipulator. Safety that is independent of the control scheme, is referred to as *intrinsic* or *inherent safety*. Besides the finite control bandwidth issue, inherent safety is also necessary in the event of control failure, hardware failure and other such malfunction that can easily occur in a complex system.

As described in [137, 8], compliance in a system improves the open loop characteristics needed for safety by reducing the reflected inertia on the contact side of the impact.The reflected inertia at the contact end can be modified in a number of ways, albeit with different performance characteristics: (a) the mass of the entire system can be reduced, (b) the overall stiffness of the system can be reduced, i.e., some form of additional compliance, e.g., a soft covering can be introduced, (c) the mass distribution within the system can be modified, and (d) the stiffness distribution within the system can be modified. Robots that utilize soft and inflatable structures can embody these principles well and can lead to systems that are extremely safe.

1.2 Challenges

While the safety of inflatable robots is intuitive, inflatable robots present a number of other challenges in their development and use. This thesis addresses a number of these challenges that exist towards realizing inflatable robots for safe physical human interaction.

Design for safety and performance

Clearly, soft robots can satisfy safety requirements that are needed for working in close proximity to humans. The question that needs to be answered then is: how do we design a soft robot that is also functional? Are traditional static design requirements such as payload capacity, manipulability etc. enough? Often soft systems can be engineered practically never fail, e.g., a soft jelly fish like robot can be repeatedly smashed without incurring any damage at all. What should guide the design in such a case? In Chapter 3, we discuss various design paradigms for soft and safe robots. We also seek to develop a framework that can be used to synthesize the design of soft robots.

Strength

One of the main challenges has been to show that inflatable robot which are safe and light can actually have a usable payload capacity while still having a large range-of-motion. This problem is different from static inflatable structures that maintain their shape once inflated, which are often employed in architectural and space applications. Chapter 6 addresses issues in developing high strength inflatable robots and successfully demonstrates these capabilities using a prototype inflatable robot that has a payload to weight ratio of 2.5 and an absolute payload of 2.25 kg.

Motion

Inflatable robots, unlike static inflatable structures, require motion across the inflatable structure. This presents a challenge because mechanisms or joints need to be developed and realized that

can allow motion across the structure. Additionally, actuation techniques that can provide motive force across the joints are needed. Various types of joints and actuation techniques have been explored and developed in this thesis that address these need. As a result, inflatable structures with large range of motion ($> 300^{\circ}$) have been successfully realized. Chapter 6, 4 and 7 discuss the developments made with regards to actuators and joints.

Accuracy

A number of challenges exist with regards to developing inflatable robots that are also accurate in a position control sense. Because inflatable robots by definition have no rigid joints, accurate joint angle measurement is a challenge. Another challenge is the dependence of the motion of inflatable robots on the structural deformation models. In chapter 8, we address issues in sensing, estimation and model dependent kinematics for inflatable robots.

1.3 Thesis Outline

The outline of this document is as follows. Chapter 2 describes related work: safety metrics, impact modeling, compliant control, robust control and reaction strategies and flexible robots. Chapter 3 describes design issues for developing safe and robots. Chapter 4 describes the inflatable manipulator prototypes that were realized and utilized as part of this thesis. Chapter 6 describes advancements made to develop high strength inflatable robots. Chapter 7 describes developments made in the area of pneumatic actuators for inflatable robots. Chapter 8 describes models, model based algorithms and sensing and estimation work to improve the accuracy of motion of inflatable robots. Chapter 9 describes experiments and examples of the inflatable robots carrying out task involving human interaction.

Chapter 2

Background

The problem of designing and controlling a robotic system for safe operation in human environments requires knowledge from many areas including biomechanics, impact mechanics, compliant control, robust control, smart materials and flexible robots. These are briefly described in this chapter. Additionally some foundational work carried out towards developing soft robots for human interaction is described. The continuum arm, which belongs to a different class of soft robots than inflatable robots is described. Force control experiments with a single link inflatable robot are also presented.

2.1 Injury Modes

During physical human robot interaction injury can occur via a variety of mechanisms. They include quasi-static loading, dynamic loading and other mechanisms such as shearing and puncturing.

2.1.1 Quasi-Static Loading

When the interaction forces between the robot and human change slowly such loading is referred to as quasi-static loading. The injuries possible due to quasi-static interactions include fractures and soft tissue injuries [40]. This loading situation is relatively simple in terms of its description and effect on the two interacting bodies.

Compliant control, which is discussed in sec. 2.3, is useful in limiting contact forces and preventing injuries due to quasi-static loading. However, as tactile sensing has not completely matured as a technology, quasi-static loading still poses a some level of risk in pHRI. Measures to improve safety against quasi-static loading, besides compliant control, include limiting the actuation force/torque at the joints and limiting the workspace of the manipulator based on its contact Jacobian.

2.1.2 Dynamic Loading

Dynamic loading refers to the condition where the interaction forces between the robot and the human vary over a short time scale. Collisions or impacts are the most common form of dynamic loading. Injuries possible due to such loading have been detailed by Haddadin et al. [40]. Injuries include fractures, internal injuries and soft tissue injuries. It is reasonable to assume that the human is fixed (constrained) at all times during the interaction, as this is the situation which poses the maximum risk of injury [40] and hence any injury analysis based on this assumption is conservative.

Impacts between two bodies can be analyzed in a number of ways, depending on the characteristics of the two bodies. Stronge [112] provides basic classifications based on the nature of the two bodies involved in the impact. It must be noted that we will be dealing with impacts that are considered relatively low speed ($\approx$ 1 m/s). This implies that in most cases plastic flow in the two interacting bodies does not occur. In situations such as a bullet penetrating a human body, plastic

flow does occur and an impact theory for high speed collisions is needed. Gilardi and Sharf [32] provide a recent review of impact modeling of impacts. Essentially, two kinds of models exist for impact: 1) Discrete models and 2) Continuous models. The discrete models such as the Newton's model [81] utilize an instantaneous change in velocities of the impacting bodies, while continuous models such as the spring-dashpot model [35] utilize interaction force models during the contact period to propagate the dynamics of the system through the impact phase. For the most part, we shall utilize continuous models in this thesis.

We often use flexible structures like flexible links. Modeling and analysis of impacts with flexible bodies is therefore important. Khulief and Shabana [60] compare the accuracy of lumped mass versus consistent mass modeling techniques for flexible bodies undergoing impact. Other researches have studied the dynamics of flexible links with impact [134, 135, 128].

2.1.3 Other Injury Mechanisms

Shearing

Shearing refers to the case where in the human comes in contact with a sharp edge of the robot. Such a scenario is possible when the robot is utilizing a sharp tool as an end effector. This injury mechanism can cause lacerations, and penetration of the human skin and soft tissue. Data regarding forces and parameters of the tool needed to causes such injuries is available in literature [42, 71, 72, 84, 34, 33]. Preventing injuries in such scenarios is a major challenge since the robot is inherently unsafe when equipped with a sharp tool.

Puncturing

Puncturing occurs when the human comes into point contact with an external object. Such an interaction is possible if there are sharp corners on the robot or the robot is carrying a pointed object such as a nail. Wounds caused by puncturing are very similar to those caused due to shearing.

Abrasion

Relative motion of a rough surface with human skin can lead to injury due to abrasion. Abrasion causes superficial damage to the skin.

2.2 Safety Indices

A safety index is used to quantify the severity of an interaction (impact, quasi-static) between a human and any external agent. In our case, the robot is the external agent. The safety index can then be mapped to the level of injury caused in the human subject. We shall limit our discussion of safety indices to impacts only as we hope to address impact safety. When the interaction is quasi-static, the interaction force between the human subject and robot can be used directly to evaluate safety of interaction. Research in finding an appropriate safety index in pHRI is still an ongoing area of research, with only a few published results [40, 83].

2.2.1 The Head Injury Criterion (HIC)

The most commonly used quantification of severity of interaction during impacts is the Head Injury Criterion (HIC)[123]. The HIC is defined mathematically as:

$$\text{HIC} = T\left[\frac{1}{T}\int_{t_1}^{t_2} a(\tau)\,d\tau\right]^{2.5} \tag{2.1}$$

where a is head acceleration measured in g, and $T = t_2 - t_1$ is the duration of the impact. As the duration of impact T is hard to measure, the interval of integration is varied to obtain the worst case HIC. Typically, t_2 is the time when the head reaches the maximum acceleration. The HIC is mapped to a particular injury level or the probability of injury level using the Abbreviated Injury Scale (AIS) and the European New Car Assessment Programme (EuroN-CAP)[40]. An HIC level below 650 is considered to have a very low risk ($< 5\%$) of serious injury (AIS≥ 3).

The HIC was formulated to measure impact severity in the case of indirect interaction, such as that in an automobile crash. The impact scenario in an automobile crash is very different from an impact scenario with a robot manipulator. In an automobile crash an external agent impacts the automobile, in which the subject is placed, which causes large accelerations of the head. The duration and magnitude of the these accelerations are measured by the HIC. Therefore, the HIC is a good indicator for internal injuries, such as brain hemorrhage. However, effects such as those caused by direct interaction between the agent and the subject in an impact situation are ignored by the HIC. Such interactions are likely in a human-robot impact situation. These direct interactions can cause injuries such as fracturing of bones and soft tissue injuries. The HIC has been used in the past [8, 137] to speak about injury potential in pHRI, but its use has been largely limited in lieu of results demonstrating its inappropriateness for pHRI [40].

2.2.2 Contact Force

Measurements such as the contact force F_{ext} are deemed more suitable to types of injuries possible in human robot interaction. The time history of contact force between a subject and an external agent yields important information regarding the possibility of injuries like bone fractures. Bone fractures are an instance of mechanical failure of the bone leading to the formation of a crack in the bone or complete separation of the bone into two or more pieces. When the contact force exerted on a particular bone exceeds its sustainable limit, the bone fractures due to the development of stresses in the material beyond the safe value. It must be noted that along with magnitude of the maximum contact force F_{max}, the time period of loading t_{max}, shown in Fig 2.1, is also an important feature of the interaction. If t_{max} is large the loading can be considered quasi-static, if t_{max} is small the loading can be treated as an impact. High rates of loading, which usually occur in impacts between two hard objects, cause brittle behavior in the materials. This causes failure of the object via *brittle fracture* at stresses below quasi-static limits. At short time scales materials are more brittle than on long time scales. Therefore to reduce the risk of bone fracture it is useful to

attenuate the maximum contact force and also decrease the rate of loading. Reducing the loading rate also has advantages from the viewpoint of control, as it may sufficiently slow down the contact forces so that they remain within the controller bandwidth.

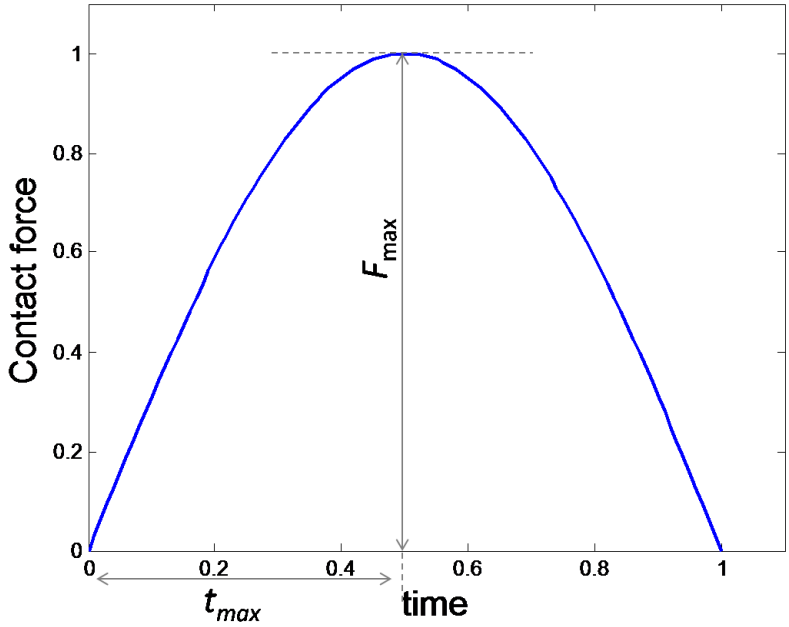

Figure 2.1: Contact Force Parameters: Maximum Force F_{max} and time period of loading t_{max}.

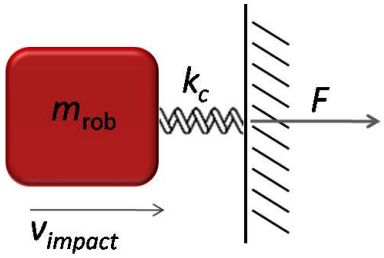

Figure 2.2: A single mass system with mass m_{rob} and contact stiffness k_c moving at velocity v_{impact} colliding with a static object

For any safety index, given the structure of the robot and certain assumptions about the human subject, it is possible to map the safety index to some state of the robot. For simple systems this can be done analytically while for more complex systems experimental and computational procedures can be used to relate the states of the system to the safety index. As an example the maximum

contact force for the single mass system , shown in Fig. 2.2, of mass m_{rob} with a contact stiffness k_c colliding with a static object at a velocity v_{impact} is given by [116]:

$$\begin{aligned} F_{max} &= m_{rob}\omega_n^2\sqrt{\frac{v_{impact}^2}{\omega_n^2}} \\ &= \omega_n m_{rob} v_{impact} \\ \text{where, } \omega_n &= \sqrt{\frac{k_c}{m_{rob}}} \end{aligned} \tag{2.2}$$

From (2.2), it can be seen for a simple single mass system the maximum force exerted is proportional to the momentum of the system and its natural frequency. Such simple relations allow the formulation of simple constraints on the states of the system (in this case the velocity of the system) in terms of the safety index (the maximum allowable force in this case). We shall base most of our future discussion of safety on the safety metric of maximum contact force during an interaction.

The mass that directly interacts with an external agent (m_{rob} in Fig. 2.2) via any intermediate non-dynamic elements (k_c in Fig. 2.2) is also known as the unsprung mass.

The fracture characteristics for various bones has been investigated previously [74, 31, 1, 2]. Data from these experiments allow us to set conservative limits based on worst case scenarios for maximum allowable contact forces between the robot and the subject.

2.3 Compliant Control

Compliant control or force control deals with controlling the interaction forces/torques between a manipulator and its environment during intended contact. Under compliant control the robot typically adapts its actions to maintain desired contact forces with the environment, in this sense the robot *complies* with its environment. It is easy to observe that such type of control is essen-

tial for tasks involving physical human robot interaction. In the context of pHRI, tasks such as hand shakes, haptic teleoperation, payload assistance, or any task involving physical co-operation between human and robot must utilize some form of compliant control for safe and effective execution.

There are a number of techniques for force control which involve controlling the compliance, impedance or admittance of the robot to achieve desired force interaction characteristics. While other force control techniques explicitly involve a force feedback loop to control the interaction forces. Thorough reviews of these techniques are available [124, 49, 129].

The techniques for force control can be used to realize compliant behaviors to limit injury risks due to quasi-static loading discussed in Sec. 2.1.1. However the limited control bandwidth decreases its usefulness towards reducing risks due to dynamic loading discussed in 2.1.2

2.4 Flexible Robots

Considering limitations in the bandwidth of active force control [26], it is necessary to improve the open loop characteristics of the systems. One of the methods of doing this, is by the introduction of flexible elements in the robot. A brief survey of various cases of robot flexibility follows.

2.4.1 Soft Coverings

Soft coverings constitute the most basic type of compliance that can be introduced to a robot structure. The robot is simply padded with soft material such as silicone, rubber etc. to introduce compliance into the system. Robots like the RI-MAN [78] utilize such soft coverings to improve interaction characteristics.

Various contact models have been derived that relate the material properties of the covering and the geometry of the contacting object to a stiffness value for the covering [58, 56]. These models can be used to select materials and material thicknesses based on desired contact stiffness.

2.4.2 Flexible Joints

Joints with flexibility or compliance geometrically collocated with the joint axis are known as flexible joints. Robots with such flexible joints have compliance concentrated at isolated locations on its structure. This is the most common type of flexibility encountered in robots, due to transmission elements such as harmonic drives, cables, gears etc. Flexible joints have also been received considerable attention recently for the development of inherently safe robots.

The Series Elastic Actuator (SEA) [90] was developed to reduce the impedance of stiff actuators by introducing compliance between the link and the actuator. The SEA can be considered to be a case of designed joint flexibility. Improving on the performance limitations posed by SEA, recently [137, 98] introduced flexibility in the joints to improve safety characteristics of robots involved in pHRI. The joint flexibility allows inertial decoupling between the actuator and the link during impacts [41].

Flexible joints with constant joint compliance, while reducing output impedance at high frequencies, do result in performance deterioration in tasks such as high speed trajectory following. The high frequency torque from the actuator to the link falls off with increasing frequency [137]. Citing this and other performance limitation using constant joint compliance, many researchers have proposed the use of variable impedance actuators (VIA) [119, 98, 131, 53, 121]. These actuators allow the mechanical compliance of the actuator to be varied in accordance with the need of the task. In the context of pHRI, Bicchi and Tonietti [8] proposed an optimization scheme to compute the optimal desired stiffness trajectory for a minimum time maneuver of a linear system with safety constraints.

The dynamic model for robots with flexible joints is twice the order of an identical system with ideal joints. For example, assuming a planar serial manipulator with all flexible revolute joints, if N is the number of links and there are N joints, then the total mechanical degrees of freedom of the system is $2N$ while the number of actuators are N. As a result such systems are underactuated.

2.4.3 Flexible Links

Besides flexibility at the joints, a robot manipulator may also have flexibility distributed throughout the length of its links. Link flexibility can be thought of as a more general case of flexible joints. In the past, flexible links have been studied in cases where it is impossible to eliminate link flexibility due to specific requirements of the task. Space applications and confined operational environments often present design constraints which make link flexibility unavoidable. In this thesis, the usefulness of link flexibility in the context of pHRI will be demonstrated. We look at link flexibility as a blessing rather than a curse.

Dynamic models for flexible manipulators have been researched in the past. Shabana [101], Dwivedy and Eberhard [25], Robinett et al. [92] and Tokhi and Azad [118] provide thorough overviews of the techniques developed to model systems with flexible components. The most popular techniques used to model system including link flexibility are the finite segment approach [54, 99], assumed modes method (AMM) [11, 127, 45] and the finite element method (FEM)[117, 75, 9, 79].

The finite segment or lumped parameter approach treats the flexible links as a collection of the rigid bodies connected by elastic elements and/or dampers. In the assumed modes method (AMM) displacements along the length of a flexible link are represented as a truncated series of the spatial modal functions and time varying modal amplitude. In most cases, the mode shapes are computed from the partial differential equations (PDE) for the unforced vibrations of the link. When this is not possible (due to complicated link geometry), approximate mode shapes computed using static deflections may be used. The finite element method models each link as an assembly of elements whose displacements are compatible at the boundaries. The elastic displacements of the link are represented by the nodal displacement values of the elements. The nodal displacements are interpolated within an element by the use of predefined shape functions. The shape functions are usually chosen to be polynomial in the nodal displacements for ease of integration.

The AMM is well suited to manipulators involving only a single flexible link and simple link

geometries. For the case of multi-linked flexible manipulator the finite element approach may be better suited. An extensive comparison of the two approaches is available([115]). From the purpose of simplicity the lumped parameter approach is the easiest to analyze, as it permits the use of the vast number of tools developed for rigid multi-body systems. It may therefore be the most suited for controller synthesis. It should be noted that in the context of flexible multi-body systems FEM and AMM have been applied mostly in the linear deflection regime only, the finite segment approach allows the inclusion of geometric nonlinear deflections.

The use of flexible links introduces a variety of challenging control problems. The reasons for this is the non-minimum phase behavior of such systems and difficulty in obtaining full state feedback. A major cause of concern is the issue of vibrations when flexible links are utilized. One strategy is to modify the input command to the system based on knowledge of the certain parameters of the system to minimize vibrations in the system. The Input Shaping technique [106, 108] utilizes this idea. Feedback methods based on estimating link deflections using sensory data from strain gauges placed along the length of the arm may also be used ([44, 136]). These sensors can be placed such that they are nearly collocated with the actuator. Tip position data may also be obtained using optical sensing/vision and utilized in the feedback control scheme . Such sensing is non-collocated and therefore stability issues may arise [11]. A variety of other specialized techniques to control flexible manipulators exists, Robinett et al. [92] and Tokhi and Azad [118] provide a detailed account of these.

2.4.4 Continuum Robots

Continuum robots are robots that consist of a continuous *backbone* and move via deformation of this backbone. No kinematic joints are present on the structure. This class of robots utilizes hyper-elastic structures that can tolerate large deformations. Other terminologies often used to describe such robots are: snake robots, elephant trunk robot, tentacle robots etc. Like robots with flexible links these systems possess distributed compliance all throughout their structure, however unlike

flexible link robots they utilize compliance to achieve motion as well. The distributed nature of the motion and compliance in the system can offer distinct advantages for safe physical human interaction.

A number of continuum robots have been designed in the past [114, 36, 73, 48, 105]. [93] provides a review of some of the efforts in realizing continuum robots. Most continuum systems are actuated either by the use of remotely actuated tendons [36, 105] or by the use of pneumatic actuators [114, 73, 48]. These actuators modify the shape of the robot by application of geometric constraints on the structure. Inspiration from biological systems such as elephant trunks and octopus tentacles have driven the design of these systems. The primary motivation is applications involving convoluted spaces, whole arm manipulation and locomotion.

Theoretically continuum robots posses infinite degrees of freedom. However, only a few of the DoF's are usually actively controlled. Therefore continuum robots may be underactuated. There are also example systems which approximate continuum systems by using a large number of rigid links thus making them very large but finite DoF systems [130, 17, 43, 86]. The infinite degrees of freedom in continuum robots pose interesting challenges in their modeling. A significant portion of research has focussed on modeling continuum robots from the kinematics and dynamics perspective. Chirikjian and Burdick [15] provide a modal approach to formulate the kinematics for hyper-redundant robots. Some of the results from this work are directly applicable to continuum robots. Gravagne and Walker [38, 37] address the kinematics of multi-section remotely actuated continuum robots. Simaan et al. [105] provide a kinematic formulation, based on the reasonable assumptions noted by Gravagne and Walker [38], for a snake like arm with secondary backbones functioning as push-pull tendons. Dynamic models for continuum robots using a continuum mechanics formulation were explored by Chirikjian [14]. [126] provides a general overview of design and motion planning issues for continuum robots and their discrete approximations.

2.4.5 Inflatable Robots

An inflatable structure refers to a structure that is made using membrane material (can only hold tensile stress) and maintains structural integrity by virtue of internal pressure. Such structures are a special case of a class of structures known as *membrane structures*. Based on the method of pressurization, inflatable structures using air can be classified as either (a) air supported or (b) air inflated. Air supported structures commonly utilize a small pressure differential between internal and external pressure and are continuously replenished with air as they are usually open structures. Examples include inflatable roofs and other inflatable structures used in entertainment. Air inflated structures consist of pneumatically closed structures that are inflated to any desired pressure above the external pressure. Unlike air supported structure continuous replenishment of air is not needed and therefore higher pressure differentials can be generated between the internal and external pressures. Examples include inflatable space structures, inflatable wings, inflatable tents, inflatable toys, etc.

Use of inflatable links instead of traditional rigid metallic links can help incorporate the design paradigms listed Sec. 3.1. They can be potentially extremely lightweight, have low contact stiffness (due to the compressibility of air) and also possess distributed compliance due to the relatively higher elasticity of the materials used to make these links as compared to aluminium or other conventional metals. In addition, there are also numerous other possibilities using inflatable structures such as good post-buckling characteristics which is not available from conventional robot materials. Other advantages of inflatable structures include collapsibility (deployable) and low cost. Multiple links offer a feasible way to generate multi-DoF systems using inflatable structures. In such a configuration, interesting opportunities and challenges present themselves regarding the joints that connect the multiple links. Traditional bearing based joint designs are often heavy and can therefore adversely affect payload capacities of the structure. Fortunately, it is possible to utilize inflatable structures that allow relative motion between different section of the structure. In Chapter 4 we describe a number of realizations of such inflatable structures.

Besides this thesis, other prior attempts to utilize inflatable structures in robot manipulators have been made. Most notably in the early 1980s, [5] built a manipulator consisting of a single inflatable link with pneumatic actuators along its length that caused bending of the link in multiple directions. [94] appended a traditional rigid robot manipulator (PUMA) with an inflatable link at the distal end and presented an analysis of this system. More recent attempts have been also been made to build inflatable manipulators using pneumatic actuation [69]. [125] developed a novel constant volume joint for inflatable robots. These efforts suggest the applicability of inflatable structures for robot manipulators, however, they represent only a preliminary exploration of the design space of such robots.

2.5 The Continuum Arm

The continuum arm is a continuum robot and belongs to the category of C1 manipulators described in 3.2.1. This section details our work with such a system.

2.5.1 System Description

Fig. 2.3 shows an image of the continuum arm prototyped in our lab. We will refer to the moving section of the robot as the robot arm and the stationary base as the robot base. The robot does not contain any rigid joints and rigid links. As can be seen in the image, the robot consists of three linear actuators which actuate three tendons. The main structural element of the robot consists of a hollow latex tube which is appended with a number of guide collars, shown in Fig. 2.4b, made using polyurethane sheets. These guide collars are used to guide the three tendons which are made using Kevlar® thread of 1mm diameter. The latex tube and tendons are attached to an end flange, shown in Fig. 2.4a, which is made from polyethylene. This is the only other element which moves along with the robot arm. An inherent safety feature in the design of the system is the near monolithic structure of the arm leading to fewer edges and a lighter design. Notably there are also

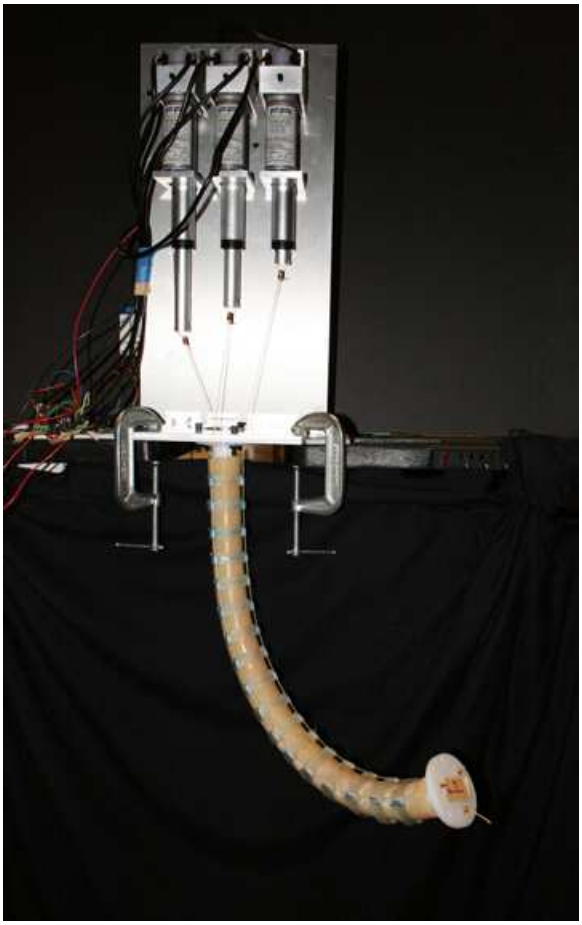

Figure 2.3: A prototype of a 2 active DoF continuum arm

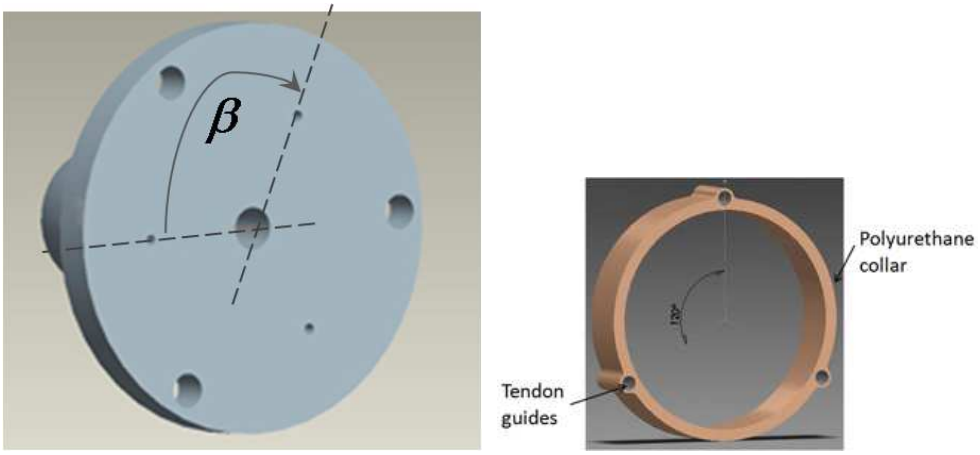

(a) End flange (b) Guide Collar

Figure 2.4: Continuum arm components

no hard metallic surfaces in the robot arm.

2.5.2 Analytical Kinematics

The continuum arm is a remotely actuated continuum type robot. The kinematics of continuum type robots have been previously discussed in [39, 105, 16]. The robot arm is 0.6m long. We have a total of 3 actuators for the system, however, the arm is assumed to be a 2 DoF system. This is because the tube of the arm, which is its *backbone*, is much stiffer in axial compression relative to stiffness in the transverse or bending direction. In other words, the arm can easily bend in any plane but cannot change length easily and therefore the DoF corresponding to this motion is ignored. The purpose of the third actuator is only to increase the workspace of the system. At any given time, only two sets of actuators are controlled independently.

The following assumptions are used to write out the forward kinematics equation:

(a) The arm always bends in a plane,

(b) The arm bends in circular arcs only, and

(c) The length of the arm remains constant throughout its motion.

Implicit in (a) is the fact that we do not consider the effect of gravity to be large. We define the configuration of the arm by the parameters δ and κ. δ defines the plane in which the arm bends and κ defines the curvature of the arm. The equations relating the configuration parameters to the displacement of the linear actuators q_i are given by [105] as follows:

$$\delta = \text{atan2}(A,B) \tag{2.3}$$

$$\kappa = \frac{\theta_0 - \theta_L}{L} \tag{2.4}$$

$$\text{where,} \quad A = -q_1 \sin\beta, \qquad B = -q_1 \cos\beta + q_2$$

$$\theta_L = \theta_0 + \frac{q_1}{r\cos\delta}$$

β is the angular spacing between the tendon locations on the end flange (shown in Fig. 2.4a), r is the radial distance between the location of the tendons on the end flange and the center of the end flange, L is the length of the robot arm and $\theta_0 = \frac{\pi}{2}$. In the above equations, we have assumed that the first two actuators are independently actuated; the equation can be easily modified to include any pair of actuators as the three actuators are arranged symmetrically about the arm cross-section.

Based on the above equations, the position of the end of the arm can be computed using:

$$\begin{pmatrix} x_e \\ y_e \\ z_e \end{pmatrix} = R^{\delta} \frac{L}{\theta_L - \theta_0} \begin{pmatrix} \sin\theta_L - \sin\theta_0 \\ 0 \\ \cos\theta_0 - \cos\theta_L \end{pmatrix} \tag{2.5}$$

Here, R^{δ} is the rotation matrix corresponding to a rotation about the vertical axis (in our case the Z axis) by the angle δ. Note that the coordinate system for the definitions above is placed at the base of the arm with the Z-axis pointing vertically downwards and the X-axis passing through the location of the first tendon on the base of the arm.

Using the above equations, it is possible to command trajectories for the linear actuators based on desired configuration space trajectories. The workspace of the robot is a surface embedded in $\mathbb{R}^3$. The nature of the workspace in a quadrant is depicted in Fig. 2.5. There are a number of factors causing the physical system to deviate from the analytical kinematics: (a) the arm is assumed to be straight when relaxed, however, this is not always true, (b) the gravitational effect does become large enough for some configurations, and (c) the tendons are not perfectly guided along the geodesics between the two end faces of the tube. In the next subsection, we shall discuss kinematics of the arm based on experimental data to account for the above sources of error.

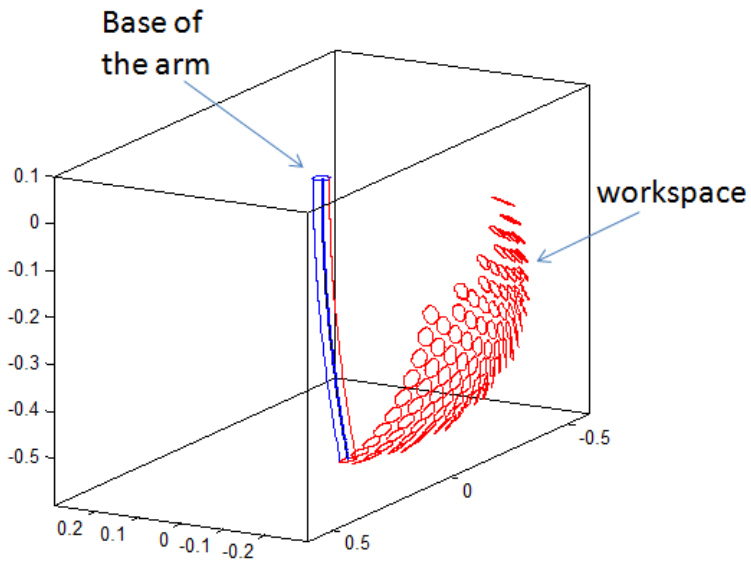

Figure 2.5: Workspace for the continuum arm in a quadrant

2.5.3 Experimental Kinematics

For experimentally finding the position of the end of the arm in response to changes in position of the linear actuator, we used a Vicon® Motion Capture system (MoCap). Markers were placed on the end flange and the position of the center of the end flange was recorded along with the actuator positions. Potentiometers were used to measure the position of the linear actuators. As can be seen in Fig. 2.6, the prediction of the analytical forward kinematics model, although close, is not entirely accurate.

Based on the collected data, it is possible to either improve upon the model or directly use the data for inverse kinematics of the arm using a procedure like locally weighted regression (LWR) [20, 4]. The forward kinematics model is useful to know where the arm is, given the actuator positions, and also for inverse kinematics using inverse Jacobian based methods. We shall explain why it is not very useful in our case to improve on the model and shall illustrate the use of LWR to learn the inverse kinematics for the continuum arm.

For the continuum arm, the forward kinematics model utilizes only three parameters namely

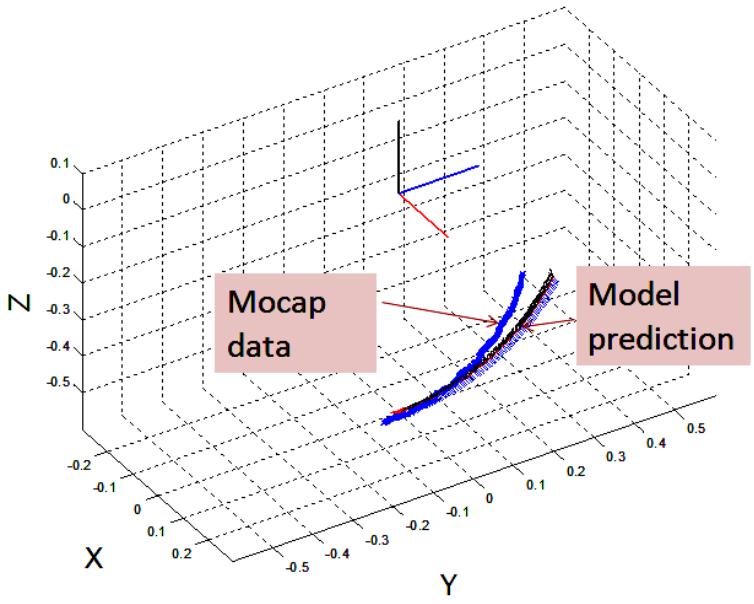

Figure 2.6: Position data for the end of the arm and predicted position using analytical model

the radius of the tube r, the length of the tube L and the angular spacing between the tendons β. Each of these parameters is easy to physically measure and is therefore accurately measured for our system. However, the scale of the errors in the model prediction in Fig. 2.6 is much larger than what might be expected from small errors in the kinematic parameters. We can, therefore, only hope to improve the performance of the model if we increase its complexity. Since the unmodeled effects in the system are very complicated, it is hard to increase the complexity of the model to include these effects. We, therefore, directly use the data to develop the inverse kinematics map.

For our analysis, we use locally linear models in LWR. Given the data $(X_i, Y_i)_{i=1\ldots N}$ (where X_i is a 3-vector giving the position of the end disk with respect to a frame at the base of the robot and Y_i is a 2-vector containing the position of the two active linear actuators) and the query q, locally weighted regression (LWR) using a linear model generates the following output:

$$y = q\beta \tag{2.6}$$

$$\text{where,} \quad \beta = \arg\min_{\beta} \sum_{i=1}^{N} w_i \|Y_i - Y_i^e\|_2 \tag{2.7}$$

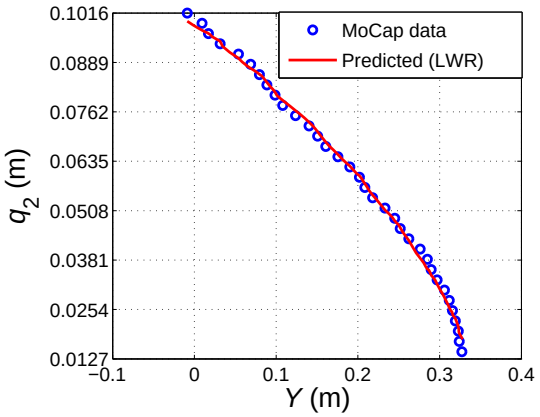

(a) Predicted and actual position values of the second actuator q_2 plotted with Y coordinate of the arm end

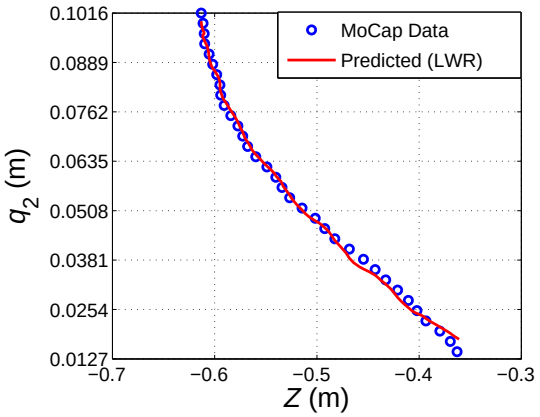

(b) Predicted and actual position values of the second actuator q_2 plotted with Z coordinate of the arm end

Figure 2.7: Inverse kinematics map for the continuum arm using LWR

Here Y_i^e is the predicted output for the given input data X_i:

$$Y_i^e = X_i^T \beta \tag{2.8}$$

$$w_i = e^{-kd_i^2} \tag{2.9}$$

$$d_i = \|X_i - q\|_2 \tag{2.10}$$

k is a parameter used to control the size of the region of relevant data points, d is the distance between the query and data points and can be defined based on a suitable metric (in the equation above, we have used the Euclidean distance). Fig. 2.7 shows the predicted values of the actuator position for various positions of the end coordinates of the arm based on the method described, along with MoCap data.

Based on the above analysis, it is possible to accurately position the end of the arm and move it along desired trajectories in the workspace of the robot. If a desired position lies outside the workspace of the robot, i.e., it does not lie on the surface in $\mathbb{R}^3$ accessible by the robot, then LWR gives the actuator positions q_i corresponding to the orthogonal projection of the point onto the

Figure 2.8: The continuum arm pushing a box resting on a surface

workspace surface.

Fig. 2.8 shows the continuum arm executing an example motion to show its motion in $\mathbb{R}^3$. On careful observation of Fig. 2.8, it can be seen that the arm deflects when it comes in contact with the box. This is a unique characteristic of such an arm, where the motion of the arm can adapt to the environment it functions. Such behavior highlights the fact that it is important to have some means of sensing the contact forces for the continuum arm as these contact forces affect the motion of the arm.

2.5.4 Application to Human Interaction Tasks

To demonstrate the applicability of such a system to tasks involving close interaction with humans, the continuum arm was utilized to feed an individual. It must be noted that, at this stage of development of the robot is not equipped to grasp general objects. For this task, the robot was pre-equipped with a feeding tool (fork) and was controlled to follow a desired motion of the end effector. As can be seen in Fig. 2.9 the robot starts by picking up the food (pick phase), which in the shown example is pudding and then proceeds onto bringing the food close to the subjects mouth. The subject then decides to open his mouth and consume the food. At this stage the subject and robot are physically interacting up until the feeding tool is out of the mouth of the subject (feed phase). The robot is following a desired trajectory using only position control of the linear actuators.

It should be noted that in the above example it is the subject that moves his head to bring the fork inside his mouth. The robot does not actively insert the fork into the mouth. More DoFs are

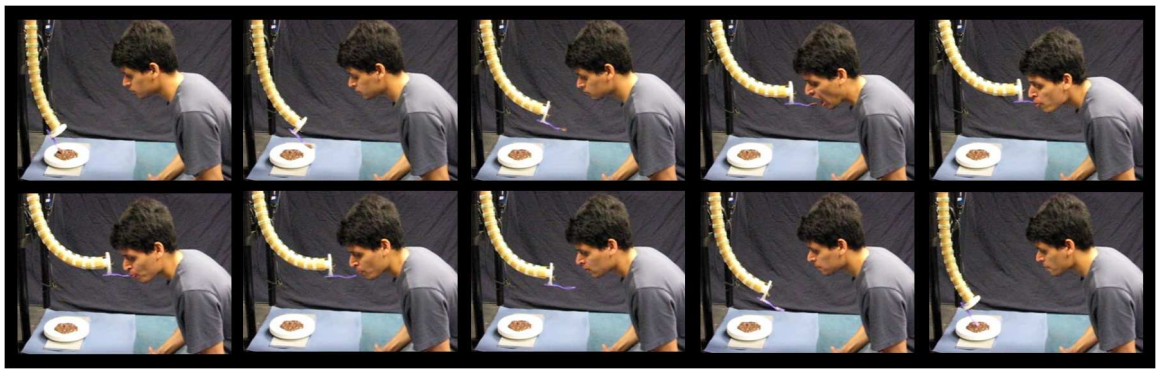

Figure 2.9: The continuum arm feeding a subject

Figure 2.10: Passive compliance allowing subject neck motion

needed to allow the bowl and subject position to be varied arbitrarily in the robots workspace. The passive rather than active approach of food insertion demonstrated here would be suitable only to people with disabilities that do not affect head motion capabilities. For individuals with more severe disabilities that does not allow head motion an active feeding approach must be taken.

The active approach of for food insertion bears resemblance to the peg in hole problem studied extensively in force control literature [91, 70]. In this case the location of the hole in not fixed during the insertion phase. Since the subject is free to move his/her head the interaction during this phase must be compliant. In the continuum arm compliant interaction is achieved by the passive compliance in the system. The passive compliance allows for small neck motion that occur during the feeding phase as shown in Fig. 2.10.

2.5.5 Discussion

The continuum arm moves using only continuous deformation along its structure. This allows using an extremely flexible robot structure for safety while using the same flexibility to move the system. Our approach towards developing the continuum arm has been to use minimal rigid parts in the structure which potentially negate the safety benefits of the system. This has lead to a design consisting of a single rubber tuber with tendon guides. The kinematics for the resulting system are complex enough to warrant to use the of a data driven approach to develop the kinematic map between actuator positions and the end effector pose. One of the key drawbacks of the system is the lack of structural damping leading to uncontrolled undulatory motion in the arm even at low speeds. Further work is necessary to analyze the arm motion in the presence of external forces, as the arm motion is highly dependent on these unlike rigid systems.

2.6 Single Link Inflatable Robot

The next few subsections will provide details regarding some of our initial development work on inflatable link robots. We shall first study the modeling and control of a single inflatable link. This section of work is largely based on [97]. The system shown in Fig. 2.11, although very simple is important in understanding and addressing certain key challenges in developing an actuated inflatable link. The development lead to ideas regarding the type of material to be used and some unique ideas regarding how to couple the links to actuators. We shall describe these developments in subsequent subsections.

Besides the challenge of designing a practical inflatable link robot, we also need to establish the ability to do useful tasks using robots with inflatable links. One such ability is force control. We attempt to develop such capability for a single link inflatable robot. The purpose of doing so will be two fold: a) develop a modeling technique for inflatable link systems b) utilize the model to design controllers for the system. We shall describe both of these aspects along with experimental

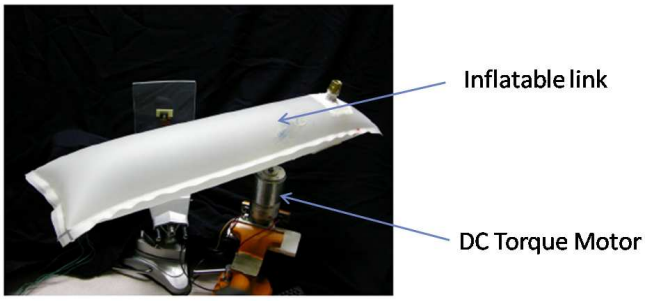

Figure 2.11: The Single Link Inflatable Robot

results in subsequent subsections.

Inflatable structures were used in a robotic manipulator in [94]. To the best of the author's knowledge, the use of inflatable structures for force control is not previously documented. Force control with flexible link manipulators has been studied [12, 13]. We believe that the class of systems being investigated by us would operate under deflections which do not permit the use of a linear deflection model. We therefor use a Pseudo Rigid Body Model (PRBM) [52] to analyze the system under large deflections.

2.6.1 System Description

As depicted in Fig. 2.11, the prototyped system consists of a single inflatable link actuated at the base with a DC torque motor. In the following discussion we shall use the term inflatable link and beam interchangeably as the inflatable link functions structurally as beam. The inflatable link we use in our system have been fabricated in our lab with polyurethane sheets of varying thickness. The sheets are heat sealed to form an air tight chamber. We have also experimented with polyethylene sheets which did not give satisfactory results due to less structural load capacity, weak seals obtained, and formation of plastic regions after inflation. The lesser load capacity and formation of plastic regions can be related to the lower yield stress of polyethylene compared to polyurethane. The lower yield stress causes achievable pressures in the link to be smaller. Formation of plastic regions causes crimping of the link ultimately leading to lower structural capacity.

For a polyurethane inflatable beam of length 50 cm, we were able to successfully carry a force of 8 N at its end. The limitation in load capacity is largely due to certain prototyping issues. With this load capacity, the system can be used for applications such as manipulation of lightweight objects and grooming which have small force requirements and are relevant to assistance in activities of daily living (ADLs). Higher load capacities on the order of a few hundred Newtons can be achieved as is shown in [122, 64].

Inflatable beams are different from traditional beams as the material used to make them can only hold tensile stress. An inflatable tube can be modeled in a number of ways as suggested in [52, 113, 122]. The simplest approach is to consider the effect of pressure in the tube as a pre-stress in the tube. Then the Euler-Bernoulli beam theory for large deflections can be applied to obtain deflections and stresses in the beam. The beam fails when the stress at any point on the surface of the beam is less than zero. In the following subsections, we discuss a system model and system behavior.

2.6.2 Large Deflection Beam Analysis

In the following discussion, we review some theory about large deflections of solid beams to understand the deflection characteristics of an inflatable beam. We assume the beam is inextensible and consider only geometric nonlinearity. For the sake of simplicity, we study a cantilever beam with a moment load (M_0) at its end for large deflections. We know from Euler-Bernoulli beam theory:

$$\frac{d\theta}{ds} = \frac{M_0}{EI} \tag{2.11}$$

$$\frac{d\theta}{ds} = \frac{\frac{d^2y}{dx^2}}{\left(1+\left(\frac{dy}{dx}\right)^2\right)^{\frac{3}{2}}} \tag{2.12}$$

where, E is the Young's Modulus of the beam material, I is the area moment of the cross section of the beam, s is the arc length along the beam, θ is the angle of the tangent to the beam from the horizontal, y is the transverse deflection of the beam which is a function of the position x along axial direction. In linear analysis, we say the slopes in 2.12 are small and neglect its powers and get the standard equation. For the large deflection case, the powers of the slope cannot be neglected. Therefore we start with 2.11 and integrate along the arc length s, for the length L of the beam.

$$\int_0^{\theta_0} d\theta = \int_0^L \frac{M_0}{EI}\, ds$$

$$\Rightarrow \theta_0 = \frac{M_0 L}{EI} \tag{2.13}$$

Hence the angular deflection at the end of the beam, with no small deflection assumptions, is given by 2.13. From 2.13, the relationship between angular deflection and moment at the end of the beam is linear. Such a relation allows for a simple representation of a flexible link with sufficient accuracy using only a few parameters as discussed in the next subsection. Such simplifications are also possible for beams with other loading conditions. For a detailed analysis of beams with end loads and large deflection, see [50].

2.6.3 Pseudo Rigid Body Model

The rigid body model allows the representation of large deflections of flexible systems by rigid bodies and spring elements. For instance, the large deflections of the beam described in the previous subsection can be modeled as shown in Fig. 2.12. The model is defined by the following parameters: r defines the distance of the hinge from the fixed end of the beam, l is the length of the beam, K is the spring constant of the torsional spring at the hinge, θ is the angular deflection of the torsional spring, f is the force at the end of the beam and y is the vertical deflection at the end of the beam.

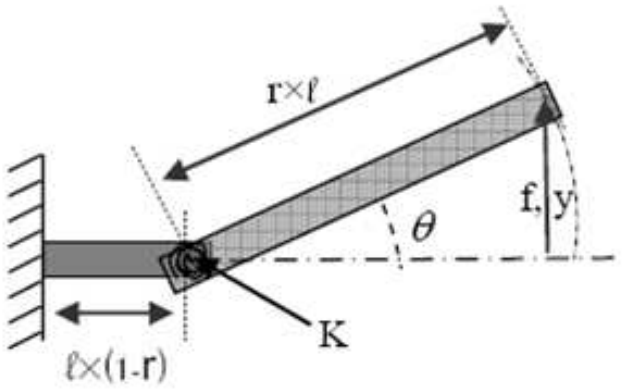

Figure 2.12: Pseudo rigid body model of the link along with associated parameters

The rigid body model consists of two bodies connected by a hinge through a linear torsional spring. Since inflatable links used in serial robots are essentially beams with pre-stress due to internal pressure, we shall model the inflatable link using the rigid body model. Fig. 2.13 shows the components of the system being studied. For the experimental deflection testing discussed in the next section, the coupler B is fixed. The coupler B is attached to the link by the use of polymer adhesives and thermal welding.

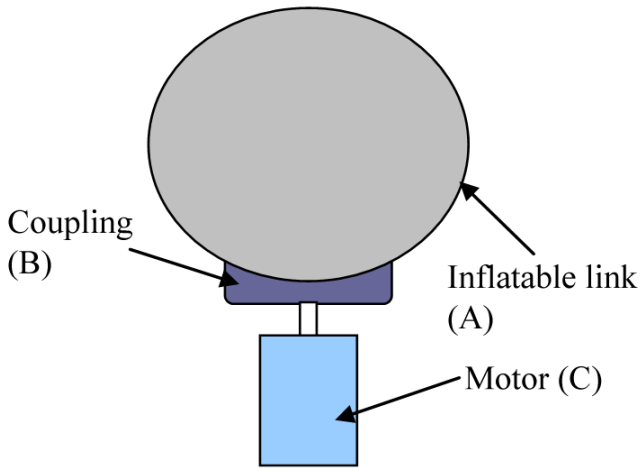

Figure 2.13: Schematic showing the components of the system, looking into the cross section of the link. The coupler is bonded to the link using polymer adhesives and thermal welding.

2.6.4 Experimental Deflection Testing

To fit a rigid body model described in previous subsections to our inflatable beams, we conducted deflection tests. Fig. 2.12 shows the rigid body model that is fit to the system for deflection modeling. The inflatable beam was fixed at one end and weights were hung at the other end of the beam. For the system, we have the following relation between load f and deflection y:

$$
\begin{aligned}
& f_i rl\cos(\theta_i) = K\theta_i + c \\
& \Rightarrow [K,\, C]^T = \left(A^T A\right)^{-1} A^T (Frl) \qquad (2.14)
\end{aligned}
$$

where,

$$
\begin{aligned}
\theta_i &= \sin^{-1}\left(\frac{y_i}{l_i}\right) \\
A_{i,1} &= \theta_i, A_{i,2} = 1 \\
F &= [f_1\cos(\theta_1), f_2\cos(\theta_2), ..., f_n\cos(\theta_n)]^T
\end{aligned}
$$

K is the best linear least squares stiffness for the load deflection data and the offset c is the moment value at zero deflection. The value of r is taken from the literature [50] to be equal to 0.8517. In the experiments, we measure the tip displacements and we need to find the equivalent torsional stiffness K of the beam. Table 1 gives a sample of the load-deflection data. The value of K and c obtained from the data are 3.8576Nm/rad and 0.1205. It is to be noted c is not forced to zero (which would be the case in the absence of unmodeled physical phenomena, errors in the position/force readings, etc.) to get a more accurate approximation of K.

The linear least squares fit of the form given in (2.14) is shown along with experimental data in Fig. 2.14. Although we obtained a linear torsion spring constant K for the deflection model of the inflatable beam, for generality, we shall use a spring with moment-angular deflection relation given by (2.15) in further analysis.

Table 2.1: Load deflection data for inflatable beams

Load (N)	y (mm)
0.6	6
1.1	12
2.6	32
3.7	54
4.3	62
5.0	72
5.6	84

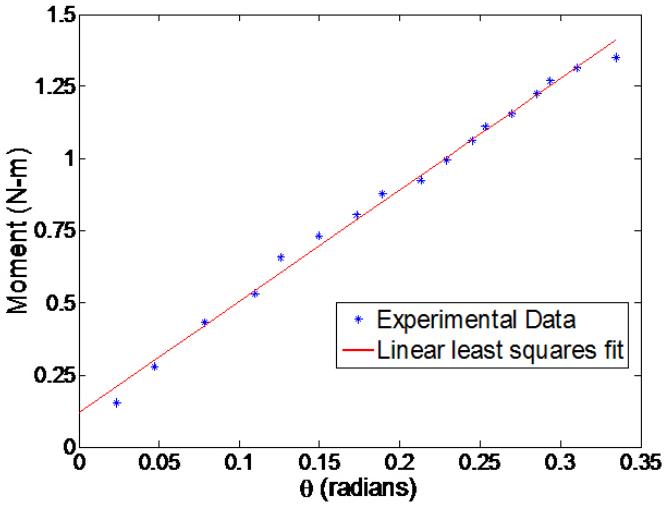

Figure 2.14: Linear spring fit to the load deflection data.

$$\tau = k_1\theta + k_2\theta^3 \tag{2.15}$$

Equation (2.15) is useful if in addition to geometric nonlinearities, other nonlinearities due to material properties, motor-link coupling and other un-modeled effects in the system exist. In fact for all the analysis presented in subsequent sections, (2.15) can be replaced by any higher order function of the angular deflection as well, without affecting the validity of the analysis.

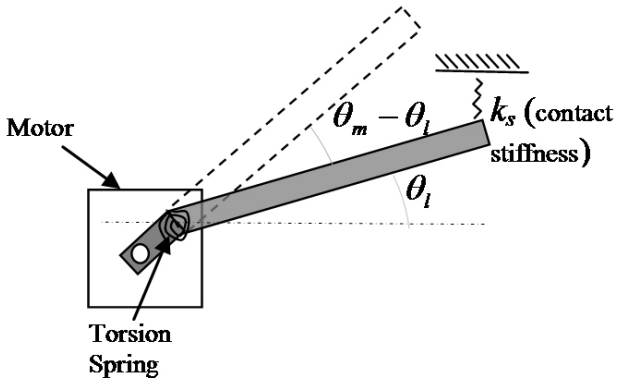

Figure 2.15: Rigid body model of the system.

2.6.5 System Model and Behavior

To develop our control, we propose a rigid body model of the system as shown in Fig. 2.15. Since we have an inflatable link which has high surface compliance, a linear contact spring k_s is a suitable choice. From the model, it can be seen that the system resembles a series elastic actuator (SEA) [89]. The rigid link in our model can be considered massless as we have an inflatable link and its mass can be neglected. The only source of inertia is the motor inertia (J_m).

The equations for the system are given by:

$$J_m\ddot{\theta} + k_1(\theta_m - \theta_l) + k_2(\theta_m - \theta_l)^3 + b\left(\dot{\theta}_m - \dot{\theta}_l\right) = T_m \tag{2.16}$$

In 2.16, T_m is the input torque to the motor, k_1 and k_2 are torsional stiffness coefficients of the spring, b is the viscous damping coefficient, θ_m and θ_l are described in Fig. 2.15. The torque due to contact with the object, T_L is given by (2.17).

$$\begin{aligned} T_L &= \frac{k_s l_c^2 \sin(2\theta_l)}{2} + k_s l_c (l - l_c)\sin(\theta_m)\cos(\theta_l) \\ &\approx \frac{k_s l_c^2 \sin(2\theta_l)}{2} = k_1(\theta_m - \theta_l) + k_2(\theta_m - \theta_l)^3 + b(\dot{\theta}_m - \dot{\theta}_l) \end{aligned} \tag{2.17}$$

assuming $\frac{k_s l_c^2 \sin(2\theta_l)}{2} \gg k_s l_c (l - l_c) \sin(\theta_m) \cos(\theta_l)$.

where $l_c = rl$ and $r \simeq 1$. Note that from (2.17) T_L is a function of θ_l, further we define the stiffness f_N at any deflection as

$$T_N(\theta_m - \theta_l) = k_1(\theta_m - \theta_l) + k_2(\theta_m - \theta_l)^3 \tag{2.18}$$

Using (2.16) and (2.17) we can obtain the state space form of the dynamic equations:

$$\begin{aligned} \dot{x}_1 &= x_2 \\ \dot{x}_2 &= \frac{1}{J_m}\left(T_m - \frac{k_s l_c^2 \sin(2x_3)}{2}\right) \\ \dot{x}_3 &= \frac{1}{b}\left(k_1(x_1 - x_3) + k_2(x_1 - x_3)^3 + bx_2 - \frac{k_s l_c^2 \sin(2x_3)}{2}\right) \end{aligned} \tag{2.19}$$

where $x_1 = \theta_m$, $x_2 = \dot{\theta}_m$ and $x_3 = \theta_l$.

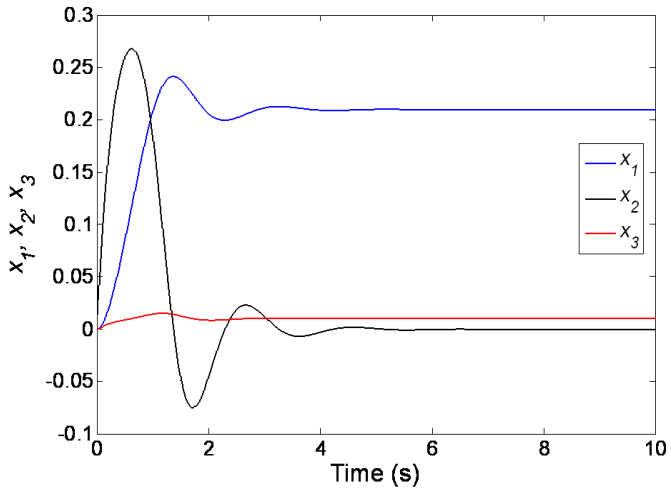

Figure 2.16: Step response of the system.

System Behavior The system described by (2.19) was simulated with an input $u = T_m = 1$. Fig. 2.16 describes the response with time. For the step input $Tm = 1$ applied at $t = 0$, the system

exhibits stable characteristics as can be seen from the response.

Lyapunov Stability Analysis We use the Lyapunov method for studying the stability of the system [109]. For understanding the stability properties of the system, we take the candidate Lyapunov function V as:

$$V = \frac{1}{2}x_2^2 + \int_0^{x_1 - x_2} T_n(\sigma)\, d\sigma + \int_0^{x_3} T_L(\sigma)\, d\sigma \tag{2.20}$$

V is a positive definite function as each of the terms involving the spring stiffness integrates to positive values. Here T_L, f_N were defined in (2.17) and (2.18) respectively.

Differentiating (2.20) we get,

$$\dot{V} = x_2\dot{x}_2 + T_N(x_1 - \dot{x}_3) + T_L(\dot{x}_3)\dot{x}_3 \tag{2.21}$$

Using (2.17) and (2.18) in (2.21

$$\begin{aligned} \dot{V} &= -bx_2^2 + 2bx_2\dot{x}_3 - b\dot{x}_3^2 + x_2u \\ &= -b(x_2 - \dot{x}_3)^2 + x_2u \end{aligned} \tag{2.22}$$

As can be seen from (2.22), for the open loop response i.e. when $u = 0$, $\dot{V} \leq 0$. Therefore as can be seen from Fig. 2.16, the system is stable. Further, asymptotic stability can be proved by invoking LaSalle's theorem. For the closed loop system, the control law u needs to be chosen to ensure stability in the Lyapunov sense.

2.6.6 Force Control

Considering the system behavior, there are a number of options regarding what states we need to measure and the states we want to control. We shall explore two sensing options: a) place an

encoder at the motor which gives the motor angle, b) place a force sensor at the contact tip to measure the contact force. We desire a constant reference force F_d given by:

$$F_d = y_d = k_s l_c \sin(x_{3d}) \tag{2.23}$$
$$\Rightarrow x_{3d} = \sin^{-1}(F_d / k_s l_c)$$

The set point input u_s is,

$$u_s = \frac{k_s l_c \sin(2\theta_{3d})}{2}$$

This shifts the equilibrium to the desired state and all equations are now with respect to this equilibrium.

Motor Encoder Here we measure the motor shaft angle x_1 and velocity x_2. It should be noted we can use the motor encoder to control the contact force for a static object only. For moving objects, we would need another sensor to inform us about the position of the object. The output of the system is given by:

$$\bar{y} = \begin{bmatrix} x_1 & x_2 \end{bmatrix}^T$$

We choose the proportional derivative (PD) control law:

$$u = k_p(-x_1) + k_v(-x_2) \tag{2.24}$$

We modify the Lyapunov function V to V' such that

$$V' = \frac{1}{2}x_2^2 + \int_0^{x_1 - x_2} T_n(\sigma)\, d\sigma + \int_0^{x_3} T_L(\sigma)\, d\sigma + \frac{1}{2}k_p x_1^2 \tag{2.25}$$

Again differentiating (2.25) with time:

$$\begin{aligned}\dot{V}' &= -bx_2^2 + 2bx_2\dot{x}_3 - b\dot{x}_3^2 + k_p x_1 x_2 \\ &= -b(x_2 - \dot{x}_3)^2 - k_v x_2^2 \end{aligned} \tag{2.26}$$

Clearly, $\dot{V}' \leq 0$. Hence the system is stable in the sense of Lyapunov. Fig. 2.17 and Fig. 2.18 show the simulation of the above system.

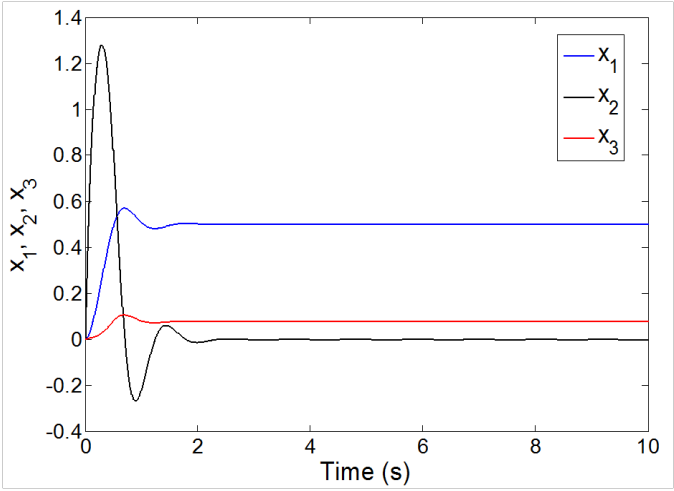

Figure 2.17: Model states in simulation with PD control on motor angle.

Contact Force Sensor Here we place a force sensor at the contact point and measure the contact force. We assume that the contact force lies in the plane of the actuation torque from the motor.

The output is given by:

$$y = k_s l_c \sin(x_3)$$

The proposed control law u is:

$$u = k_p(-y) \tag{2.27}$$

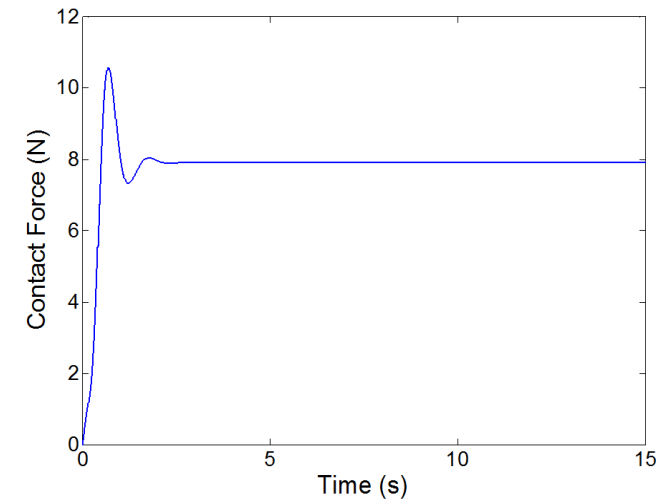

Figure 2.18: Contact force in simulation with PD control on motor angle.

Using (2.27) in (2.22):

$$\begin{aligned}\dot{V} &= -b(x_2 - \dot{x}_3)^2 + x_2 kp(-y) \\ &= -b(x_2 - \dot{x}_3)^2 + x_2 k_p k_s l_c \sin(x_3)\end{aligned} \tag{2.28}$$

From (2.28), the stability of the system is unclear. It can be observed that if $x_3 \ll x_2$, then $\dot{V} \leq 0$. However if k_p is increased to a sufficiently large value, $\dot{V}$ may not remain negative semi-definite and the system may become unstable. Fig. 2.19 shows the advantage of using force feedback in terms of convergence to the desired force level.

2.6.7 Experimental Results

Experiments using the system shown in Fig. 2.11 were performed. The system comprises of an inflatable link actuated at the base using a DC torque motor, a 500 CPR Motor Encoder and a Honeywell Force Sensor (Honeywell FSG15N1A). It should be noted that the range of forces applied to the link was limited in the experiments due to actuation limitations. We operated only under small deflections of the beam. Control sampling frequency was 100 Hz. Fig. 2.20 and Fig.

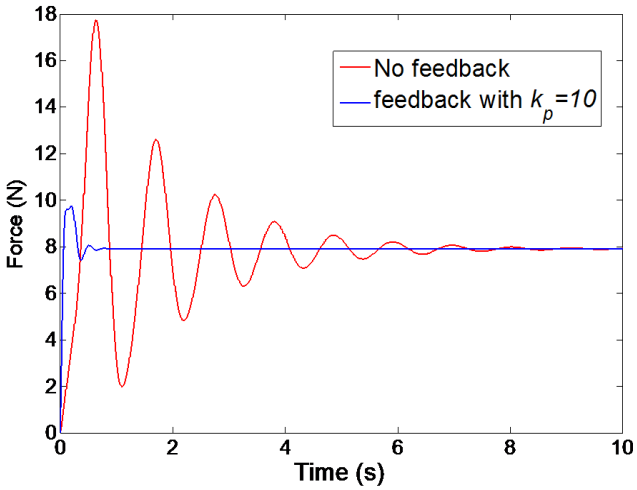

Figure 2.19: Contact force in simulation with and without feedback.

2.21 show the contact force evolution for different desired force values using PID control on motor position and force sensor feedback respectively.

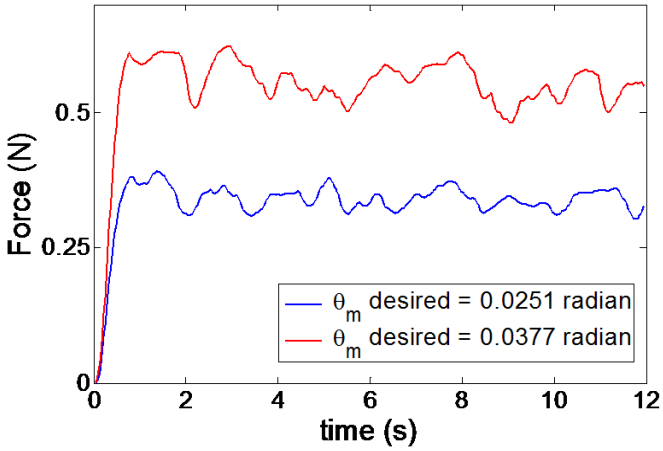

Figure 2.20: Force at the contact point due to position control on motor.

2.6.8 Discussion

The use of a single contact force sensor allows the contact force to be controlled at the assumed contact point only. Using printed strain gages on the polymer used to fabricate the inflatable link allows the possibility of aggregate force sensing and multi-contact point force sensing. This would

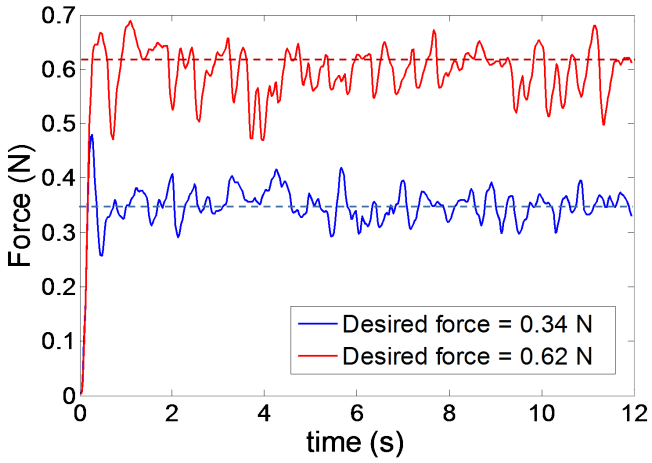

Figure 2.21: Force at the contact point due to force feedback.

enable force control while contacting an external object at any point on the inflatable link it.

For our system, we consider force in a single plane only. The extension of force sensing and control to all 3 dimensions needs to be addressed. The system we described has a single active degree of freedom, therefore we can actively control force in a single direction only. We can increase the degrees of freedom in two ways: a) using multiple inflatable links, b) achieving motion through elastic deflection of the link in 3D. Achieving motion via elastic deflection in a manner similar to continuum type manipulators is not typically well suited to an inflatable structure. The membrane material from which the structure is built is incapable of holding compressive stress, therefore a continuum system is possible only when the material is pre-stressed with high tensile strains similar to a rubber balloon used to make balloon toys.

2.7 Variable Morphology Robots

Robots with soft structures have the potential of varying their morphology, i.e, they can exhibit parametric (size of links, location of joints, etc.) and non-parametric changes (connectivity of links, number of links, etc.) to their geometry. Morphology variation can be used to match the structure of the robot to the task, for e.g, to achieve variable stiffness or impedance in the structure.

Figure 2.22: Variation in location of buckling site along an inflatable link

We have explored this idea of variable morphology by implementing a mechanism that can allow variation in the location of the joint along the structure of the robot. We will briefly describe this mechanism next, which we will refer to as the Variable Buckling Hinge Mechanism.

2.7.1 The Variable Buckling Hinge Mechanism

The variable buckling hinge mechanism utilizes buckling in the structure to create to joints. The location of buckling serves as a joint functionally similar to a revolute joint. By controlling the location of the buckling site it is possible to vary the location of the joint, as depicted in Fig. 2.22. It is possible to do this for both thick walled structures such as that used in the Continuum arm, in Sec 2.5 and thin walled structures such as the inflatable robots described throughout this thesis. The implementation described here utilizes a thick walled latex rubber tube similar to the one utilized for the Continuum arm.

The mechanism consists of a primary tubing that is reinforced along its length by a secondary tubing, as shown in Fig. 2.23a. The reinforcement tubing is split into two segments and the gap between the two segments is maintained by the use of a string or tendon. As the secondary tube is pulled or pushed the location of the gap changes. The gap in the secondary tendon biases the primary tube to buckle at that location as it is weaker due to the lack of reinforcement at the location of the gap. Another tendon that runs along the length of the primary tubing an terminates at its end is used to bend the primary tube. After the application of sufficient force on this tendon the primary tube buckles at the location of the gap of the secondary tubing.

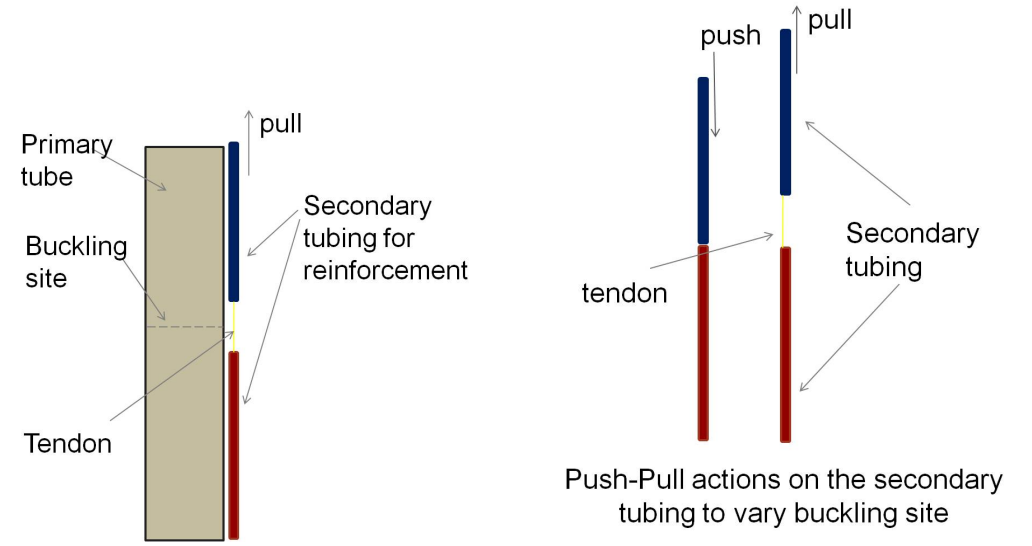

(a) Schematic showing the various components of the buckling hinge mechanism

(b) Push-Pull actions on the secondary tubing to vary buckling site

Figure 2.23: Variable buckling hinge mechanism schematic

Fig. 2.24 shows the physical implementation of the variable buckling hinge mechanism and the variation in the buckling site caused by the variation in the gap location of the secondary tubing.

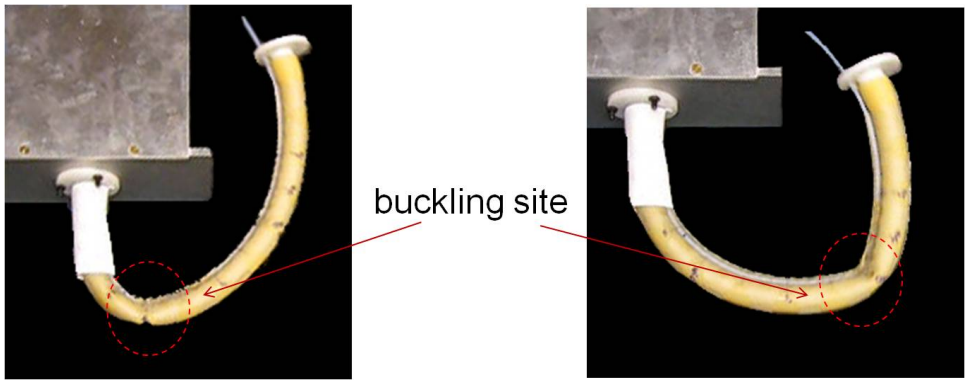

Figure 2.24: Variation of buckling site along the length of the tube in the physical implementation of the variable buckling hinge mechanism

2.8 Summary

In this chapter, we reviewed various injury modes that can occur during physical human robot interaction and safety indices to measure the severity of injury during collisions between a human and a robot. We also reviewed some of the existing techniques used to mitigate the risk of injury such as compliant control, joint compliance and other existing relevant robot designs such as that flexible link robots, soft coverings, continuum robots and inflatable robots. Some of our preliminary work carried out in developing two types of soft robots: continuum robots and inflatable robots was also described.

Chapter 3

Design for Safe Physical Human Interaction

In this chapter we introduce design paradigms for safe robots. We characterize manipulators based on the type of curves that can be used to describe their geometry. Based on this characterization we identify various design paradigms that can be included for any given manipulator. Using computational arguments based on optimal control we attempt to also attempt to answer questions regarding the theoretical performance advantages of rigid and soft robots in the presence of safety constraints.

3.1 Design Paradigms For Safe Robots

To deal with safety under dynamic loading we need to change the characteristics of the system at high force interaction frequencies. As any practical controller has finite bandwidth, the system characteristics at high frequencies are unaffected by the controller and therefore governed only by the open loop characteristics of the system. Fig. 3.1 illustrates this effect of finite control bandwidth. Since the high frequency force interaction depends on the open loop characteristics only, it is necessary that we modify the physical design to achieve desired safety under dynamic loading or impacts. We must then answer the question of what these design modifications can be.

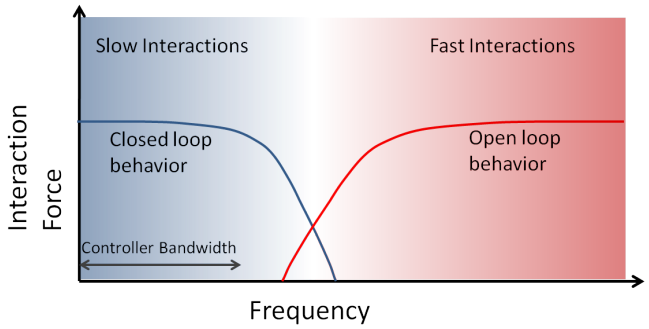

Figure 3.1: Force interaction at various frequency. While introducing compliance in the structure of the robot improves open loop characteristics, it can adversely affect closed loop performance.

It is useful to identify design paradigms for robots that will lead to safer systems with comparable performance characteristics. For safety against injuries due to dynamic loading discussed in Sec. 2.1.2, the following design paradigms can be identified:

- The manipulator should be light
- Contact compliance is beneficial
- Unsprung mass is beneficial
- Distribution of compliance is beneficial

Robots with soft structures naturally allow the above characteristics to be present in the robot and this provides a motivational argument as to why we need to think of developing soft robots when considering application domains involving domestic environments and working in close proximity to humans. In Sec. 3.2 we discuss in some detail the characteristics of a soft robot that are useful in realizing safe robots.

If the robot structure can be described by a curve (Sec. 3.2.1) then soft robots can be realized using either multiple links (Fig. 3.5) or using flexible links (Fig. 3.4b). For more general manipulators whose structure can be defined by surfaces and solids, soft robots may resemble any thing from a blob of dough [76] to compliant mechanisms being utilized in the emerging area of microelectromechanical systems (MEMS) [61].

3.2 Synthesis of Safe Systems

We shall next discuss how we can synthesize robot structures that are better suited to the application domain of pHRI. The synthesis process will allow us to understand why soft robots may work in our favor for our desired applications.

To gain insight into why we need robotic systems that have physical characteristics which are very different from most current robotic systems, a synthesis procedure for the design of a robot which factors in safety requirements is useful. By developing such a synthesis procedure we can hope to answer questions regarding the nature of the 'softness' or compliance in the system. The broader scope of the work here is to answer the question - what is the best robot structure (open loop/closed loop, number of link, link flexibility, etc.) when safety is important? Note that implicit in the above question is the notion that the robot is required to perform some task. Understandably the above question has not been extensively looked at previously due to the prime application domain of robots, which has thus far been in industry, where human robot interaction is not expected. Recent work by Bicchi and Tonietti [8] takes a step towards answering these questions by finding the optimal stiffness in a simple two mass robot model, for rest to rest maneuvers in the presence of safety constraints. We shall attempt to explore this question further.

3.2.1 Characterization of Soft Robots

Since most robots have a serial structure, it is possible to make some simplifying assumptions regarding the design space of robotic manipulators 3.2. The structural space of manipulators can be thought of consisting of one dimensional curve having C^k continuity, where $k \geq 0$. Manipulators consisting of rigid bodies connected via joints can be represented using C^0 curves (we shall refer to these manipulators as C0 manipulators) while continuum type manipulators can be represented using curves of with at least C^1 continuity(we shall refer to these manipulators as C1 manipulators). The continuum arm described in Chapter 2, Sec. 2.5 is an example of a C1 manipulator. Robot

manipulators may also be represented using piecewise differentiable curves. A common example is flexible manipulators. We shall refer to these as C0C1 manipulators. The inflatable manipulators describes in this thesis belong to the C0C1 category of manipulators. Each of these representations allows different design parameters in the synthesis of safe robots. We shall describe these design parameters next.

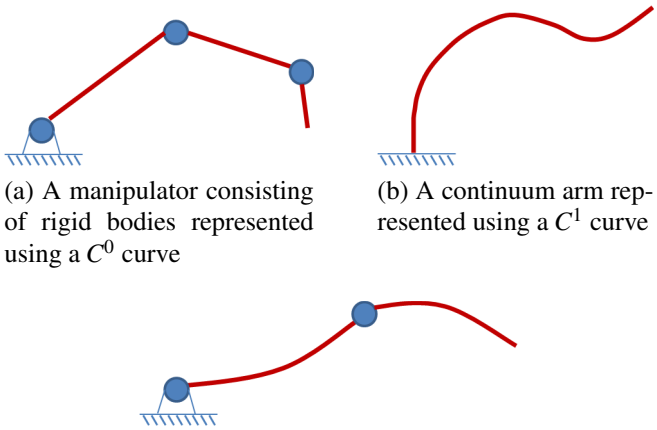

(a) A manipulator consisting of rigid bodies represented using a C^0 curve

(b) A continuum arm represented using a C^1 curve

(c) A piecewise C^1 curve representation of a flexible manipulator

Figure 3.2: Curve representation of manipulators

Inertial Parameters

For a C0 manipulator the inertial parameters are a set of link masses m_j, location of center of mass for each link r_j and inertia tensors I_j. How do these parameters affect the safety? Consider safety under impacts. For a simple robot model shown in Fig. 3.3, as described previously in Sec. 2.2.2, the maximum impact force F_{max} is give by (2.2), restated here for clarity:

$$F_{max} = v_{impact}\sqrt{m_{rob}k_c} \tag{3.1}$$

where, v_{impact} is the impact velocity, m_{rob} is the mass of the robot and k_c is the contact stiffness of the robot. Clearly, if the mass of the robot is reduced the impact force decreases. Lightweight

manipulators are therefore desirable from a safety point of view. Additionally, as long as we are within the class of C0 manipulators, reducing the mass of the system does not adversely affect performance.In fact it can make the system faster. The design paradigm 'lighter is better' is therefore obvious.

Besides choosing the overall mass of the system, as stated previously for a C0 manipulator, the mass m_j, center of mass locations r_j and inertia I_j properties of each link in the system can be chosen. In other words, we can choose how to distribute mass within our system. For a C1 manipulator this choice relates to the mass per unit length $\gamma(s)$, here s is the arc length parameter. Assuming the manipulator is made from a single material, $\gamma(s)$ can be modified via the cross-section of the manipulator. While for a C0 manipulator the mass distribution can changed independent of the compliance in the system, the compliance in the system is related to the mass distribution for a C1 manipulator through the cross section of the manipulator along its length.

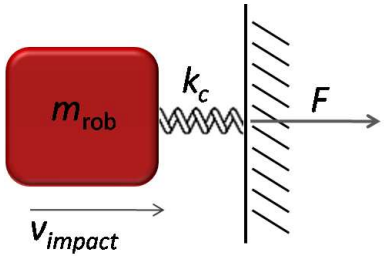

Figure 3.3: A simple one mass model of a robot with contact compliance

Compliance

When the robot manipulator can be represented using a C^0 curve as in Fig. 3.2a, compliance in the structure may be located at the joints. Previously described in Sec. 2.4.2, we shall refer to such compliance as lumped compliance (Fig. 3.4a). When the robot manipulator may be described by a differentiable curve, i.e a C1 manipulator, compliance is distributed (Fig. 3.4b), such systems were discussed briefly in Sec. 2.4.3. Another form of compliance which is independent of the structural representation is the local compliance at the surface of the structure, this is termed as

contact stiffness (Fig. 3.4c).For the simple robot model shown in Fig. 3.3, k_c represents the contact stiffness. From (3.1) the impact force decreases as the contact stiffness decreases. As the robot dynamics are independent of the contact stiffness the performance characteristics are not effected by changes in the contact stiffness. The design paradigm "low contact stiffness is better" is therefore true.

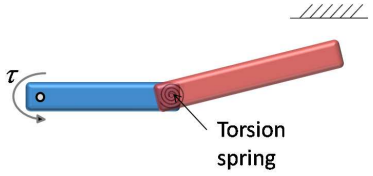

(a) Two link arm with a torsion spring coupling

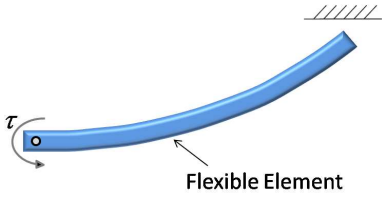

(b) A flexible link

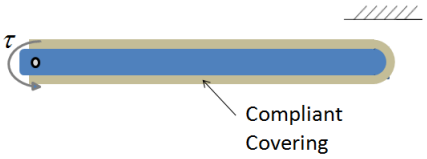

(c) A link with compliant covering

Figure 3.4: Various cases of compliance

For C0 manipulators, the aggregate stiffness in the task space k_{task} and the stiffness at each joint k_i are design parameters. The vector $\vec{k}$, whose elements are k_i, defines the distribution of stiffness within the structure of the robot. Likewise, for C1 manipulators the stiffness in the task space k_{task} is a design parameter. Within the structure, the distributed parameter $k(s)$ defines the stiffness (and compliance) variation along the length s of the manipulator. Note that distribution of compliance is possible in both C0 and C1 manipulators, in C0 manipulators compliance distribution is achieved by the presence of multiple locations of lumped compliance.

By modifying the level of distribution of compliance in a system it is possible to discuss soft robots in a general sense (at least in the serial case) that is beyond simply joint compliance and contact compliance, which have been considered to some extent in the past [98, 137, 77]. Instead we are also interested in looking at systems such as those described in [114, 73, 28, 11] possess-

ing some form of distributed compliance. When compliance distribution is allowed in a system the design space of the manipulator vastly increases. We shall discuss this issue of compliance distribution for synthesis of safe systems in greater detail next.

3.2.2 Compliance Distribution

When compliance is continuously associated with several regions of the structure of the robot, we will refer to such compliance as distributed compliance. Compliance distribution has two important effects:

1. It decreases the unsprung mass during an impact, thus decreasing the maximum impact force.

2. By definition it introduces compliance at multiple location. The unsprung mass during an impact is therefore reduced even as the impact location changes on the structure.

In Fig. 3.5 the unsprung mass is simply the last link that interacts with the external object. We shall see the effect of unsprung mass reduction via compliance distribution on impact contact forces, for a system with rigid bodies using simulations later in this section.

While the above effects are beneficial for safety, The dynamics of the robot are affected by changing the distribution of compliance. It is therefore not clear whether distributed compliance has a degrading or positive effect on performance of the system. We shall attempt to answer this question using optimization.

Given the large number of design parameters available for a system with distributed compliance, we shall focus on the problem of optimizing these parameters from the standpoint of safety and performance. In the case of rigid bodies (Fig. 3.5), the parameters may include the number, mass and length of the intermediate links, the stiffness of the torsion springs connecting the intermediate links, etc. The design parameters for a flexible link may include: the shape of the link, the material's Young's modulus, the cross section, the mass density.

Assuming we can model the system using rigid bodies connected via lumped massless elastic elements in a serial manner, as depicted in Fig. 3.5, the issue of compliance distribution is three-fold. First, we need to decide *how many* sites of compliance may exist in our structure, this is related to the number of bodies in the system. Second, we need to decide *where* we may add the compliance in our structure, this is related to the spatial location of compliance sites. And third, we need to decide *how much* stiffness is to be associated with each site of compliance. The issue of *how much* and *where* involves conventional parametric optimization within a particular dynamic system. The issue of *how many* is more interesting, in that it involves optimization over different dynamic systems of varying structure. The issue of *how many* is most directly related the level of compliance distribution in a system. We shall refer to the problem of *how many* as the number synthesis problem.

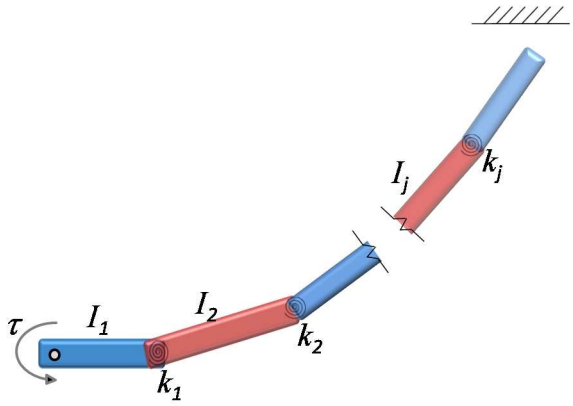

Figure 3.5: Compliance distribution using rigid bodies and lumped elastic elements

It is possible that although these design options may exist, they may not be entirely useful for realizing systems that are safer. It is instructive to see the effect of compliance distribution on safety. Fig. 3.6 shows the decrease in impact force as the number of compliance locations is increased. The number of compliance locations are increased by increasing the number of bodies N. Three cases are shown, when $N = 1$ the manipulator consists of only a single link hinged at the base, when $N = 2$ the link is split into two part of equal length and for $N = 4$ each link is again split into two halves. A larger N represents a greater distribution of compliance. Each

system is impacted with a moving object of identical mass and contact stiffness, moving at the same pre-impact velocity v_{impact}.

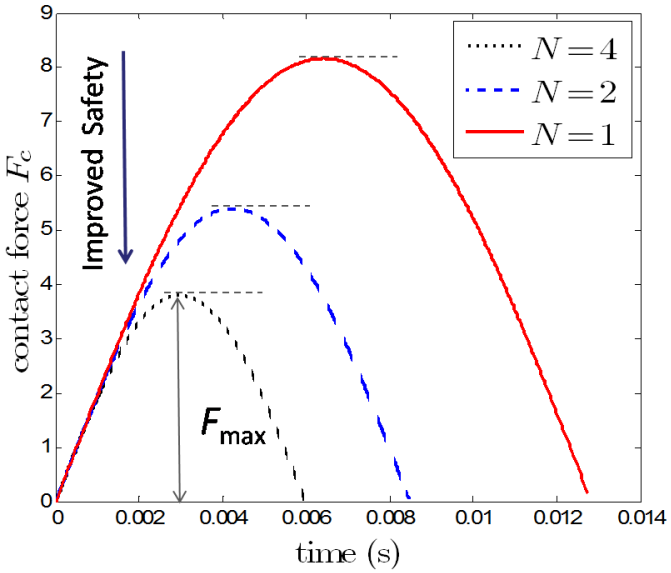

Figure 3.6: Reduction of impact forces by increasing the distribution of compliance

From Fig. 3.6, it is clear that distributing the compliance is beneficial from the point of view of reducing impact forces. This is a result of the reduction of the unsprung mass, mentioned earlier, during the impact. This matches intuition, if one were to walk into a rope at some speed it would hurt less than if one were to walk into a solid link having identical mass/inertial properties to the rope in its relaxed state. The question than is why aren't ropes and similar structures used more often instead of rigid links in manipulators. The reason is, to move a rope constitutes moving an underactuated system and therefore controlling such systems can be difficult. This indicates that there exists a trade-off between good performance and safety when it comes to designing the compliance in a system.

Fig. 3.7 illustrates this safety-performance tradeoff. The system in Fig. 3.7a, which consists of an actuated base connected to a mass via a rigid coupling, may be fast due to the absence of any oscillatory modes. It is also highly unsafe because of the large unsprung mass $m_1 + m_2$ at the contact side. The system in Fig. 3.7b describes the other extreme system where the coupling is

infinitely compliant i.e there is no mechanical connection between the two masses. This system is very safe because the mass at the contact side m_2 (unsprung mass) is small but the system is incapable of moving the mass m_2 and is therefore useless. Various performance criteria must therefore be factored in during the synthesis procedure.

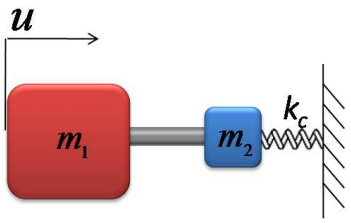

(a) A system capable of moving fast due to a rigid coupling between the actuated mass and the unactuated mass but unsafe due to high mass seen at the contact side of the system

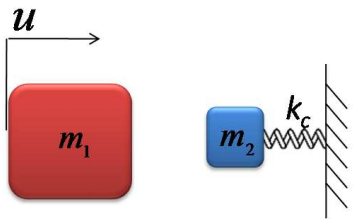

(b) A system potentially very safe due to the low mass at the contact side but incapable of any motion by means of the actuated mass

Figure 3.7: Examples of a system that can demonstrate high performance but are unsafe and another that is very safe but shows poor performance

Performance for a system can be evaluated from two perspectives: open loop and closed loop. The open loop criteria considers performance criteria along trajectories of a system including the maneuver time for a rest to rest motion, the effort needed to move along a desired trajectory and the potential energy of the system along a trajectory. Closed loop performance criteria considers characteristics of the system including the stability of the system under disturbances, disturbance rejection and stability under modeling uncertainties. Although open loop and closed loop characteristics are closely related in a linear system, in general the relation is not straightforward for a nonlinear system.

For this work, we shall utilize the open loop performance criteria of the system and analyze the behavior of the system during gross motions between various regions in its configuration space. We believe both open loop and closed loop criteria must be utilized in a hybrid process to come up with the best characteristics and we hope to achieve such a process in the future.

The next section discusses a formulation for synthesis of safe systems that utilizes system performance metrics. Although we shall utilize the described framework with open loop performance criteria, the framework in itself is not specific to open loop performance criteria and may be directly adapted to utilize closed loop criteria.

3.2.3 Problem Formulation

For the following discussion, we shall concern ourselves with safety of robotic manipulators with respect to uncontrolled impacts only. We are concerned with the problem of designing a robotic manipulator to minimize its potential to cause injury to a human being who may be present in its workspace. There are two approaches that can be used to formulate the design problem. The design variables can be optimized so that: (a) a safety criterion can be extremized while satisfying performance constraints, and (b) a performance criterion can be extremized while satisfying safety constraints. Approach (a) usually lead to extremely safe but slow systems. We shall use approach (b), as it offers the possibility of finding designs which are not only safe but also have good performance.

As we are dealing with non-autonomous dynamic systems, the optimization procedure also involves the bounded control variables $u(t)$. The optimization problem can be written as:

$$\min_{\vec{d}} \min_{u(t)} \; J(\vec{d}) = \int_0^{t_f} L(t, \vec{x}(t), u(t))\, dt \tag{3.2}$$

$$\begin{aligned} \text{s.t.} \; : \quad \vec{x}(0) = \vec{x}_0 \quad &, \quad \vec{x}(t_f) = \vec{x}_f \\ \dot{\vec{x}}(t) \quad &= \quad F(\vec{d}, \vec{x}(t), u(t)) \\ C\left(\vec{d}, \dot{\vec{x}}(t)\right) \quad &\leq \quad 0 \\ |u(t)| \quad &\leq \quad u_{max} \quad \forall t \in [0, t_f] \end{aligned}$$

Here L is the cost function, t_f is the final time, $\vec{x}$ is the state of the system, F defines the dynamics of the system and u_{max} is the maximum actuator force. In (3.2), the optimal control $u(t)$ is found

such that it minimizes the cost functional $J(\vec{d})$ for a particular set of design variables $\vec{d}$; $J(\vec{d})$ is then minimized over the set of design variables $\vec{d}$. The approach described above is similar to [8] where optimal control is used to generate the functional for the optimal design problem, however they use this method to optimize for the mechanism stiffness only. We are concerned with a more general design problem. Based on the above formulation, it is possible to answer important questions regarding the design of a manipulator such as what is the best topology of the actuator link transmission and what is the best stiffness and mass distribution within this topology, etc.

The idea of modifying the actuator-link topology to improve interaction characteristics of the system has been used before. Designs such as the Series Elastic Actuators (SEA) [89] split the actuator and link and couple them with an elastic element. [137] uses series elastic actuators and also modifies the mass distribution within the system to improve performance.

Having presented a general synthesis framework, in the subsequent section, we shall utilize the above framework to gain insight into the nature of compliance distribution needed for safety and performance of linear systems of the type shown in Fig. 3.8. As mentioned previously the number of the bodies in the system affect the distribution of compliance in the system and so we shall focus on the number synthesis problem for this system.

3.2.4 Number Synthesis

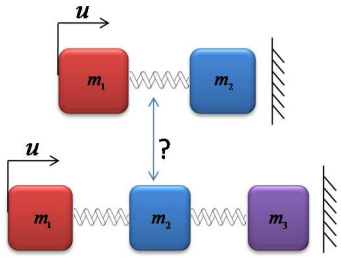

Figure 3.8: The number synthesis problem

A schematic of the number synthesis problem introduced in Sec. 3.2.2 is shown in Fig. 3.8. To simplify our discussion and to neglect geometric effects, we shall only consider linear time-

invariant (LTI) systems of the type shown in Fig 3.8. Such systems are often referred to as *floating oscillators* and they consist of an actuated root with force $u(t)$ acting on it, and a series of n bodies of mass m_i connected with elastic elements of stiffness k_i. The end which is farthest from the actuated root is treated as the contact end of the system.

Our goal is to find the number of masses n, which leads to a system with the best performance while satisfying the safety constraints. We specify performance in terms of time t_f taken by a system to complete a rest-to-rest maneuver. Since our objective is to understand the influence of n in our design, we fix the values of the other design parameters as $k_i = n * k_c$ and $m_i = \frac{M_c}{n}$ to satisfy the constraints in 3.3. We shall formulate the problem as:

$$
\begin{aligned}
&\min_{n} \min_{u(t)} \int_0^{t_f} 1 \, dt \qquad (3.3)\\
&\text{s.t.} : \quad \vec{p}(0) = 0 \ , \quad \dot{\vec{p}}(0) = 0 \\
&\qquad\quad \vec{p}(t_f) = 1 \ , \quad \dot{\vec{p}}(t_f) = 0 \\
&\qquad\quad M\ddot{\vec{p}} = -K\vec{p} + Bu \ , \quad -u_{max} \leq u(t) \leq u_{max} \ , \\
&\qquad\quad m_r \dot{p}_e \ \leq \ P_{max} \ , \\
&\qquad\quad \sum_1^n m_i = M_c \ , \quad \sum_1^n \frac{1}{k_i} \leq \frac{1}{k_c}
\end{aligned}
$$

Here u_{max} is the maximum actuator force/torque that the actuator can exert on the system; the mass matrix M, stiffness matrix K, along with input matrix B define the dynamics of the system. $\vec{p}$ is the vector of position variables for n masses. In (3.3), the safety constraint is implemented by imposing a limit P_{max} on the momentum of the reflected mass m_r moving with the end effector velocity $\dot{p}_e$. As it does not make sense to compare arbitrarily sized systems, we shall only compare similarly sized systems by requiring that the total mass for each design be equal to M_c. The total stiffness of the system is constrained to be greater than a minimum value k_c to meet static load requirements for the design.

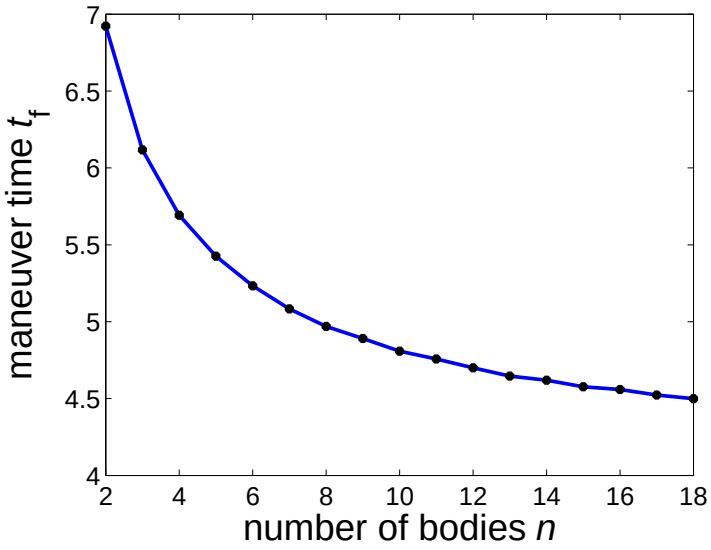

Figure 3.9: Variation of maneuver time t_f with change in number of bodies n

Based on Bicchi and Tonietti [8], the reflected mass m_r at the end effector is given by :

$$m_r = m_n + \sum_{i=1}^{n-1} m_i \prod_{j=1}^{n-i} \left(\frac{k_j}{k_j + \alpha} \right) \tag{3.4}$$

Here α is an interpolating constant; its value is set empirically so that the reduced order dynamics with the reflected mass m_r match the dynamics of the end mass in the full system. In (3.4), if the number of bodies $n = 2$ and $k_1 \to \infty$, then m_r is simply equal to the sum of the two masses i.e. $m_1 + m_2$. This corresponds to the rigid case. Likewise if $k_1 = 0$ (the infinitely compliant case), then m_r is equal to only the mass of the end body i.e. m_2. Therefore, (3.4) interpolates the reflected mass of the system between the rigid and infinitely compliant cases.

Fig. 3.9 shows the variation of the maneuver time t_f with the change in number of bodies n in the system. It is obtained by solving the problem described in (3.3) when the values of m_i and k_i are set be equal $\forall i$. A standard optimal control package (PROPT®[1]) was utilized to obtain the time-optimal control profiles. It can be seen that as the number of bodies increases, the maneuver

[1] http://tomdyn.com/

time decreases. Optimizing over a larger number of variables, including the mass of each body m_i and stiffness k_i, does not alter the nature of this curve. The improved performance with additional bodies in the system also causes the control profile to have more switches as can be seen in Fig. 3.10. This is due to underactuated nature of the system and the presence of higher order modes in the system ([6, 107, 87]). It should be noted that the jagged nature of the control profile in Fig. 3.10a during the middle of its time history is only a result of numerical artifacts during the optimization procedure.

If the frequency of control switches is too high, it may not be possible to implement $u(t)$ on a real system with finite control bandwidth. This is a limiting factor in moving towards higher dimensional systems. If we want to utilize higher order modes, the frequency of the modes up to the highest order mode of interest must be kept sufficiently low. For example in a continuum setting, a very stiff cantilever beam whose second modal frequency is higher than frequency of the control system can only be controlled as a single mode system. To utilize higher order modes, the stiffness of the cantilever needs to be reduced to below the control frequency. Doing this may lead to a faster system in the presence of safety constraints as explained above.

It must be noted that the result obtained is only true in the presence of the safety constraint defined in (3.3). Without the presence of the safety constraint, the inclusion of additional modes in the system leads to delays, thereby increasing the maneuver time. With safety constraints included, each time an additional body is added to the system, the safety constraints become less prohibitive (due to decreased impact forces as demonstrated in the previous subsection). This compensates for the delay introduced by the addition of a body to the system.

It should also be noted that although we have used time-optimal control to guide our design, it is not necessary that time-optimal control be used when the system is actually functioning. We have used time-optimal control only to inform our design procedure.

3.2.5 Flexible Links

The results obtained in the previous subsection were for a linear system. We shall next deal with a system consisting of a flexible link attached to a hub as shown in Fig. 3.11. We shall use this system as a concrete example to demonstrate that a C1 type manipulator which inherently has distributed compliance can have better performance characteristics compared to a rigid manipulator in the presence of safety constraints.

Flexible Link Model

Fig. 3.11 shows the model and its associated parameters and variables. The model assumes planar motion only and consists of a hub on which a flexible link is rigidly attached at its base. The flexible links undergoes linear deformation only which is transverse to the longitudinal direction of the beam. We shall briefly describe the variables in Fig. 3.11 next.

J_h is the hub inertia, τ is the torque applied to the hub, m_L is the mass at the end of the flexible link, m, L, E and I are the mass per unit length, length of the link, Young's modulus and second moment of area of the cross-section of the link respectively. $\{x_0, y_0\}$ is the fixed co-ordinate system, $\{x, y\}$ is the co-ordinate system that is fixed to the hub. $\theta(t)$ is the rotary displacement of the hub, $w(x,t)$ is the transverse deformation of the link at the longitudinal position x along the link at time t.

We shall use the assumed modes method (AMM) detailed in [132, 133, 24] to model the dynamics of the system. The form of the equations is given below:

$$\begin{pmatrix} m_{rr} & m_{rf}^T \\ m_{rf} & m_{ff} \end{pmatrix} \begin{pmatrix} \ddot{\theta} \\ \ddot{\eta} \end{pmatrix} + \begin{pmatrix} C_r \\ C_f \end{pmatrix} + \begin{pmatrix} 0 & 0 \\ 0 & K \end{pmatrix} \begin{pmatrix} \theta \\ \eta \end{pmatrix} + \begin{pmatrix} G_\theta \\ G_\eta \end{pmatrix} = \begin{pmatrix} \tau \\ 0 \end{pmatrix} \tag{3.5}$$

In (3.5), θ corresponds to the rigid displacement of the hub and η is a vector that corresponds to the modal co-ordinates that describe the deformation of the link according to (3.6). The cardinality

of η depends on the number of modes n_m used to describe the dynamics. For our simulations, in most cases two modes were found to be sufficient to describe the dynamics.

$$w(x,t) = \sum_{i=0}^{n_m} \phi_i \eta_i \tag{3.6}$$

For the performance evaluation in the following section the following physical parameters were used: $L = 1, J_h = 0.5, m = 0.54, m_l = 0.0, EI = 18.4/4$, the radius of the hub $R = 0.2$.

3.2.6 Performance comparison in the presence of safety constraints

A time optimal control problem with safety constraints was solved for the above system similar to that described in Sec. 3.2.3 except that the outer design optimization stage is omitted. The same problem was then also solved for a rigid pendulum with the same physical parameters (as applicable) as the flexible link. The safety constraints are enforced in the form of tip velocity constraints for the flexible link and rigid pendulum.

Fig. 3.12 shows the tip velocity magnitude histories for the flexible link and rigid link for a rest to rest maneuver from $\theta = -\frac{\pi}{2}$ to $\theta = -\frac{\pi}{2}$. The maximum actuator torque was set to $u_{max} = 5.0$ in each case. Based on simulations identical to ones used to generate Fig. 3.6 in Sec. 3.2.2, it was assumed a 50% reduction in impact forces is achieved for identical tip velocities of the flexible link as compared to the rigid link. In terms of the safety constraints, this translated to the tip velocity constraint for flexible link to be twice as high than that for the rigid link.

The above example illustrates the fact that including flexible links (a form of distributed compliance), albeit with the correct physical properties, can result in system that has better performance characteristics as compared to a system with rigid links when safety is an unavoidable factor during the system's operation.

It must be noted that the physical parameters of the flexible link in the example were well chosen so that a performance advantage was observed, a poor choice could very well have lead

to a performance disadvantage. The correct physical parameters can of course be arrived at by an optimization procedure such as that described in Sec. 3.2.3 and we hope to do such a problem in the future. In the above example we are answering the question of existence of such a set of physical parameters.

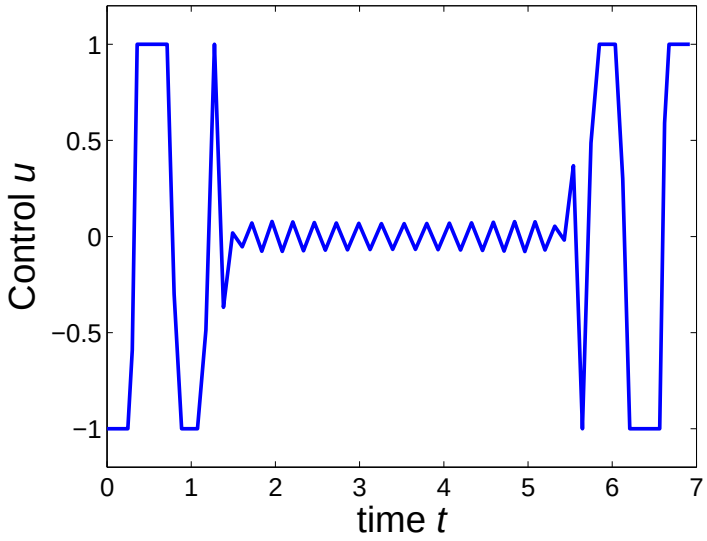

(a) Control u for a 2-body system

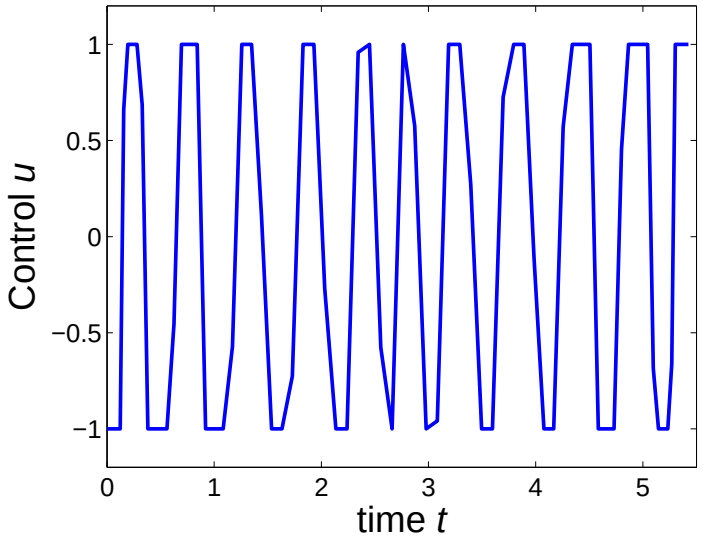

(b) Control u for a 5-body system

Figure 3.10: Characteristics of control u for a system with different number of masses n

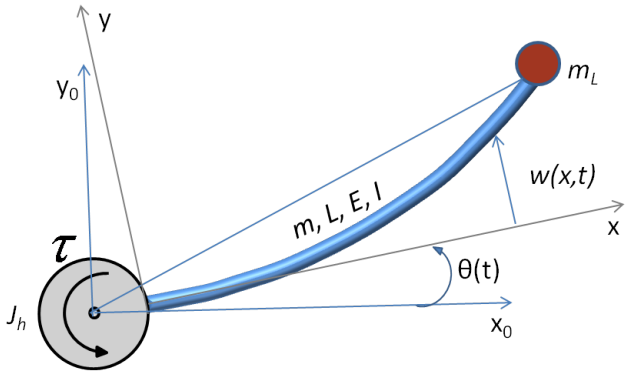

Figure 3.11: Flexible link Model

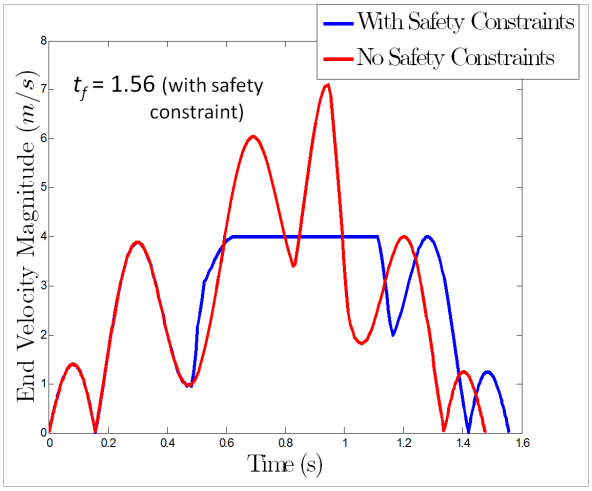

(a) Tip velocity magnitude for the flexible link with and without the safety constraint

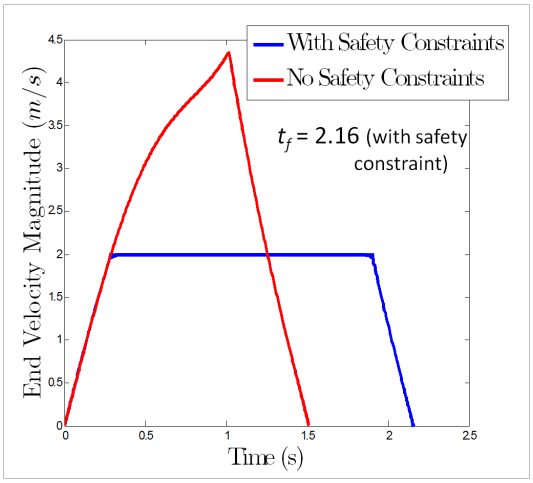

(b) Tip velocity magnitude for the rigid link with and without the safety constraint

Figure 3.12: Tip velocity magnitude time histories for the flexible link and rigid link for a rest to rest maneuver. The maneuver completion time t_f is lesser for the flexible link than the rigid link

3.3 Summary

In this chapter, various design paradigms that are useful for improving safety of robotic system are discussed. Specifically, the role of inertial and stiffness parameters is discussed. A differentiating feature of soft robots from rigid robots with soft coverings is the presence of distributed compliance along the structure of the system. Results from a control-design optimization technique developed indicate that compliance distribution which is a useful property for safety and can also lead to systems with good performance characteristics. The performance criteria considered in this chapter are open-loop, however closed-loop criteria may also be used as in Sec. A.1.

Chapter 4

Hardware

In this chapter, we will provide a brief overview of the inflatable prototypes developed and utilized for this thesis. Three inflatable manipulator prototypes, shown in Fig. 4.1, will be discussed: (1) the CMU inflatable arm, (2) the PneuArm, (3) the AIRarm [1]. We will discuss the CMU inflatable arm in greater detail and will defer some details of the other prototypes to later chapters.

4.1 The CMU Inflatable Arm

The inflatable manipulator (Fig. 4.2) is built using membrane material (polyurethane film: Catalogue #3460, McMaster-Carr) which is maintained under tension by the use of pressurized air. This leads to an extremely lightweight structure which has a weight of the order of a few grams ($\approx$ 5 gm). Besides being extremely lightweight, it allows for a low contact stiffness providing a soft contact interface throughout the structure. In addition, the inflatable structure allows for structural compliance in the form of link flexibility due to the relatively low Young's modulus of polyurethane ($\approx$ 0.025 GPa) used in its construction when compared to traditional materials such as aluminum ($\approx$ 69 GPa) and steel ($\approx$ 200 GPa). The above features are all highly desirable in a

[1] The AIRarm hardware was developed at iRobot as part of a collaborative project with CMU

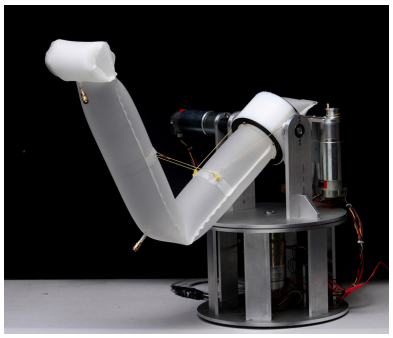

(a) The CMU Inflatable Arm using electromechanical actuation coupled with tendons

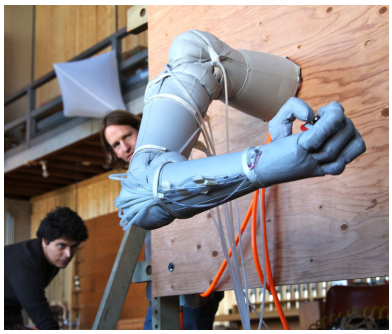

(b) Fabric-based inflatable arm with integrated compressive pneumatic actuators (work at Otherlab)

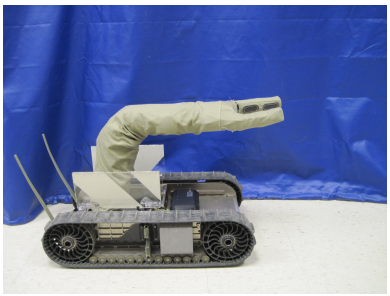

(c) The iRobot AIRarm uses a fabric structure and electromechanical actuation

Figure 4.1: Inflatable arm prototypes developed as part of this thesis with different actuation methods

manipulator to be inherently safe for operation in human environments.

The following subsections describe the design and construction of the inflatable manipulator. We will also discuss arm kinematics, joint stiffness characteristics and joint angle estimation for the manipulator.

4.1.1 The Arm

The arm (schematic shown in Fig. 4.3a) consists of pneumatically sealed inflatable beams which function like traditional links. These links (sections A and C) are connected to each other in a serial manner via an inflatable joint. Many possible implementations of an inflatable joint are possible and have been implemented. In Fig. 4.3b, a flexure type joint is implemented using

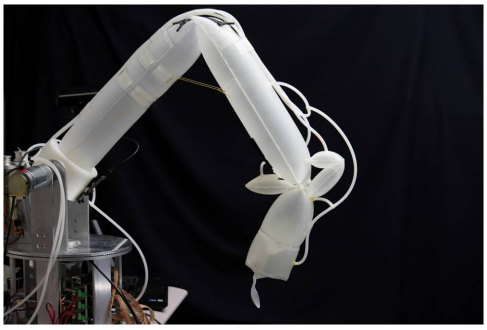

(a) Version of the inflatable arm with 4 degrees of a freedom including a wrist

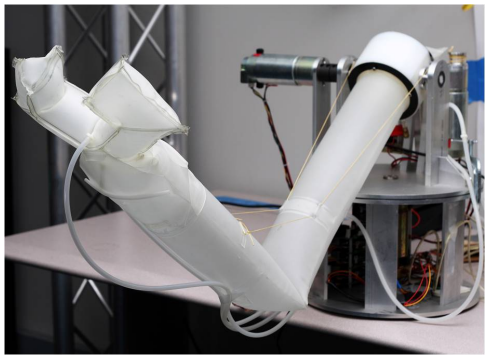

(b) Version of the inflatable arm with the inflatable hand at its end

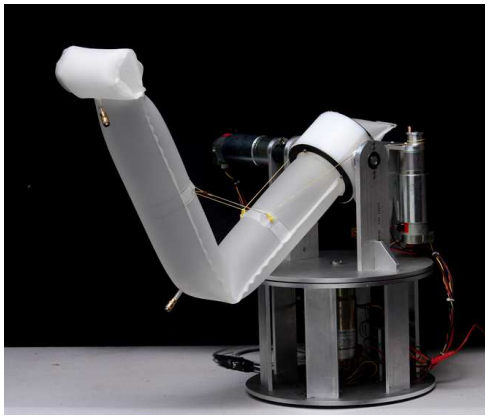

(c) Version of the inflatable arm with the inflatable torus at the end

Figure 4.2: Various versions of the CMU inflatable arm

a pneumatically sealed section (section B). Section B has a reduced cross-section at a particular location. This makes its behavior similar to that of a flexure joint often utilized in compliant mechanisms [51] in that it behaves like a revolute joint with a torsional spring.

In addition to the links and the joint, different versions of the arm (see Fig. 4.2) are equipped with various type of ends to grasp tools and provide additional degrees of freedom. In Fig. 4.2c, the arm has an inflatable gripper which we call the Inflatable Torus, that serves as an end effector that hold various tools. The inflatable torus is passively attached to the arm via a seam joint. In Fig. 4.2b, the arm has a grasping device called the inflatable hand that can be used to grasp and release objects. The hand is passively attached to the arm using a seam joint and restraints to minimize motion relative to the link its attached to. In Fig 4.2a the arm has a wrist at the end which can be used as an interface to various tools and grasping devices. The wrist is attached to the arm via a seam joint and is actuated using pneumatic actuators. Each of the end effectors will be described in detail in Sec. 4.1.3.

As each section is pneumatically sealed due to its construction, the pressures in each of the links and the joints (flexure type) can be changed independently. For the flexural type joint independent pressurization is necessary to prevent premature failure of the arm caused by loss of tensile stress in the membrane near the joint. This mode of failure is described in Sec. 4.1.7. Independent pressurization of the joint prevents premature failure resulting in increased payload capacity.

To fabricate the arm we utilize thermal welding that can generate flat straight seams. With this simple process the above arm construction is made possible by the use of a layered fabrication process which involves sealing selective layers as depicted in Fig. 4.4. The physical arm with the multiple pneumatically sealed sections is shown in Fig. 4.3b. The simplicity of the process offers potential for large scale production of such arm structures at very low cost and high speed. In addition to the links (section A and C) and the joints (section B), additional features may be thermally welded on any of the layers for actuation, sensing, wiring, etc.

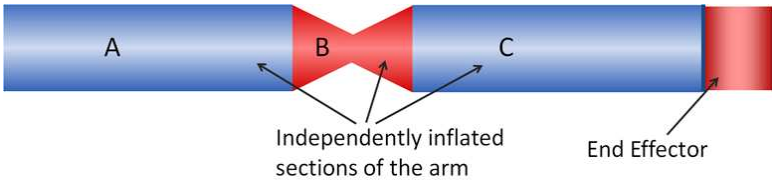

(a) Arm structure schematic (top view)

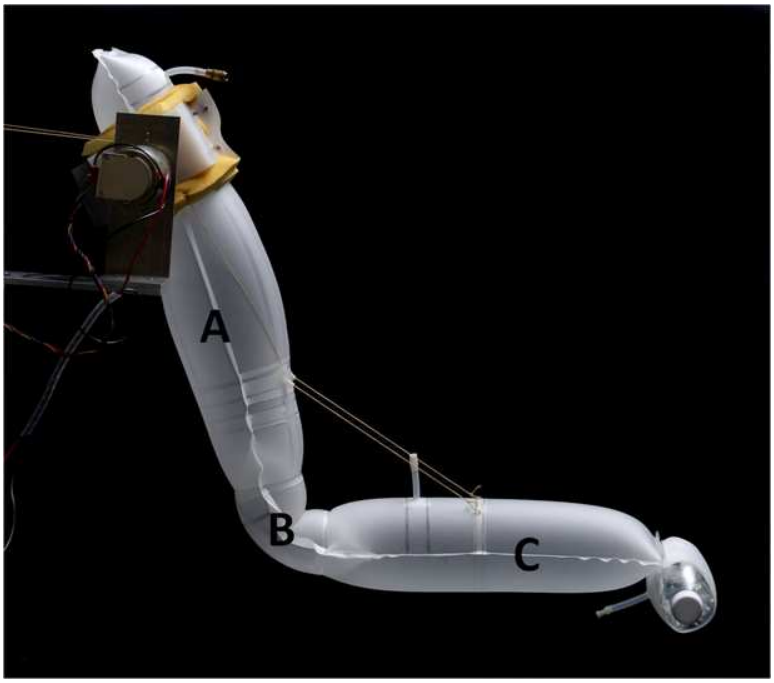

(b) Physical arm (side view)

Figure 4.3: Schematic of the arm structure and the physical arm with independently inflated links (A and C) and the joint (B).

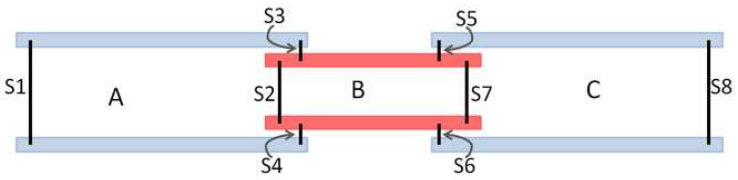

(a) Cross-section in the side view plane revealing layered design to achieve independently inflated sections. Black lines labeled S1-S8 represent seams joining the two layers which are intersected by the lines.

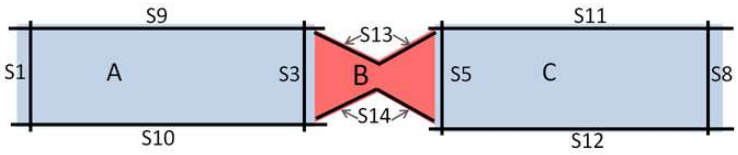

(b) Top view revealing additional seams S9-S14 and shape of the flat structure.

Figure 4.4: Schematic showing layered design of inflatable arm to achieve independently inflated sections in the arm structure using flat straight seams.

4.1.2 Actuation

In its current form (Fig. 4.2a, the inflatable manipulator has four active degrees of freedom. The first link (section A in Fig. 4.3a) is actuated in the plane by directly coupling it to a DC servo motor. The second link (section C in Fig. 4.3a) is actuated using tendons which are driven by DC servo motors as shown in the schematic in Fig. 4.5. The arm can also move out of the plane using the degree of freedom at the base that is actuated by another DC motor. In addition to these three degrees of freedom the arm has an in plane degree of motion at the wrist that is pneumatically actuated. We have also explored other actuation schemes using McKibben pneumatics where the tendons are connected to the McKibben actuators rather than motors (see Fig. 4.6).

The actuation of the second link can be described as an open-ended tendon drive as the tendon terminates at link 2. As the joint between link 1 and link 2 (section B in Fig. 4.3a) has finite stiffness, the tendon works against this stiffness at the joint and allows the joint to be position controlled to any desired angle ($\theta_2 > 0$). The tendon passes through the axis of rotation of joint 1 to avoid kinematic coupling between the two joint angles. As the tendon drives the joint in

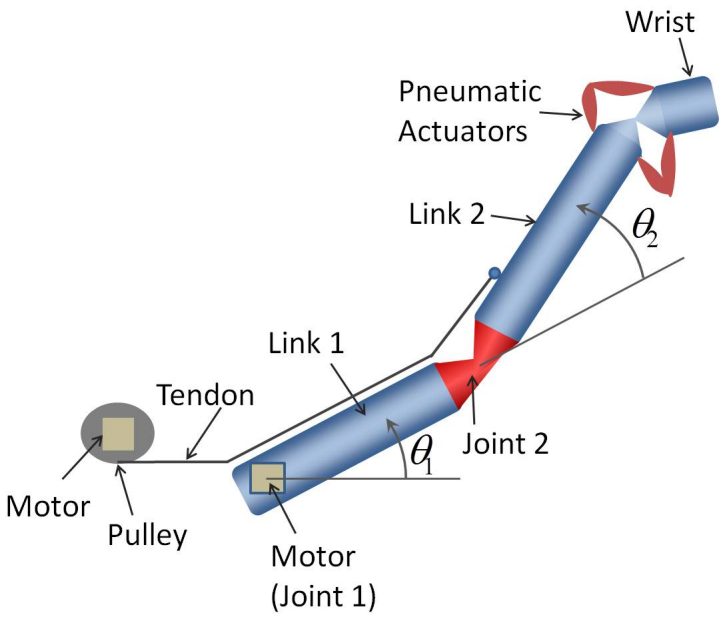

Figure 4.5: Manipulator schematic showing in plane actuation setup for the arm

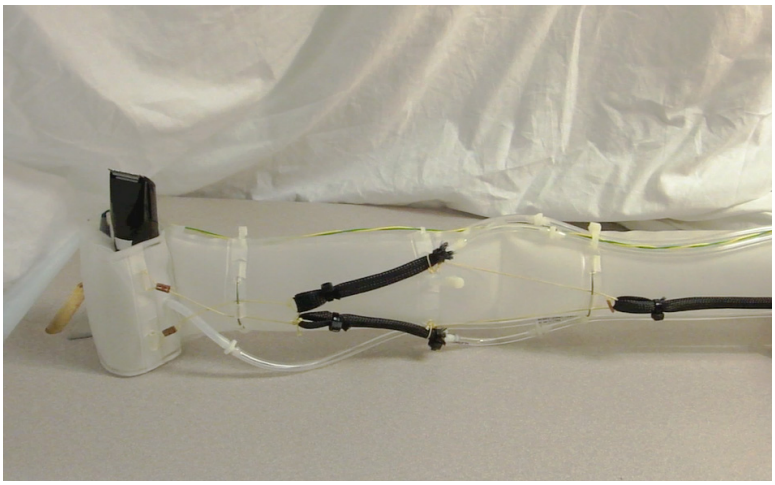

Figure 4.6: Prototype inflatable arm using tensile Mckibben actuators instead of motors

the counter-clockwise direction only, the joint behavior is asymmetric along different directions of rotation. In the physical system, there are in fact two tendons symmetrically spaced from the centerline of the arm in the top view (visible in Fig. 4.3b and Fig. 4.16a). This is done to stabilize the joint against out of plane rotations.

Motors driving joint 1 and the tendons of joint 2 are geared brushed DC motors. The motors are currently capable of only being position controlled using position and velocity feedback from rotary encoders and do not currently have a torque control feedback loop. In the future we plan to introduce torque sensors at the joint and tendon load sensors to have torque control capability at the joint level. The DC geared motors with a reduction ratio of 19.7 are capable of a peak torque of 20 N-m. However the payload capacity of the manipulator is not limited by this peak torque but rather by the structural strength of the system.

Wrist Actuation

The degree of freedom at the wrist is pneumatically actuated using two inflatable variable stiffness actuators (IVSA), shown in Fig. The IVSA is an extremely simple actuator and consists of a single straight inflatable volume. The length of the actuator is such that it remains bent or buckled (in its inflated state) when it is attached across the link and the wrist. Similar to the inflatable flexure joint, the stiffness across the buckled section of the actuator changes as it is pressurized. A similar working principle for an actuator is reported in [69].

Two IVSAs are placed on either side of the wrist and work as an agonistic-antagonistic actuator pair. As the pressure on either of the actuators is varied the torque applied by the actuator varies and results in variation of the equilibrium configuration for the wrist. Therefore, it is possible to control the angle of the wrist by variation of the pressure in the actuators. Alternatively, the actuators can also be used as binary actuators where each of the actuators is completely inflated or deflated to move the wrist to the extremities of its range of motion.

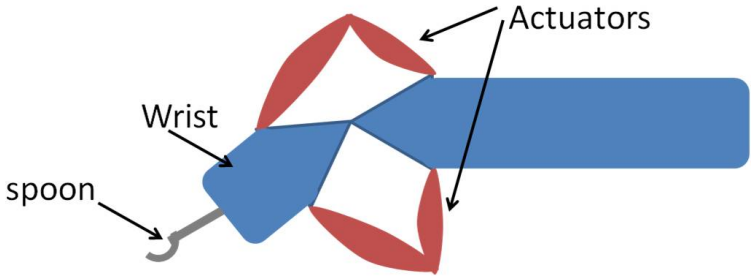

(a) Schematic showing wrist and inflatable variable stiffness actuator (IVSA) arrangement

(b) Physical realization of the wrist and the variable stiffness actuator (IVSA)

Figure 4.7:

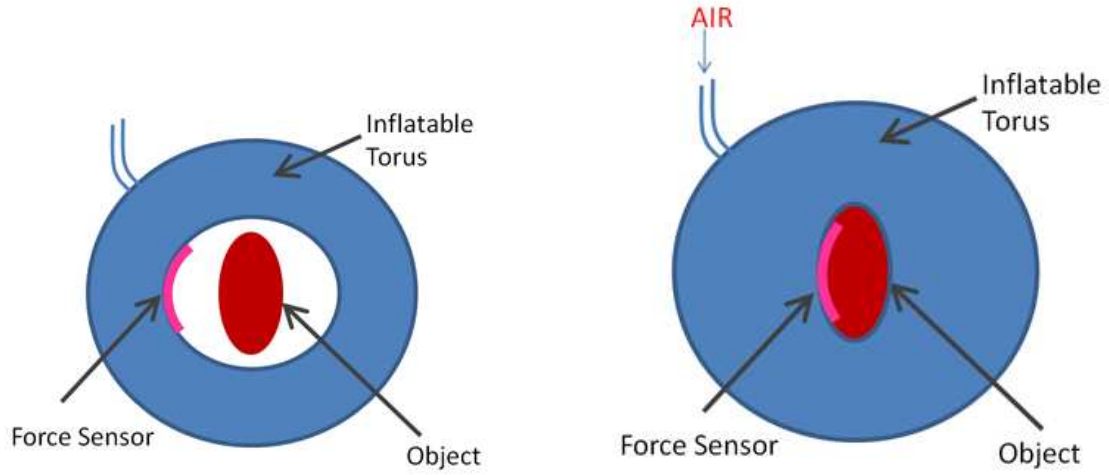

(a) The Inflatable Torus in its deflated state with object to be grasped.

(b) The Inflatable Torus inflated with air to grasp object.

Figure 4.8: Schematic showing the Inflatable Torus in its deflated and inflated state. The torus utilizes a force sensor embedded in its surface to sense contact forces between the external object and the gripper.

4.1.3 The End Effector

For the inflatable manipulator to manipulate real world objects, it needs to be equipped with an end effector that can grasp objects. A rigid end effector would add additional weight and decrease payload capabilities for the manipulator besides reducing some of the safety advantages gained from using an inflatable structure. An end effector that is inflatable gripper does not suffer from these disadvantages and is also easy to integrate with the inflatable structure of the arm during fabrication. A number of inflatable end effectors have been developed for the inflatable arm, we will describe three of them next: (1) the Inflatable Torus (2) the Inflatable Hand, and (3) the Inflatable Wrist.

The Inflatable Torus

The Inflatable Torus, seen in Fig. 4.2c, is an end effector that allows the arm to be equipped with various tools like a spoon, trimmer, etc. As shown in Fig. 4.8, it grasps objects by trapping the

object between its inflated surfaces. The inner surface of the gripper exerts a contact force as a result of expansion due to inflation. This contact force is measured using a force sensor (A401 FlexiForce). In our experiments it was sufficient to inflate the gripper to a single pressure determined empirically (5 psi) without explicit contact force control. The contact force measurement is useful to detect anomalies in the gripping process and for limiting contact forces for delicate objects. Besides contact force, the grasp is also stabilized due to the internal surface of the torus conforming to the shape of the object.

As mentioned before the Inflatable Torus is easy to integrate with the rest of the inflatable arm structure. It is made from the same material (polyurethane film) as the rest of the inflatable structure and can therefore be fabricated as part of the inflatable arm fabrication process. The gripper also demonstrates the capability of handling a large variation of object size and geometry as depicted in Fig. 4.9. Objects as small as pen and as large as a bottle of water can be gripped with the same gripper.

The Inflatable Wrist

The inflatable wrist is similar in form to the inflatable torus with some added functionality. As can be seen in Fig. 4.10 , it is essentially an inflatable torus held within a primary volume. In function, it is therefore like an inflatable link with a *female* interface at one end to grasp tools. The wrist is connected to the preceding link by a seam joint.

The primary volume and the torus interface form separate inflatable volumes using construction depicted in Fig. 4.10. During operation the primary volume is kept inflated while the torus interface is inflated if the tool is to be held or deflated if the tool needs to be removed. Unlike the Inflatable Torus, tools can be held with their axis in the plane of the arm.

The torus interface can be also be used to couple the wrist with other inflatable modules that are constructed with a male interface. This can allow the arm to interchangeably equipped with different grasping devices such as the Inflatable Hand (which we will describe next) or other end

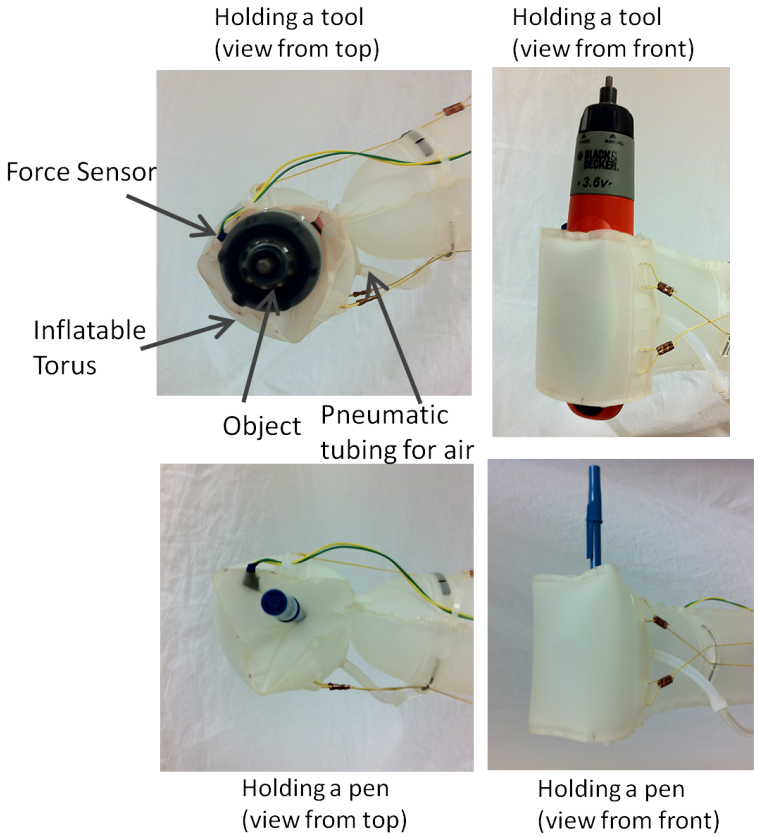

Figure 4.9: The physical construction of the Inflatable Torus. Two example objects are shown being held by the gripper, a power screwdriver (top image, max. dia: 50 mm) and a pen (bottom image, max. dia: 5 mm)

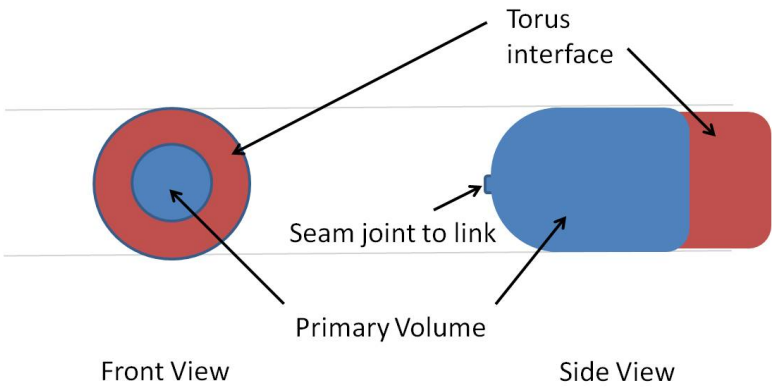

Figure 4.10: Physical schematic of wrist construction showing the torus interface and the primary volume that it is held within.

effectors without having to reconstruct the entire inflatable structure of the arm.

The Inflatable Hand

The Inflatable Torus can be used to hold tools which are inserted into it however it is not ideally suited to picking up grasping objects which are not already within the torus due to the lack of well defined open grasp. The inflatable hand seen in Fig. 4.11, is functionally more similar to a traditional robotic hand with a well defined open grasp.

(a) The inflatable hand in its open state when volume with shape S_1 is inflated

(b) The inflatable hand in its closed state when volume with shape S_2 is inflated

Figure 4.11: The Inflatable Hand

The hand utilizes the concept of shape actuation, detailed in Sec. 7.2. A closed volume with a

shape S_1 that corresponds to the shape of the open state of the hand is combined along a common geometric feature with a second closed volume with shape S_2 that corresponds to the closed state of the hand. The hand takes the shape of whichever volume is inflated. The model for predicting the shape of the structure when both volumes are partially inflated, is not straightforward to compute due to the presence of wrinkling on the two volumes. Fig. 4.12 provides an example of two shapes that can be combined along the common geometric feature which in this case is the black edge of equal length in both the shapes. The shapes can be extruded out of the plane to have non-zero volume for inflation. It should be noted that the volumes do not need be simple extrusions, and can have other complex forms like those described in Sec. 7.2.

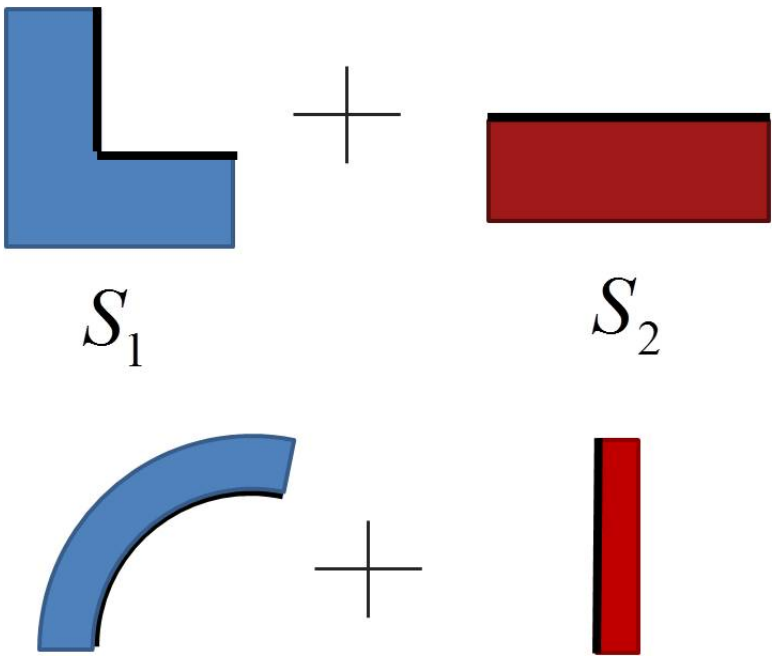

Figure 4.12: Example shapes that can be combined along the common geometric feature which is the black edge of equal length in shape S_1 and S_2. The closed volumes will be extrusions of these shapes.

4.1.4 Kinematics

The inflatable manipulator is identical in structure to a conventional RRR manipulator (arm with 3 revolute joints) with two planar degrees of freedom in the plane and one out of plane DoF at the base. The exception is that the actuator for joint 2 is not collocated at the joint and is instead actuated using tendons. Considering only rigid body motions, the kinematic relationships are identical to an RRR manipulator structure with some additional kinematic relationships to represent the mapping between the actuator configuration and configuration of joint 2. Presence of link flexibility and joint compliance leads to additional deviation from the rigid kinematic model which we address in Sec. 8.2.1.

We shall describe the arm configuration Q in terms of the generalized coordinates arising from the two joint angles θ_1, θ_2 shown in Fig. 4.5 and an additional joint angle for the base, θ_b. We must remind ourselves that in the physical system there is no joint angle θ_2, it is simply our approximate representation of the behavior of joint 2 of the arm. The forward map $K : \mathsf{Q} \to \mathbb{R}^2$ gives the position of the end of the arm corresponding to a configuration $q \in \mathsf{Q}$ of the arm. K is well known for the rigid manipulator and for the sake of brevity we shall not repeat it here (see [22]). In addition to the map K, due to the use of tendon actuation for joint 2 there is an additional map relating the motor shaft angular position θ_{m2} to the joint angle θ_2. We shall refer to this map as the transmission map T. This map assumes the tendons are taut and inextensible.

To develop the transmission map T, we shall approximate section B (joint 2) of the arm using the rigid body kinematic model shown in Fig. 4.13. The tendon length l is mapped to the joint variable θ_2 by $h(.)$:

$$\theta_2 = h(l) = \alpha - \arccos\left(\frac{a^2 + b^2 - l^2}{2ab}\right) \tag{4.1}$$

where α, a and b are defined in Fig. 4.13. The tendon length l is related to the motor shaft angle θ_{2m} by the following relation:

$$l = s(\theta_{2m}) = l_0 - r\theta_{2m} \tag{4.2}$$

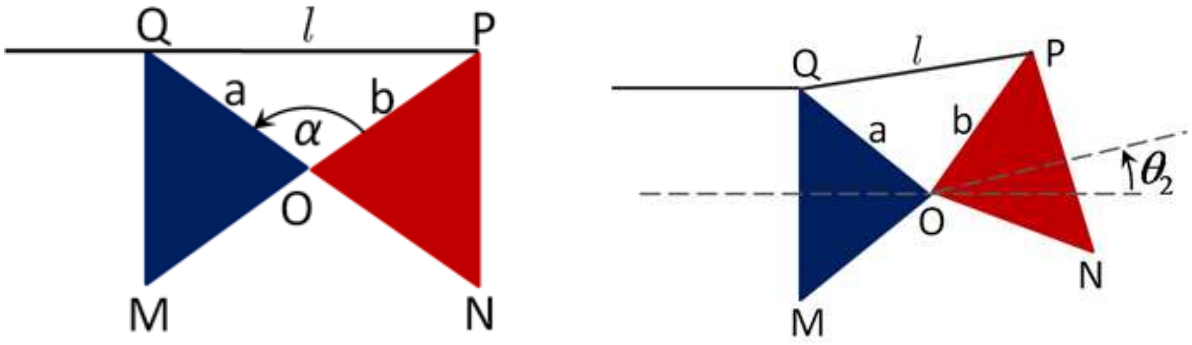

(a) Kinematic model with the joint relaxed i.e $\theta_2 = 0$.

(b) Kinematic model with $\theta_2 \neq 0$.

Figure 4.13: Rigid body kinematic model of joint 2 using two rigid bodies O-Q-M and O-N-P connected at O via a revolute joint. Vertex Q represents the last point on link 1 through which the tendon is constrained to pass through while vertex P represents the tendon attachment location on link 2. α is the angle between O-Q and O-P when $\theta_2 = 0$. a and b are the lengths of O-Q and O-P respectively, l is the length of the tendon between vertex Q and P.

where r is the radius of the pulley driving the tendon and l_0 is the length of the tendon when $\theta_2 = 0$. Composing the two functions in (4.1) and (4.2) provides the desired map $T : \theta_{2m} \mapsto h \circ s\,(\theta_{2m}) = \theta_2$. The inverse map can be similarly computed easily.

The position of the end of the arm (q_e) can then be computed for any given (θ_1, θ_{2m}) by using the maps T and K:

$$q_e = K\,(\theta_1, \theta_2) = K\,(\theta_1, T\,(\theta_{2m})) \tag{4.3}$$

(θ_1, θ_{2m}) correspond to the positions of motor 1 and motor 2 respectively, which are directly sensed using encoders. The inverse relation of (4.3) can also be similarly derived using K^{-1} and T^{-1}.

4.1.5 Joint Stiffness

The joint stiffness for the inflatable joint (joint 2) in the plane of rotation is dependent on the direction of rotation since the joint is actuated by tendons in one direction only. Although we do not at present utilize antagonist tendons, it is easy to implement these on our system. The torsional stiffness in the counter-clockwise direction (k_J^+) is equal to the torsional stiffness of the unac-

tuated inflatable joint (as tendons cannot carry compressive loads) which has been characterized experimentally as shown in Fig. 4.14.

The stiffness of the joint in the clockwise direction (k_J^-) is affected by the stiffness of the tendon in tension k_t, if elastic tendons are considered. For very stiff tendons, such as those made using Kevlar which are used in our prototype, the joint stiffness k_J^- depends primarily on the tendon stiffness. The relationship between tendon stiffness and joint torsional stiffness can be derived analytically using the transmission kinematics described in Sec. 4.1.4. The equations are presented below:

$$M(\theta_2^e) = k_t \left(l(\theta_2 - \theta_2^e) - l(\theta_2)\right) r(\theta_2 - \theta_2^e) \tag{4.4}$$

$$k_J^- = \left.\frac{dM}{d\theta_2^e}\right|_{\theta_2} = k_t \left(\frac{\partial l(\theta_2 - \theta_2^e)}{\partial \theta_2^e} r(\theta_2 - \theta_2^e) + \left(l(\theta_2 - \theta_2^e) - l(\theta_2)\right) \frac{\partial r(\theta_2 - \theta_2^e)}{\partial \theta_2^e} \right) \tag{4.5}$$

Eqn. (4.4) relates the moment M to the angular deflection θ_2^e at joint 2, the nominal unloaded joint angle is θ_2. $l(.)$ is the extension function that relates the joint angle to the length of the tendon, $r(.)$ relates the joint angle to the moment arm for the tendon driven joint 2. (4.5) provides the stiffness of the joint k_J^- for clockwise deflections as a function of the nominal joint angle θ_2 and angular deflection θ_2^e. The tendon stiffness k_t for the Kevlar thread used is ≈ 630 N/mm based on a tensile modulus of 80 GPa, wire dia of 0.96 mm and nominal length 0.4 m.

4.1.6 Design Procedure for Inflatable Links

The primary motivation for using inflatable structures as robotic manipulators is to improve safety. Simultaneously the manipulator must also be capable of performing tasks which will involve carrying a certain payload. In this section, we present a procedure for specifying desired payloads and tip stiffness for inflatable links. The payload capacity and tip stiffness of each link in the

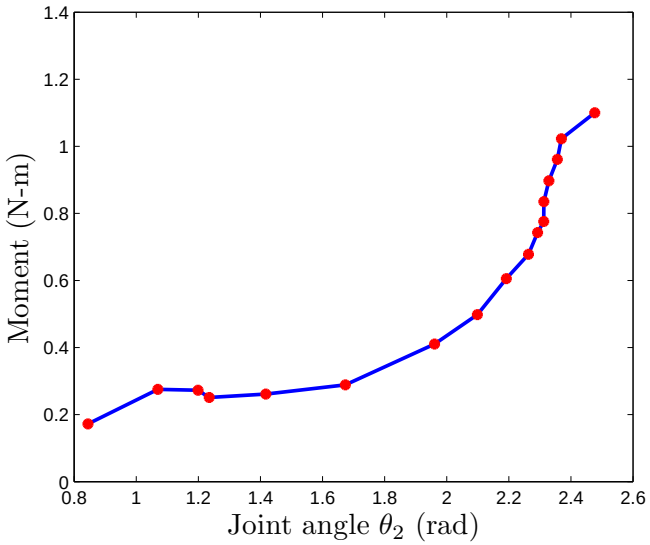

(a) Torsional stiffness of inflatable joint at 2 psi.

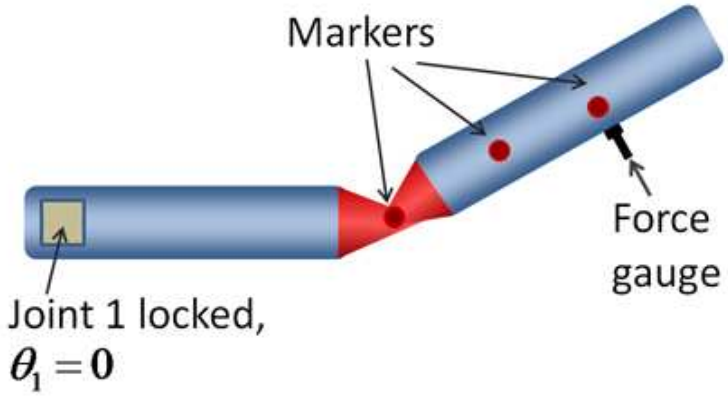

(b) Schematic of experimental setup to measure joint stiffness. The forces were measured using a force gauge at different configurations of joint 2. The configuration of joint 2 was computed using visually tracked markers.

Figure 4.14: Experimental measurement of torsional stiffness of inflatable joint.

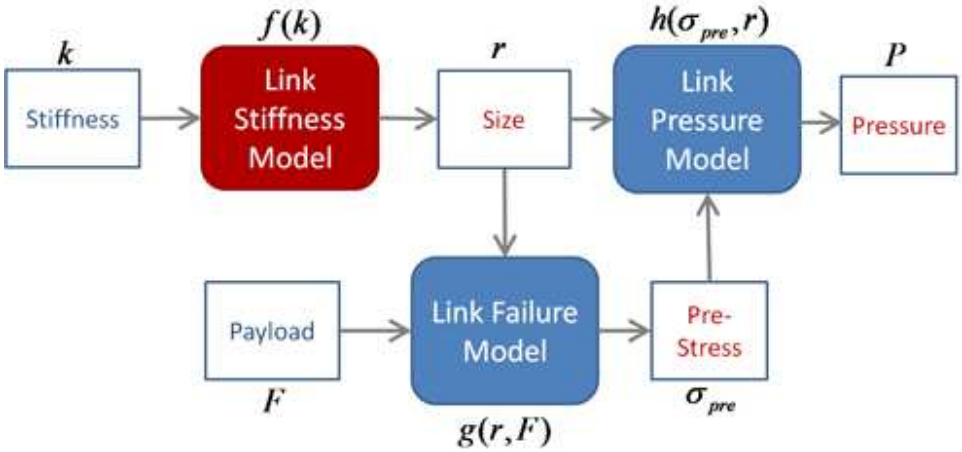

Figure 4.15: Schematic of the procedure for designing an inflatable link. The desired tip stiffness k is used in a link stiffness model $f(k)$ to arrive at the radius of the cross-section r. The desired payload along with r is used in a link failure model $g(r,F)$ to arrive at a desired membrane pre-stress σ_{pre} for the inflatable arm. r and σ_{pre} are then used to compute the desired internal pressure P using the link pressure model $h(\sigma_{pre},r)$.

manipulator affects the overall payload and safety characteristics of the manipulator.

Inflatable links can be operated at a range of internal pressures. This allows for independent specification of payload capacity and tip stiffness for an inflatable link. These specifications can be utilized to arrive at the appropriate cross-section (size) and internal pressure at which the inflatable link must be operated. Fig. 4.15 details the procedure of arriving at the size and pressure parameters for an individual link. It is assumed that the inflatable link has a circular cross-section. The cross-section can be therefore represented by a single parameter r, the radius of the cross-section.

Example Inflatable Link Design

We shall use an example design problem for the inflatable link to explain the procedure illustrated in Fig. 4.15. The specifications for the design problem are the following: Payload (F): 10 N, Stiffness of the link (k): 50 N/m. Following the procedure in Fig. 4.15 we can arrive at the desired

radius of the cross-section r and the internal pressure P using the following sets of equations:

$$r = \sqrt[3]{\frac{kl^3}{3\pi Et}} \text{ (Link Stiffness model)} \tag{4.6}$$
$$= 0.0411\,\text{m}$$
$$\sigma_{pre} = \sigma_{bend} = \frac{Fl}{\pi r^2 t} \text{ (Link Failure model)} \tag{4.7}$$
$$= 2.4683 \times 10^6\ \text{Pa}$$
$$P = \frac{2\sigma_{pre} t}{r} \text{ (Link Pressure model)} \tag{4.8}$$
$$= 4.5720 \times 10^4\ \text{Pa}$$

In the above computations, the following values of the various parameters are used: $E = 0.025\,\text{GPa}$ (Elastic modulus of polyurethane at 10% strain), $t = 0.381\,\text{mm}$ (thickness of polyurethane film), $l = 0.5\,\text{m}$ (length of link).

The link stiffness model (4.6) and link failure model (4.7) are based on the Euler-Bernoulli beam theory applied to cantilever beams with a thin circular cross-section. The link failure model computes the maximum bending stress (σ_{bend}) in the link. As the inflatable link is made using membrane material, the tensile stress in the membrane material (σ_{pre}) due to the internal pressure (P) must balance the maximum bending stress. This is necessary to prevent buckling due to development of compressive stress in the membrane. The link pressure model (4.8), based on a thin cylinder assumption, is used to compute the necessary internal pressure (P) needed to develop a tensile stress (σ_{pre}) in the membrane.

It should be noted that the above procedure is valid only for membrane strains (ε_{pre}) up to around 25%. This is because at higher strains the relationship between membrane stress and internal pressure becomes more complicated than the simple model presented in (4.8). In fact for a highly flexible material like rubber, the internal pressure that can be achieved inside a closed structure like a sphere or cylinder has a maximum value P_{max} which is dependent on the nonlinear

characteristics of the material [80]. For the inflatable links fabricated in our lab we observe a similar phenomenon. A maximum pressure of approximately 10 psi (68.947 kPa) could be achieved in a link with geometrical parameters identical to that in the example presented above. The link continues to inflate and expand volumetrically after achieving the maximum pressure P_{max}, but without any observable increase in internal pressure before material yielding occurs.

In the above inflatable link design example, the membrane strain ε_{pre} resulting from the desired membrane stress σ_{pre} is close to 10%. If the design specifications result in strains greater than the limiting strain, the design specifications may be modified to decrease σ_{pre} and therefore the strain ε_{pre}. For instance, it is possible to increase the stiffness specification and lower σ_{pre}. Another option is to increase the membrane thickness t.

4.1.7 Payload Capacity and Safety

Payload Capacity

The current prototype utilizes links with geometrical parameters similar to those described in the example inflatable link design. The link lengths are slightly smaller and equal to 0.4 m for both the links. Links 1 and 2 are inflated to 5 psi (34.473 kPa) while the joint is inflated to 7 psi (48.263 kPa). Our prototype inflatable manipulator has been tested with payloads of up to 350 gm ($(\theta_1, \theta_2) = (0, \frac{\pi}{3})$). The accompanying video shows the manipulator lift a small bottle of water weighing roughly 350 gm.

The inflatable joint needs to be inflated to a slightly higher pressure than the links to prevent premature failure due to unintended buckling at the joint. In normal operation, the joint structure is buckled on the upper side to allow joint motion (for $\theta_2 > 0$), however upon failure, buckling occurs on the opposite (lower) side as shown in Fig. 4.16b. When the joint is sufficiently pressurized, the arm fails upon being loaded beyond the payload capacity via buckling of link 1 near joint 1 as shown in Fig. 4.16a. It is worth noting that unlike conventional robot structures, failure via

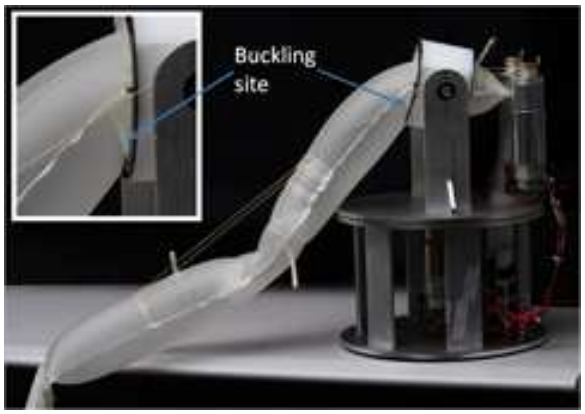

(a) Failure due to buckling of the inflatable link 1.

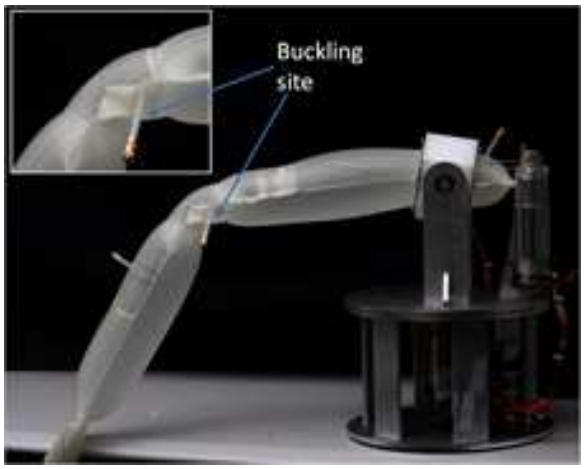

(b) Failure due to buckling of the inflatable joint. The inset figure shows buckling on the lower side of the inflatable joint.

Figure 4.16: Two modes for failure of the inflatable arm: a) Buckling of the inflatable link b) Buckling of the inflatable joint

buckling is temporary, i.e., the structure restores to its nominal shape and configuration once it is unloaded.

Impact Tests

To verify safety in terms of interaction forces during high velocity impacts, impact tests were conducted with the inflatable arm. For the test, the joint 2 motor was locked while the joint 1 motor was accelerated to different speeds. The arm impacted a fixed surface instrumented with a force sensor to measure impact forces (ATI Mini85). The torque at the joints contributes a significant percentage of the interaction force during impacts, as is evidenced by the static portion of Fig. 4.17.

As shown in Fig. 4.17, the maximum magnitude of the impact force even at velocities as high as 5m/s is $<$ 10N. For the sake of context, the zygoma (a facial bone) has a fracture force of approximately 614 N when impacted with a rigid surface [74]. The impact force levels are, therefore, well below the force levels that would cause injury to a human. The first author of this

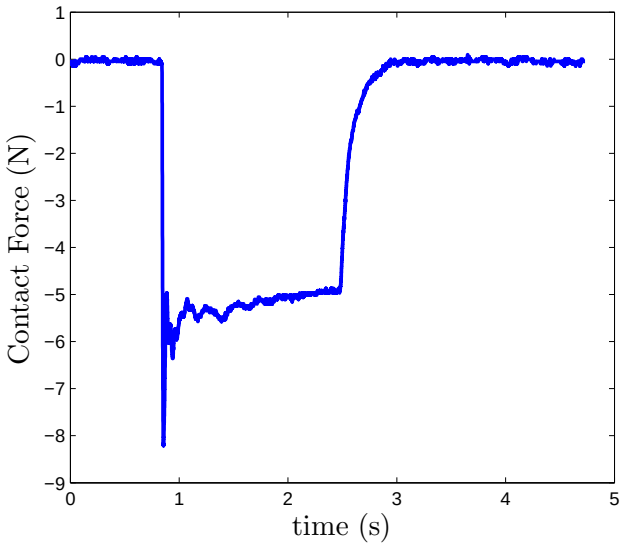

Figure 4.17: Contact force at 5 m/s tip velocity. The impacting surface normal was parallel to the tip velocity.

paper also volunteered to participate in an impact test which involved the end of the arm hitting the facial region (see accompanying video). For identical test conditions, as used in the experiment in Fig. 4.17, the subject reported no pain or physical discomfort during and after the test.

These results indicate two things: 1) the inflatable arm is capable of moving extremely fast while not posing any significant injury risk in terms of accidental impacts, and 2) arm inertia and stiffness can be significantly increased while still not violating safety constraints, implying that much larger safe manipulators can also be made using inflatable structures.

4.2 The PneuArm

The CMU inflatable arm is capable of handling payloads in the range of 0.5 kg which is sufficient for a wide range of assistive tasks feeding, wiping, grooming and other task which require picking up of small and light objects found in a domestic setting. However, higher payloads and even higher payload to weight ratios are possible by using different materials for the construction of

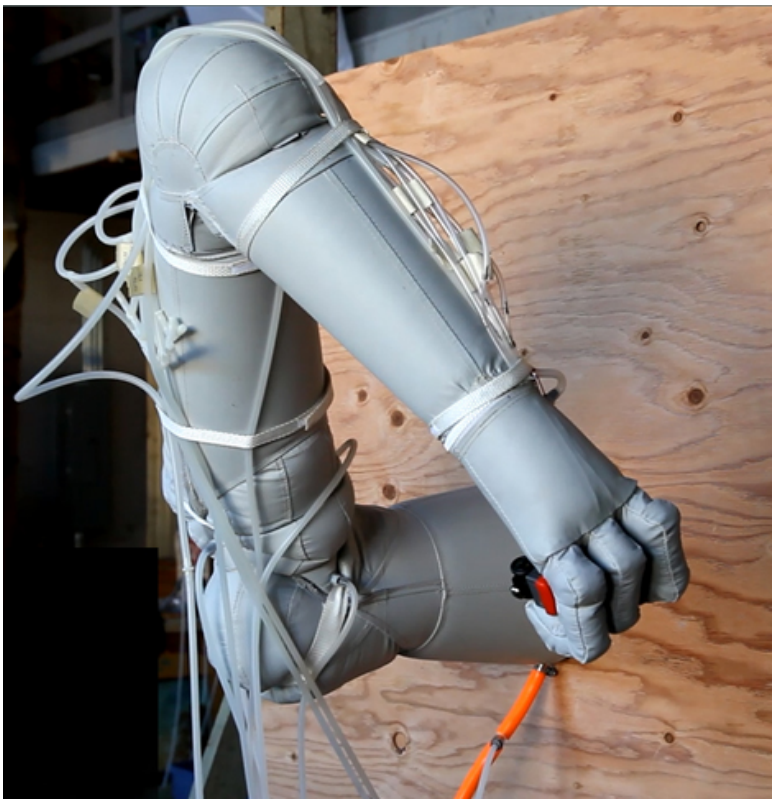

Figure 4.18: The PneuArm in a configuration near the extremity of its workspace.

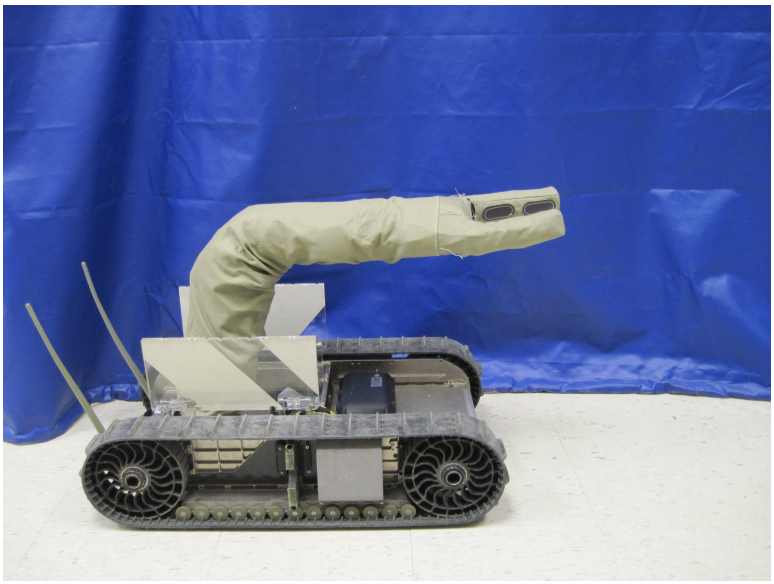

Figure 4.19: The two degree of freedom iRobot AIRarm uses an inflatable structure and electromechanical actuation.

the inflatable structure and compressive rather than tensile actuators. The PneuArm serves to demonstrate higher payload capacities with inflatable robots.

We will briefly describe the PneuArm here, for details refer Sec. 6.2. The PneuArm (see Fig. 4.18 and 4.1b) utilizes an inflatable structure with integrated pneumatic actuators. All inflatable components have an exterior fabric (high strength polyvinyl chloride (PVC) coated polyester) and an internal polyurethane bladder to pneumatically seal the components. The PneuArm has 3 DoFs that follow an anthropomorphic structure with 2 DoFs at the shoulder and 1 DoF at the elbow. The arm also has an inflatable hand with 3 fingers and 1 thumb at its end. The arm utilizes a flexure type joint where a restriction of the cross-section of the arm leads to the creation of a joint axis. The joints are actuated with antagonistic compressive pneumatic actuators that enclose the joint on either side. Further details regarding the PneuArm and its capabilities can be found in Chapter 6.

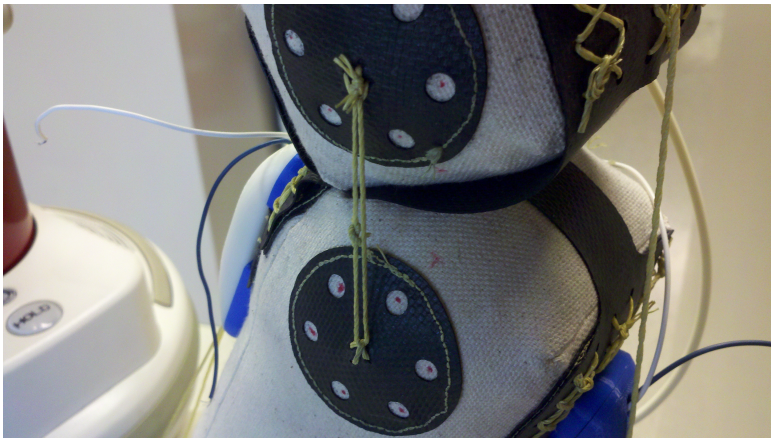

Figure 4.20: Rolling Flexure Joint.

4.3 The AIRarm

The AIRarm is hardware developed at iRobot as part of a collaborative effort with CMU. Some of the modeling and analysis work described in Chapter 8 was carried out for the AIRarm. The AIRarm (Fig. 4.19) is an electromechanically actuated 2 degree of freedom manipulator that has a gripper, the AIRHand, at the end. The system consists of two inflatable links that are coupled using the rolling flexure joints shown in Fig. 4.20. The links consist of a fabric exterior that is sewn into the desired shape of the links. For the purpose of inflation, each link has an internal polyethylene bladder. The fabric-bladder design allows the links to be inflated to high internal pressure due to the high strength of the fabric exterior material.

The rolling flexure joint (see Fig. 4.20) uses the idea of higher pairs to develop a joint functionally similar to a revolute joint. The idea also draws inspiration from the human knee joint which involves a higher pair actuated using tensile elements. The rolling flexure joint allows almost strain free motion of the joint and therefore the range of motion achievable can be very large. Joint loads are supported by the internal pressure at the contact surface of the joint, the surface area of contact increases as the joint load increases. The loads are supported in a way that is similar to the way car tires support loads via the tire contact patch.

Fig. 4.21 gives a geometric description of the rolling flexure joint. The joint consists of two

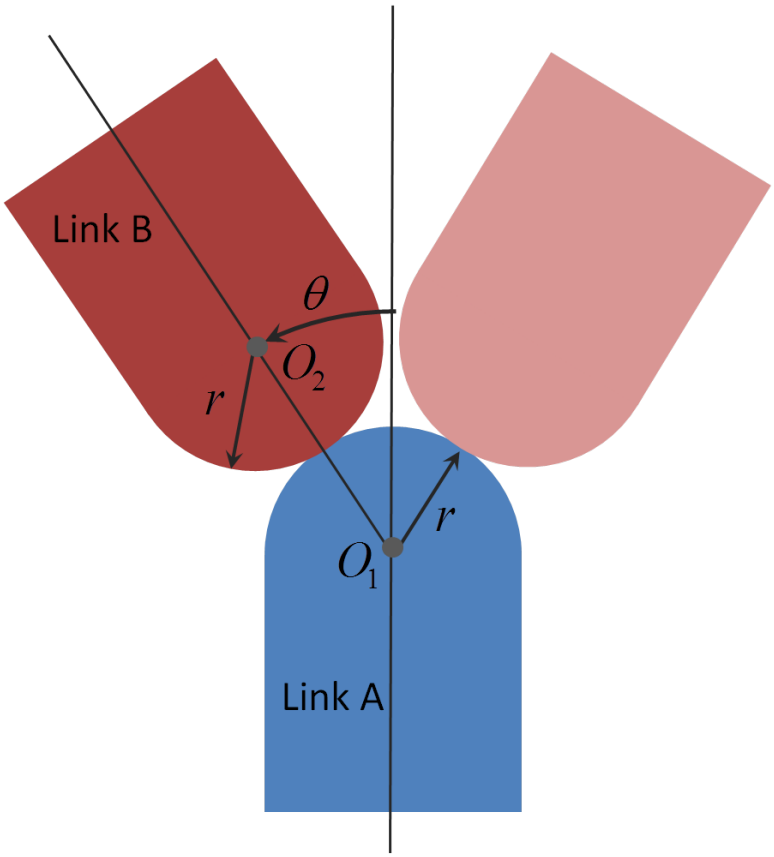

Figure 4.21: Schematic of rolling flexure joint.

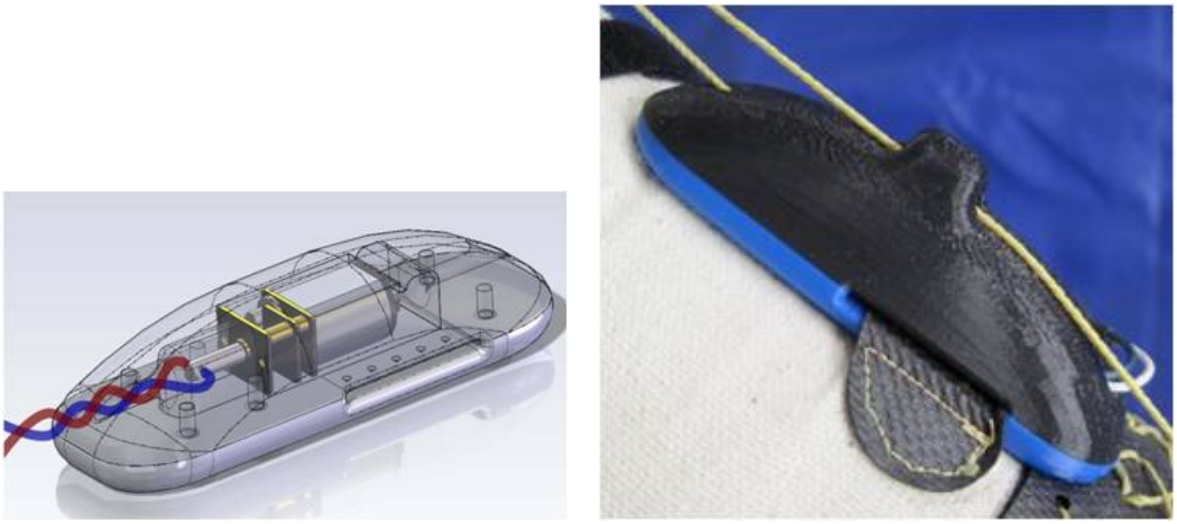

(a) (b)

Figure 4.22: Twisted string actuators used to actuate the rolling flexure joints

links (link A and link B) with cylindrical end surfaces. As the cylindrical surface of link B rolls over the cylindrical surface of link A, link B undergoes displacement. If the radii of the two cylindrical surfaces r are equal as in Fig. 4.21, the displacement of the link B is a pure rotation θ about the center of the cylindrical surface of link A, O_1.

The rolling flexure joint is actuated using twisted string actuators shown in Fig 4.22. The actuators use DC motors that twist a pair of strings as shown in Fig. 4.22a. The twisting motion results in contraction of the string length. These actuators have a very high gear ratio that depends on the diameter of the two strings.

4.4 Summary

In this chapter, various inflatable robot prototypes that were developed and/or utilized for this thesis are described. Actuation, link design, end effector, joint stiffness, transmission kinematics, and payload capacity and safety under impacts are discussed for the CMU inflatable arm. General design aspects of two other inflatable robots, the PneuArm and AIRarm, are also presented.

Chapter 5

Fabrication

In this chapter, we will briefly describe some of the fabrication techniques used to manufacture the inflatable robots described in this thesis. The fabrication methods are unconventional but not new and used regularly in other application areas besides robotics.

5.1 Thermal Welding

Figure 5.1: An impulse sealer used for generating straight seams between layers of plastic film

The primary inflatable structure of the CMU inflatable arm, the bladders of the PneuArm and AIRarm are fabricated by thermal welding of multiple layers of plastic film. The impulse sealer

shown in Fig. 5.1 was used for this purpose. This machine allows the manufacture of only straight seams between multiple layers of plastic film. Other machines such as the hot air welding machine shown in Fig. 5.2 can allow fabrication of curved seams by passing film that is heated using hot air between multiple rollers.

Figure 5.2: A thermal welding machine from Miller Weldmaster that uses hot air and rollers for generating straight and curves seams.

Fig. 5.3 shows the inflatable hand and the panels of polyurethane films used to construct the hand using thermal welding. The edges of adjacent panels are sealed together to build the 3D inflatable volume. It is also worth noting that it is possible to generate 3D volumes using shapes which are 2D when deflated. The primary structure of the CMU inflatable arm is an example of this. This can allow easier automated manufacturing of inflatable structures of robots while at the same time increasing speed and lowering cost of manufacturing.

5.2 Sewing

Sewing is another technique that is highly relevant to inflatable robots. The PnueArm and AIRarm both utilize structures which utilize high strength fabric that has been sewn into desired shapes.

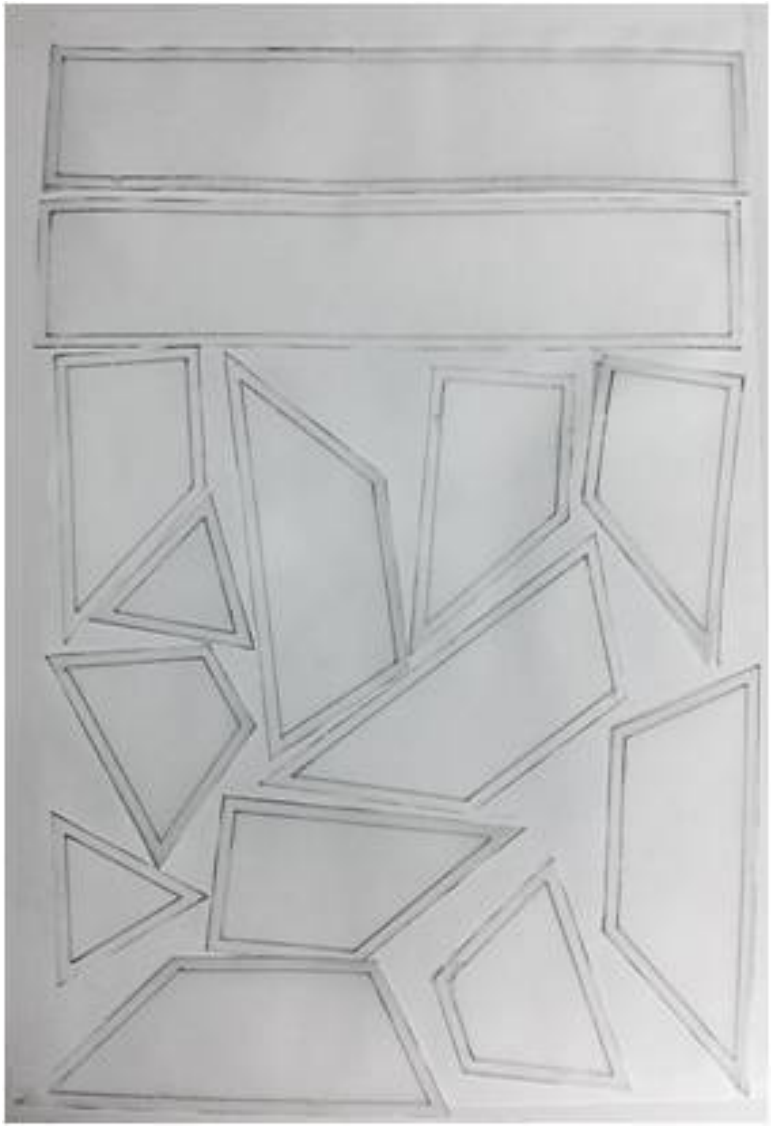

(a) Polyurethane film panels used to construct the inflatable hand

(b) Inflatable hand - open state

(c) Inflatable hand - closed state

Figure 5.3: The inflatable hand manufactured by thermal welding of polyurethane film

Figure 5.4: Sewing machines such as the one shown above can be used to sew fabric or textile materials into desired shapes for use in inflatable robots.

The volumes obtained by sewing are clearly not sealed and therefore need an internal bladder to make the volume air tight. The bladder is used to only make the structure air tight and not used for any structural strength. This is achieved by using a bladder which is bigger (approx. twice the volume) than the volume it is used to seal. Complex 3D volumes to be realized using fabric or textile like material at a cost comparable to that of making clothes.

One of the drawbacks of fabrication using sewing is that it hard to automate the process because automated CNC type sewing machines are not readily available for complex 3D parts. Development of automated tools for the manufacture of 3D inflatable volumes can benefit the long term acceptance of inflatable robots as a viable technology.

5.3 Other Methods

Besides thermal welding and sewing other methods can also be used to manufacture inflatable robots. We will relax our definition of an inflatable robot for the following subsections, which has through out this text implied robots made from materials which can only support tensile loads.

Seamless Knitting

Seamless knitting is another technique that can be used to manufacture inflatables with an outer fabric shell and bladder lining. This technique allows fabrication of 3D shapes and volumes without the use of cutting and sewing. The lack of seams in the structure implies an overall stronger structure, as failure in inflatable structures often occurs across the seams. The other advantage of seamless knitting is that process can be automated. Machines that can output seamless volumes are commercially available, see [18] for details.

5.4 Summary

This chapter discusses the various techniques that were used to fabricate the prototypes described in this thesis. Thermal welding and sewing are the two main techniques used. The fabrication techniques used are identical to that used to make clothes and inflatable pool toys. These fabrication techniques allow extremely low cost manufacturing of inflatable robots and can serve as an enabling factor to make personal robots accessible to large segments of the general population and researchers. Automation of the manufacturing process using 2D printing and lamination techniques and 3D printing and knitting techniques might be beneficial for future applications.

Chapter 6

Strength and Range of Motion

In this chapter, using a prototype inflatable manipulator the PneuArm, we will address the problem of designing inflatable manipulators with a large range of motion, high payload to weight ratios and high absolute payload capacity. The PneuArm is a pneumatically actuated inflatable manipulator with an anthropomorphic design. This work was carried out in collaboration with Otherlab Inc, San Francisco.

6.1 Introduction

In this chapter we present a novel inflatable manipulator, the PneuArm, that is completely soft. All elements, i.e, the structural and actuator components of the manipulator are built using membranes and are integrated into a single structure. The manipulator is actuated pneumatically and is capable of a very high level of dexterity and strength that have not been reported in previous inflatable manipulators. The payload to weight ratio of ≈ 2 for the PneuArm exceeds that of any commercially available traditional manipulator. While numerous challenges exist in terms of actuation, sensing and control, the prototype represents a significant step in terms of strength and range of motion for a manipulator that is completely soft. The function and form of the human arm served as a key

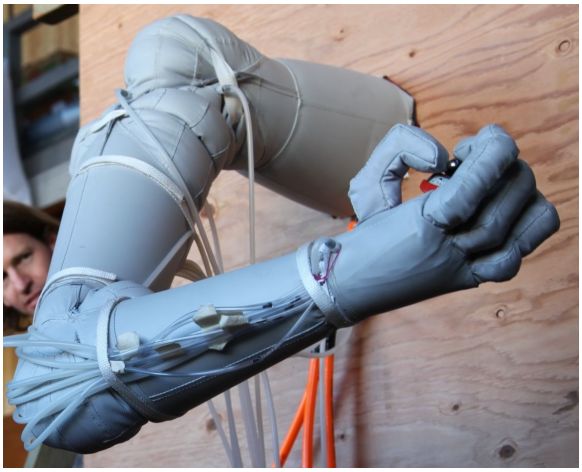

Figure 6.1: The prototype inflatable manipulator

inspiration to guide the overall design of the PneuArm.

The rest of the chapter is organized as follows. In Sec. 6.2, we describe the design of the primary structure, the joints, the actuators and the hand of the PneuArm. In Sec. 6.3, we present a model for controlling the actuators of the PneuArm. In Sec. 6.4 we provide some results on experimental characterization of the strength and range of motion characteristics of the PneuArm and in Sec. 6.5 we provide a brief discussion of our results. Finally, in Sec. 6.6 we provide some concluding remarks and future work.

6.2 Description of the PneuArm

The inflatable manipulator prototype, shown in Fig. 6.1, is constructed using commercially available textile fabric (PVC coated polyester fabric) that can be seen on the exterior and polyurethane bladders to pneumatically seal the structure for inflation. The manipulator is absent of any rigid elements (elements that can bear compressing and/or bending loads). The inflatable manipulator has similar functional components to that of a traditional manipulator; it consists of links serially connected via joints which are actuated allowing relative motion between the links. We will briefly describe the general specifications and realizations of the functional components of the PneuArm

next.

6.2.1 General Design

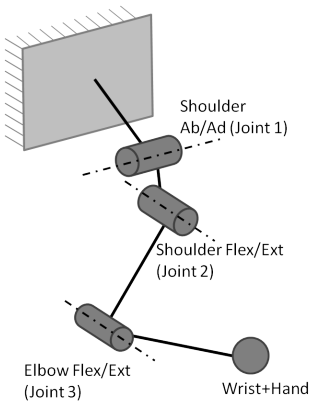

Figure 6.2: Kinematic representation of the PneuArm

The design goal for PneuArm was to achieve human like capabilities with respect to range of motion and payload capabilities, an anthropomorphic kinematic structure for the arm was therefore a reasonable choice. The anthropomorphic kinematic structure was achieved by placing two degrees of freedom at the shoulder (the shoulder abduction-adduction, and the shoulder flexion-extension) and one degree of freedom at the elbow (elbow flexion-extension), see Fig. 6.2. Note that certain DoFs that are present in the human arm are not implemented in this first version of the PneuArm. Specifically, the humeral rotate and elbow pronation-supination are omitted. This is because pneumatic actuators and inflatable structures to achieve such motion have yet to be developed. In a parallel effort, our group is developing such pneumatically actuated torsional actuators ([95]), to be incorporated into future versions of the PneuArm. Additional degrees of freedom at the hand are discussed later in Sec. 6.2.5. The overall size of the arm is chosen to be approximately that of a human arm.

Table 6.1: Parameters for Static Analysis of the PneuArm

Parameter	Value
Payload (F_p)	15 lbs (6.8 kg)
Moment arm (l)	1 m
Largest Cross-section (r_1)	7.5 cm
Fabric Thickness (t)	0.4 mm

6.2.2 PneuArm Payload Capacity

Given the shape and size of the PneuArm, its strength is determined by the internal pressure in its structure. The internal pressure within the structure defines the load at which surface wrinkling of the structure begins to occur due to the formation of compressive stresses. When surface wrinkling occurs the stiffness of the arm abruptly drops ([64, 122]). This type of failure, which we will refer to as *overloading* is completely reversible for inflatable structures and represents another advantage of inflatable structures over traditional structures. The maximum internal pressure within the structure is limited by the fabric seam strength and the presence of stress concentrations in the structure. As the PneuArm consists of multiple links connected at location to form joints, the presence of stress concentrations cannot be avoided, at least with current prototyping methods. When the structure is over-inflated beyond the maximum pressure the structure fails abruptly by tearing apart at the seams, usually accompanied by a loud explosion due to sudden expansion of the pressurized air in it.

The operating pressure of the arm is based on the desired payload, F_p for the PneuArm. The calculations are applied at the fully stretched configuration of the arm. It is important to verify that the computed operating pressure is within the experimentally identified maximum achievable pressure for the structure. For the sake of clarity, the equations used to compute operating pressure P_{op} for the first link of the PneuArm are presented below; it is assumed that the links assume a

Table 6.2: Geometric Parameters of the PneuArm

Link	Length (cm)	D_1 (cm)	D_2 (cm)
Upper Arm	60	15	12
Lower Arm	40	12	80

circular cross-section:

$$\sigma_b = \frac{F_p l}{\pi r_1^2 t} \tag{6.1}$$

$$P_{op} = \frac{\sigma_b 2t}{r_1} \tag{6.2}$$

where σ_b is the bending stress due to the payload, l is the length of the moment arm, r_1 is the radius of the cross-section of link 1 at the base, t is the thickness of the fabric material used in the construction. Substituting the parameter values listed in Table 6.1 into (6.1) and (6.2) leads to an operating pressure of ≈ 15 psi. From our experimental testing it was determined the maximum internal pressure before the structure fails is $P_{max} \approx 25$ psi. Since $\frac{P_{op}}{P_{max}} < 1$ we can safely operate the arm at $P_{op} = 15$ psi.

The links of the PneuArm consist of tapered cylindrical sections. The cross-sectional diameter of the links was derived using equations identical to (6.1) and (6.2), based on desired payload capacity, maximum pressure constraints and thin walled pressure vessel theory. Table 6.2.2 provides the geometric parameters for PneuArm. The overall size of the arm is slightly larger than that of the human arm.

6.2.3 Joints

Figure 6.3 shows the construction of the three joints of the PneuArm. The first two joints provide two rotational degrees of freedom at the shoulder and the third joint provides a single degree of rotation at the elbow. All three joints approximate revolute joints allowing rotation about a single axis. Clearly, the realization of a revolute joint for an inflatable structure is very different from

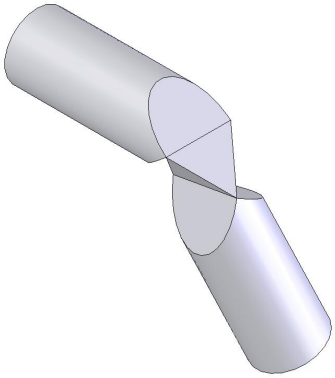

(a) The shoulder joints.

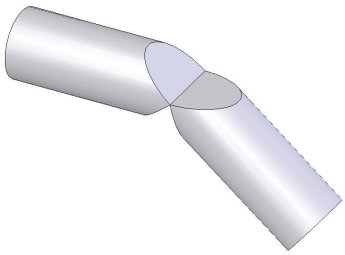

(b) The elbow joints.

Figure 6.3: CAD drawings of the PneuArm joints.

that between two rigid bodies. While it is theoretically possible to construct cylindrical bearing surfaces to implement a revolute joint, it is more feasible to use a flexure based approach. This is especially true because the tensile nature of the structural material used to construct inflatables allows the formation of near zero stiffness flexure type joints. The joints only need to support tensile loads because we use compressive rather than tensile actuators.

The geometric design of the joint is based on the range of motion requirements for the joint. Both the joints at the shoulder, i.e, joint 1 and joint 2 have equal range of motion and strength in both clockwise and anticlockwise directions. In keeping with the general anthropomorphic design of the PneuArm, the elbow has an asymmetric range of motion (130° in the clockwise (+ve) direction and 15° in the anti-clockwise (-ve) direction). The elbow joint was also designed to have asymmetric strength in the two directions.

The design parameters that describe the geometry of the joints are shown in Fig. 6.4. For

all symmetric joints the hinge offset $s = 0$ and $\alpha_{ag} = \alpha_{ant}$. α_{ag} and α_{ant} are simply the range of motion for the agonistic and antagonistic actuators. Note that in Fig. 6.4, the agonistic actuator is the actuator that will be placed on the lower side of the joint to provide counter-clockwise torque/motion about joint. The offset s is used to change the relative strength of the agonistic and antagonistic actuator. We will explain this mechanism further when we describe the actuator for the joints in later sections.

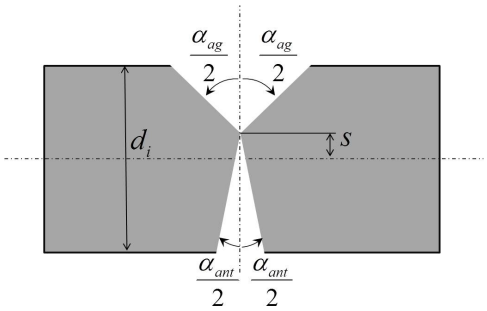

Figure 6.4: Geometric parameters of the PneuArm joints.

6.2.4 Actuators

The actuators for the PneuArm are compressive type pneumatic actuators, i.e, as the actuators are inflated they generate compressive rather than tensile forces. As shown in Fig. 6.5, each actuator is constructed by forming an enclosed volume at the joint by sewing cover panel across the joint. When the enclosed volume is inflated, pressure is exerted over the actuator pressure surface resulting in a torque about the joint axis. The cover panels of the actuator are constructed so that the actuator, in its nominal state, assumes a shape that corresponds to the fully extended state of that joint. For example, in Fig. 6.5, the agonistic actuator in its nominal state assumes a shape such that the elbow is at the range of motion limit for the agonistic motion i.e $\theta_{elbow} = \alpha_{ag}^{elbow}$, where θ_{elbow} defines the configuration of the elbow joint. Every agonistic actuator has a corresponding antagonistic actuator which is constructed around the opposite side of the joint. This allows bidirectional torque at the joint and allows stiffness variation at the joint commonly

associated with such antagonistic-agonistic actuator pairs.

For joints 2 and 3 of the PneuArm, the actuator pressure surface (shown in Fig. 6.5) is formed by the intersection of a cylinder and a plane at an angle based on the range of motion. The surface area A and radial distance of the centroid from the joint axis r of the elliptical surface influence the torque characteristics of the actuator. More specifically the product of A and r is directly proportional to the torque produced by the actuator, this is given by

$$Ar = \begin{cases} \frac{1}{12}\sec\left(\frac{\alpha}{2}\right)(L-M), & \text{if } s \geq 0 \\ \frac{1}{12}\sec\left(\frac{\alpha}{2}\right)(L+N), & \text{if } s < 0 \end{cases} \tag{6.3}$$

where

$$L = (d^2 + r^2 + r^2\cos\alpha)\sqrt{-4r^2 + d^2\sec^2\left(\frac{\alpha}{2}\right)} \tag{6.4}$$

$$M = 3d^2 r\cos^{-1}\left(\frac{2r\cos\left(\frac{\alpha}{2}\right)}{d}\right) \tag{6.5}$$

$$N = 3d^2 r\sin^{-1}\left(\frac{2r\cos\left(\frac{\alpha}{2}\right)}{d}\right) \tag{6.6}$$

From (6.3)-(6.6), it can be observed that for the case when $s > 0$, the actuator torque is a monotonically decreasing function of s and for the case $s < 0$, the actuator torque monotonically increases with $|s|$. Consequently the relative strength of the antagonistic and agonistic joints can be varied by changing the offset s in an asymmetric joint whose range of motion is equal in both directions. In the above equations, the subscripts for α has been omitted for the sake of simplicity.

In certain cases, such as joint 1 of the PneuArm, the actuator pressure surface is a triangle. In this case, assuming $s = 0$, the resulting expression for Ar is straightforward to derive and is given by

$$Ar = \frac{d^3}{24\cos^2\left(\frac{\alpha}{2}\right)} \tag{6.7}$$

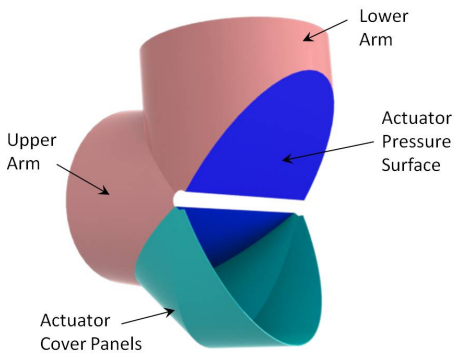

Figure 6.5: Actuator construction for agonistic actuator at the elbow joint.

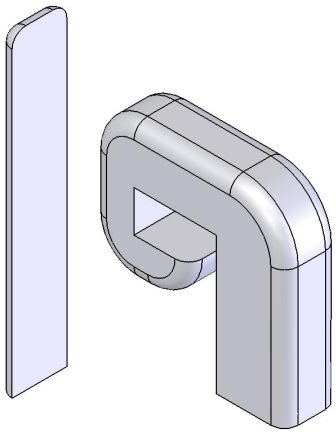

Figure 6.6: CAD model of the two inflatable chambers used to construct the finger. When the finger is in the open state the chamber shown on the left is inflated and to bring the finger to the closed state the chamber on the right is inflated.

6.2.5 Hand

In inflatable structures, it is possible to combine two differently shaped closed volumes (e.g., two shapes S_1 and S_2) into a single structure along a common geometric feature. The resulting structure can take the shape of either structure depending on which one is pressurized. Intermediate shapes can also be achieved by simultaneously inflating both the volumes. We use this principle to replicate the form and function of human fingers for the PneuArm hand. The model governing the shape of the structure during simultaneous inflation of both volumes can be complex due to the

(a) Finger in open state. In this state, the volume which has the shape of an open finger is pressurized while the other volume is deflated.

(b) Finger in closed state. In this state, the volume which has the shape of a closed finger is pressurized while the other volume is deflated.

Figure 6.7: The individual fingers that form the PneuArm hand.

(a) Hand with all fingers in the open state

(b) Hand with one finger in the closed state

Figure 6.8: Three fingers and a thumb are integrated to form the PneuArm hand.

occurrence of wrinkling. We will not explore the problem of predicting intermediate shapes in this chapter. It should be noted, that we use a similar idea for actuating the joints of the arm as well. While the shapes of the two actuators needed for the joints of the arm have parametric variation, the variation between the shapes is more general for the fingers of the PneuArm hand.

The finger is divided lengthwise into two closed volumes. The CAD model of two volumes are shown in Fig. 6.6. The shape of one volume is consistent with a straight finger as shown in Fig. 6.7a; the second volume is shaped like a finger in its closed state as shown in Fig. 6.7b. By differentially inflating the two volumes it possible to change the shape of the finger between the open and closed states. Since the actuation is in the space of *shapes*, it allows us to eliminate the need for a multi-joint actuation method for the fingers. This is particularly useful given the current sewing techniques used for prototyping which have serious limitations at smaller scales.

Figure 6.9: 1 DoF joint-actuator model.

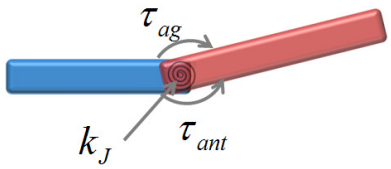

6.3 Actuator Modeling and Control

Fig. 6.9 shows a schematic of a 1 DoF joint actuator model that can be utilized for position control of the joint. The actuators are considered as torque sources applying torques τ_{ag} and τ_{ant} at the joint. The joint has an intrinsic torsional stiffness k_J due to its geometry and internal pressure. k_J can be approximated experimentally. The agonistic and antagonistic torques can be given by:

$$\tau_{ag} = P_{ag} A_{ag} r_{ag} \tag{6.8}$$

$$\tau_{ant} = P_{ant} A_{ant} r_{ant} \tag{6.9}$$

where A_{ag} and A_{ant} are the cross-sectional areas of actuators, r_{ag} and r_{ant} are the radial distance of the centroid of A_{ag} and A_{ant} from the joint axis of rotation. The product Ar is the same as that given by (6.3) and (6.7). The integrated model of the joint is given by:

$$\tau_{ant} - \tau_{ag} + k_J \theta + \tau_{ext} = 0 \tag{6.10}$$

where θ is the angle of the joint, and τ_{ext} is the external torque at the joint. Defining $C = Ar$ and using (6.8) and (6.9), the relation between the pressure differential of the antagonistic actuators ΔP, the joint angle θ, and the external load τ_{ext} can be derived:

$$P_{ant} C_{ant} - P_{ag} C_{ag} = -k_J \theta - \tau_{ext} \tag{6.11}$$

$$\Rightarrow \Delta P = \frac{(-k_J \theta - \tau_{ext})}{C_{ag}} \quad \text{assuming} \quad C_{ag} = C_{ant} \tag{6.12}$$

For joints with symmetrical actuators $C_{ag} = C_{ant}$. The pressure differential ΔP in (6.12) can be used as the feedforward term in a feedforward + feedback control scheme for controlling the position of the joint.

To completely determine the pressure in both the actuators we need another relation between the pressures P_{ag} and P_{ant}. This additional relation can be obtained by specifying a desired stiffness of the actuators.

Actuator Stiffness

To compute the actuator stiffness, we will assume all the valves (fill and exhaust) for both the actuators are closed. The stiffness of the actuators is due to compression/expansion of the air in the actuators as the joint deflects from its nominal position. For the sake of simplifying our discussion we shall assume isothermal expansion of air, as temperature effects can be ignored at the time-scale of our analysis. The torque at the joint τ_{def} due to a deflection θ_{def} at the joint can be given by:

$$\tau_{def} = \frac{P_{ant} V^i_{ant}}{V^i_{ant} + C_{ant}\theta_{def}} C_{ant} - \frac{P_{ag} V^i_{ag}}{V^i_{ag} + C_{ag}\theta_{def}} C_{ag} \tag{6.13}$$

where V^i is the initial volume. Assume P_{ag} and P_{ant} have the following form:

$$P_{ag} = P_0 + P_1$$

$$P_{ant} = P_0 - P_1$$

Then, for joint angle $\theta = 0$, if the actuators are symmetric and unloaded $V^i_{ag} = V^i_{ant}$, $C_{ag} = C_{ant}$ and $P_1 = 0$ (using 6.12). This leads to the following simplified expression for the deflection torque (omitting subscripts and superscripts where unnecessary):

$$\tau_{def} = -\frac{2C^2 P_0 \theta_{def}}{V^2 - C^2\theta^2} \tag{6.14}$$

Differentiating (6.14) w.r.t θ_{def} gives the stiffness of the joint:

$$\frac{-\partial \tau_{def}}{\partial \theta} = k_{act} = \frac{2C^2 P_0 V^2 + C^2 \theta^2}{(V^2 - C^2 \theta^2)^2} \tag{6.15}$$

The pressure P_0 can be computed using the linearization of (6.15) about $\theta_{def} = 0$:

$$P_0 = k_{act} \frac{V^2}{2C^2} \tag{6.16}$$

Using (6.16) and (6.12) along with a stiffness specification k_{act}, the pressure parameters P_0 and P_1 for the joint can be determined.

6.4 Characterization

The PneuArm prototype was evaluated for kinematic and strength features. The results of the evaluation are discussed below (for a demonstration of these capabilities please refer to the accompanying video[1]).

Joint Range of Motion:

- Shoulder Ab/Ad: $\approx 180^\circ$
- Shoulder Flex/Ext:$\approx 180^\circ$
- Elbow Bicep/Tricep: $\approx 150^\circ$

Maximum Achieved Internal Pressure: 15 psi

Maximum Tested Payload at Full Stretch: 2.25 kg

The arm was tested for a payload of 2.25 kg at the extremities of its workspace. Fig. 6.11 shows the arm lifting a 10 lb (4.54 kg) dumbbell. It is able to this by coordinating the motion of its

[1] www.cs.cmu.edu/~ssanan/otherlab/video

(a)

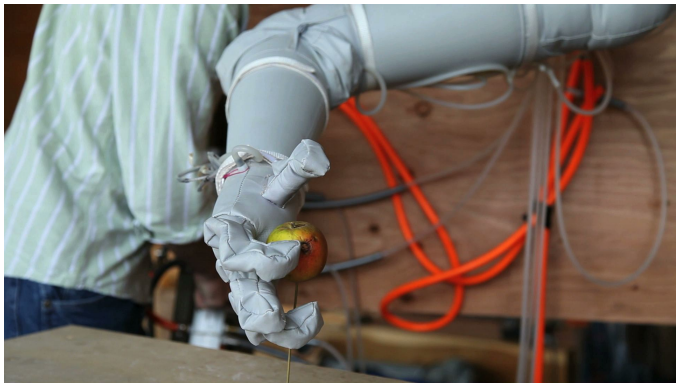

(b)

Figure 6.10: Arm prototype lifting a weighted bucket and grasping an apple.

shoulder and elbows to reduce the moment arm on the overall structure. Fig. 6.12 shows the arm in a configuration near the extremity of its workspace, the elbow flexion and shoulder abduction actuators are near the joint range of motion limits. Fig. 6.13 shows the shoulder abduction-adduction (joint 1) range of motion. It should be noted that there is some loss of range of motion in the joint because as one actuator at the joint is inflated the other needs to wrinkle in order to accommodate the joint motion. This leads to some resistance due to the finite volume of the wrinkled fabric of the opposing joint. To compensate for this, all the joints actuators were designed for a slighter larger range of motion than the design specification.

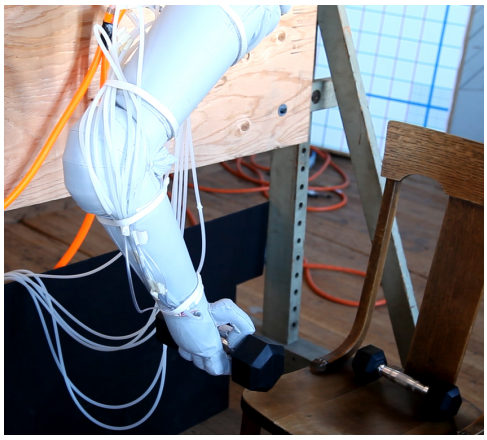

Figure 6.11: The PneuArm lifting a 10lb dumbbell.

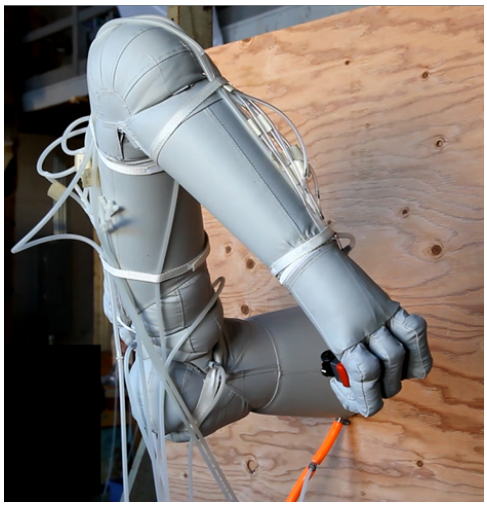

Figure 6.12: The PneuArm in a configuration near the extremity of its workspace.

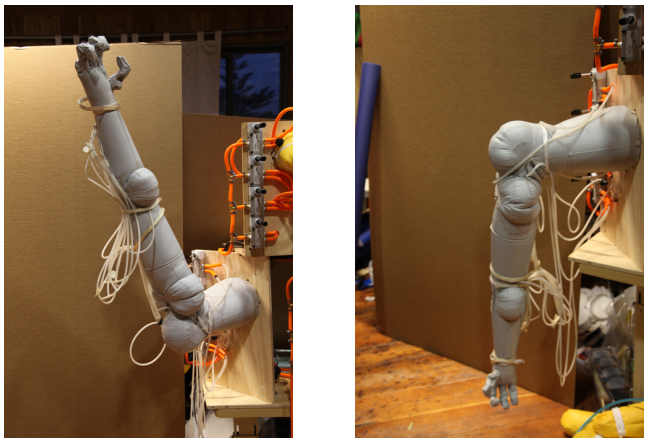

(a) (b)

Figure 6.13: The PneuArm shoulder Ab/Ad joint close to the extremities of its range of motion

6.5 Discussion

Diminishing the influence of wrinkling on the actuator characteristics is a key factor in improving characterization efforts and repeatability of the PneuArm. Another key area of improvement is the maximum angular velocity at the joints. In the current actuators for the shoulders and elbows, as the actuator inflates the joint angular velocity decreases as a result of the decreasing inlet pressure gradient. This may be overcome by the use of hydraulics instead of pneumatics for actuation along with a positive displacement pump.

Further characterization also needs to be carried out to determine the deformations in the joints and structure under the influence of an external load. This is necessary because the motion of the system is affected by the payload being manipulated and the operating pressure of the main structure and the actuators. The list below provides some of the features that need to be characterized:

- Joint stiffness
- Link stiffness
- Maximum joint angular velocity
- Arm inertia

The above characterizations will help build a more complete model of the arm suitable for developing control schemes for the whole arm. Besides characterization for modeling, performance metrics to evaluate the developed controlled schemes are needed, some of these are listed below:

- Joint position accuracy
- Tip position accuracy
- Joint trajectory tracking performance
- Tip trajectory tracking performance
- Joint torque control performance
- Tip impedance control performance

6.6 Summary

In this chapter, we have presented a dextrous, high payload, and high payload-to-weight ratio inflatable manipulator, the PneuArm. The inflatable manipulator represents a significant step in our understanding of designing and manufacturing inflatable robotic systems with high strength. With a manufacturing process as simple as sewing we succeeded in developing a manipulator that is complex enough to be 'human-like'. The arm has a payload-to-weight ratio of ≈ 2 and an absolute mass of ≈ 1 kg. Actuator and joint models for joint based position control of the arm were also developed. A novel hand that resembles the human hand in form and function is also shown and initial experiments have shown it to be capable of grasping a variety of objects.

One of the limiting factors that affects the overall payload capacity of the system is the maximum pressure that the system can be inflated to. Though this is currently limited by our manufacturing process, the ultimate reason to limit the maximum pressure within the structure is due to safety concerns. If the energy stored in the inflatable chambers in the form of compressed air is too

high, this could lead to potentially dangerous high energy loud explosions. One way to minimize such safety hazards is to divide the inflatable structures into multiple chambers that have significantly smaller volumes. This is a possible future direction for inflatable robots to achieve even greater strength and reliability. Another important direction for future research is the development of valve technology for actuating these systems. The valves are currently placed away from the arm and are the only rigid components needed to run the PneuArm. Lightweight and soft valve technology that integrates in a more seamless manner with pneumatically actuated inflatable robots would be highly beneficial to inflatable robotics.

Chapter 7

Pneumatic Actuators for Inflatable Robots

This chapter discusses a variety of novel fluidic or pneumatic actuators to generate rotary motion for inflatable robots. These actuators differ from linear actuators such as the McKibben actuators utilized for the prototype in Chapter 4, Fig. 4.6 and from the compressive actuators used to drive the Pneuarm in the previous chapter, as they provide rotary motion along the axial direction of the actuator. While pneumatic artificial muscles (PAMs) that can generate linear motion have been researched and developed fairly extensively, little effort has been devoted to develop simple actuators that can provide rotary motion. A variety of possible designs and principles are discussed to achieve such rotary motion, along with accompanying analysis to understand motion and torque characteristics of each actuator. Experiments with prototype actuators validate performance expectations of each design.

7.1 Introduction

The dominant actuation method for most robots in the past has been electro-magnetic rotary actuators or motors. These actuators tend to be heavy, adding mass and inertia to the system. For robots that need to function in human environments and physically interact with humans the actuator

weight and inertia present a challenge from the safety perspective. Although various techniques, like Series Elastic Actuation and similar approaches [89, 137] have been proposed to hide the high inertia of the actuators, these actuators still present a fundamental limitation in terms of the weight of the robots. Besides lightweight actuation, there has also been a demonstrated need for Variable Impedance Actuators (VIAs) to satisfy safety and performance requirements of robots [8]. Pneumatic Artificial Muscles (PAMs) are a promising solution for providing lightweight actuation with variable impedance.

Numerous examples of PAMs exist today, mostly for providing linear actuation. The McKibben actuator [100, 19] is probably the most extensively used and studied PAM and can be setup in antagonistic actuation scheme to allow position and stiffness control of the actuator. [23] provides an extensive review of the numerous other type of PAMs that exist. While a number of these actuators were developed in the past for actuating rigid robots, the application of pneumatic actuation principles to develop soft robots has seen an increasing interest recently [55, 102].

We are interested in developing simple pneumatic actuators that can provide direct rotary motion, like that needed to generate a twisting motion at the wrist of the PneuArm inflatable manipulator [96] shown in Fig. 7.1 that is being developed by our group. Pneumatic actuators can integrate seamlessly with an inflatable manipulator such and this was our primary consideration for choosing pneumatic 'skin-based' actuators. Very little effort has been devoted in the past to develop actuators that can provide such direct rotary motion and we hope to advance the design space of such actuators. Recently, a carbon nanotube actuator that provides such motion for micro-scale applications was reported in [30]. We will refer to actuators providing direct rotary motion as *torsional* actuators because these actuators deform torsionally along their length. It should also be noted that because our application domain is inflatable robots, our goal is to develop torsional actuators *without* the use of any rigid components.

In the following sections we will describe the design and analysis of three novel pneumatic torsional actuators along with accompanying prototypes. The first actuator design uses the concept of

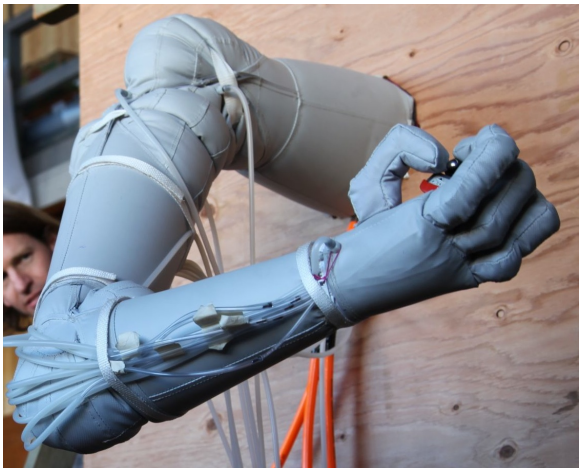

Figure 7.1: The PneuArm inflatable manipulator prototype [96]

shape actuators. Shape actuators assume different shapes based on the specific inflatable structure that is inflated. For the second design, we will use the concept of *Peano* actuators, which we will briefly explain in Section 7.3.1. The third actuator uses fibers asymmetrically arranged along the length of the actuator structure to constrain its motion in a way that results in a rotary motion at one end of the actuator. This chapter does not aim to provide a detailed experimental analysis of all the actuators but serves to explore the design space of torsional actuators with accompanying analysis to understand its behavior.

7.2 Antagonistic Torsion Shape Actuators

7.2.1 Principle

In membrane based structures, it is possible to combine two differently shaped structures (e.g., two shapes S_1 and S_2) into a single structure (having shape S) along a common geometric feature. The resulting structure can take the shape of either structure depending on which one is pressurized and can also interpolate between the two shapes (however the interpolation models can be complex because of the presence of wrinkling). This principle can be also be used to make fluidic torsional

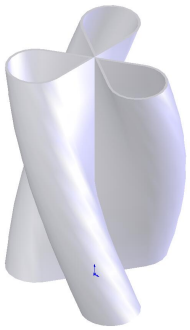

(a) Shape S_1: Left Helix

(b) Shape S_2: Right Helix

Figure 7.2: The two oppositely oriented helix that make up the rotary shape actuator

actuators by combining two oppositely oriented helix like structures shown in Fig. 7.2a and Fig. 7.2b into a single structure. The two helix in Fig. 7.2 are joined along the common geometric feature which is the central axis of the two shapes. The resulting merged structure is shown in Fig. 7.3.

7.2.2 Torque-Displacement Characteristics

To compute the static torque-displacement characteristics of the actuator, we will first compute the volume function $V(\alpha)$ of each helix shape as a function of the end rotation α. To do this, we will assume each 'leaf' of the helix has a circular cross-section when inflated. The volume for each helix actuator is then given by:

$$V(\alpha) = n\pi r^2 \sqrt{(\alpha r)^2 + l^2} \tag{7.1}$$

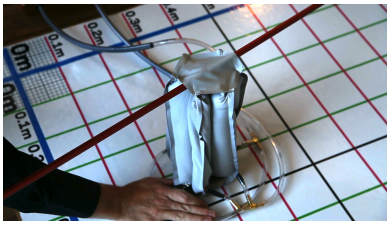

(a) Nominal configuration

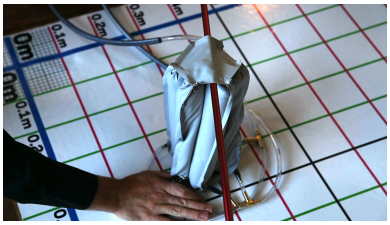

(b) Inflated configuration

Figure 7.3: Shape morphing twist actuator

where n is the number of leaves in the helix actuator (in Fig. 7.2 $n = 3$), r is the pitch circle radius of the helix and the radius of the cross-section of each leaf, and l is the length of the actuator. The torque function for the actuator can then be computed by taking the derivative of (7.1) and using the virtual work principle. We will derive the expression for the Right Helix here, the expression for the left helix can be similarly derived:

$$\delta W_\tau = \delta W_P + \delta W_s \tag{7.2}$$

$$\begin{aligned} \implies \tau_r &= P_r \frac{dV}{d\alpha_r} + \frac{dW_s}{d\alpha_r} \\ &= P_r \frac{n\pi\alpha_r r^3}{\sqrt{\alpha_r^2 r^2 + l^2}} - \frac{2\pi n r^3 t G(\alpha_r - \alpha_0)}{l} \end{aligned} \tag{7.3}$$

Above, δW_τ is the virtual work associated with the external torque τ, δW_P is the virtual work associated with the internal pressure P, δW_s is the virtual work due to the strains induced in the fabric, and α_0 is the initial or natural end rotation of the helix. It should be noted that the above analysis is only true for $\alpha_r < \alpha_0$. This is because we assume the actuator is made from fabric material which is inextensible and for $\alpha_r > \alpha_0$ the fabric needs to stretch. As a result, for inextensible

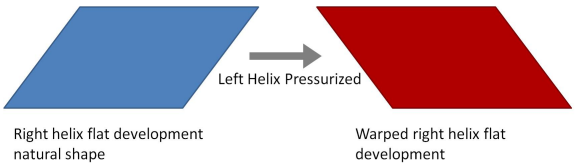

Figure 7.4: Flat development of helix during actuator motion

fabric material, the right helix will produce no torque for $\alpha_r > \alpha_0$.

Similarly, the torque displacement for the Left Helix is given by:

$$\tau_l = P_l \frac{n\pi\alpha_l r^3}{\sqrt{\alpha_l^2 r^2 + l^2}} - \frac{2\pi n r^3 t G(\alpha_l + \alpha_0)}{l} \tag{7.4}$$

The position of the actuator at any given actuator pressures P_l and P_r can be found by solving (7.3) and (7.4) for α_r or α_l. Note that α_r and α_l are related by the compatibility condition $\alpha_l = -\alpha_r$.

W_s is present in (7.2) because each helix actuator (say, the right helix) is warped into a helix actuator of the opposite shape when the other helix actuator (say, the Left Helix) is pressurized. An approximation of what happens to the fabric during this warping is that the fabric shears. This is easier to visualize using the flat development of the helix leaf, shown in Fig. 7.4. This is only an approximation to the true strains occurring in the fabric for the sake of a reasonably tractable analysis. In reality the fabric also wrinkles, however we neglect such complex phenomena. Another interpretation of the strains is that each leaf undergoes torsion, both interpretations are equivalent.

Fig. 7.5 shows the torque displacement characteristic for the right helix of an example torsion actuator. The parameters for the example actuator are: $n = 3$, $r = 0.025$ m, $l = 0.2$ m, $G = 76.9x10^6$ Pa, $P_r = 10.0$ psi, $t = 0.0005$ m.

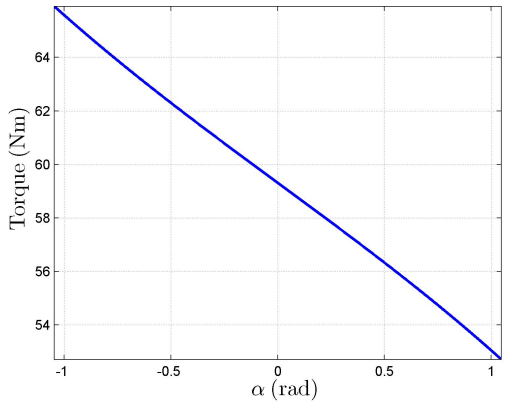

Figure 7.5: Example torque displacement characteristics for the right helix of a torsion shape actuator

7.3 Rotary Peano Actuators

7.3.1 Peano Actuators Review

The rotary Peano actuators described in this chapter will use the same operating principle of the linear Peano actuators. We will therefore briefly review the operating principle of Peano actuators.

Peano actuators utilize the contraction occurring over the width of a long tube when it is inflated, as described in Fig. 7.6. The actuators are constructed by connecting a number of such tubes along their length as shown in Fig. 7.7. The maximum theoretical contraction ratio for such actuators is ≈ 0.64, i.e, $\frac{l_{inf}}{l_{def}} = 0.64$. While the number of tubes/coils in the actuator does not affect the contraction ratio of the actuator (with all other parameters held constant), increasing the number of tubes/coils increases the efficiency of the actuator, in terms of the ratio of work output to work input.

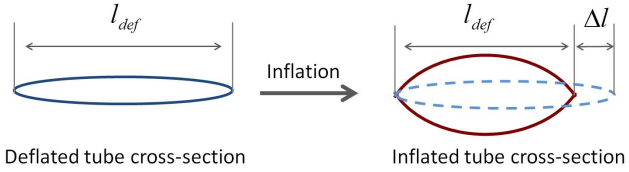

Figure 7.6: Contraction principle used in Peano actuators

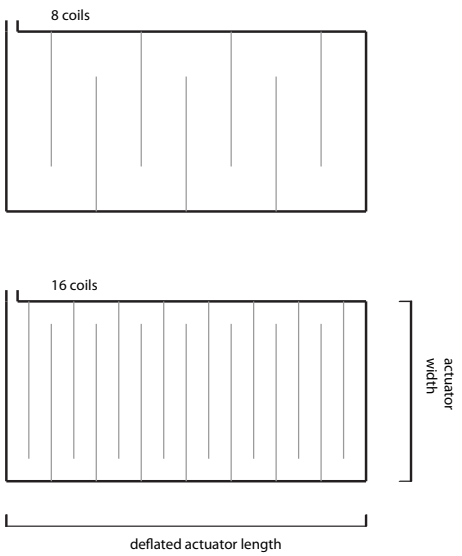

Figure 7.7: Peano actuators with different number of tubes or coils. For both the actuators shown here the actuator length contraction is identical.

7.3.2 Design

Rotary Peano actuators use the same contraction principle of the linear Peano actuators described in the previous section. Rotary motion is generated by virtue of their helical arrangement on a cylinder as shown in Fig. 7.8. The structure is closed at both ends and the cylindrical shape is maintained by internal pressure. As we shall observe, the effect of the pressure in the main cylinder is important to generate rotary motion at the end of the cylinder.

7.3.3 Actuator Motion

No external constraints

We will first consider the motion of the actuator resulting only from the contraction of the tubes and the geometry of the actuator. This implies we ignore any effects such as resistance to diametric contraction and length contraction of the actuator due to internal pressure of the large cylinder and end conditions of the actuator. We will assume the actuator remains cylindrical through out its

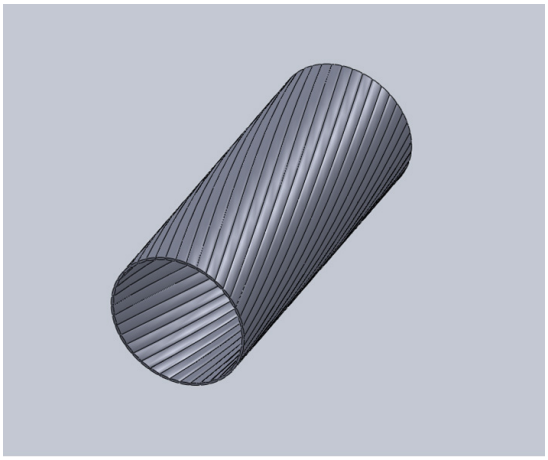

Figure 7.8: Peano Actuators on the Skin

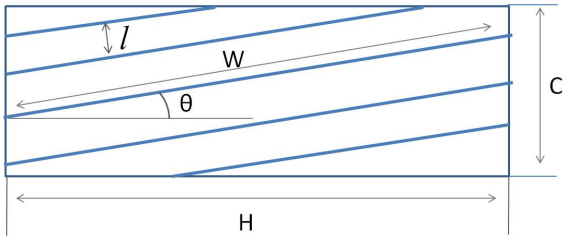

Figure 7.9: Geometric parameters of the rotary Peano actuator

motion.

The goal of the analysis below is to compute the end rotation obtained due to the width contraction of each tube in the actuator when it is inflated. Fig. 7.9 shows the geometric parameters of the actuator when the actuator is cut along its length and flattened. C is the circumference of the actuator large cylinder, l is the deflated width of each small tube in the actuator, W is the length of the small tubes, H is the height of the actuator and θ is the helix angle that defines the orientation of the small tubes on the actuator large cylinder. α is the angle between the two ends of the actuator. The following relationships can be defined between the various geometric parameters of the actuator:

$$C = \frac{n_v l}{\cos\theta} \tag{7.5}$$

$$H = \frac{n_h l}{\sin\theta} \tag{7.6}$$

$$\alpha = \frac{2\pi W \cos\theta \sin\theta}{n_v l} \tag{7.7}$$

$$\theta = \cos^{-1}\frac{H}{W} \tag{7.8}$$

where,

$$n_v = \frac{C_{def}\cos\theta_{def}}{l_{def}}$$

$$n_h = \frac{H_{def}\sin\theta_{def}}{l_{def}}$$

Assuming the contraction ratio $\frac{l_{inf}}{l_{def}} = 0.64$, the following relations follow for the inflated actuator:

$$\begin{aligned}\theta_{inf} &= \cos^{-1}\frac{H_{inf}}{W} \\ &= \cos^{-1}\frac{0.64\cos\theta_{def}\sin\theta_{def}}{\sin\theta_{inf}}\end{aligned}$$

$$\implies \cos\theta_{inf}\sin\theta_{inf} = 0.64\cos\theta_{def}\sin\theta_{def} \tag{7.9}$$

Using (7.7) and (7.9):

$$\alpha_{inf} = \frac{2\pi W \cos\theta_{inf}\sin\theta_{inf}}{0.64 n_v l_{def}} \tag{7.10}$$

$$\Rightarrow \alpha_{inf} - \alpha_{def} = \frac{2\pi W}{n_v l}\left(\frac{\cos\theta_{inf}\sin\theta_{inf}}{0.64} - \cos\theta_{def}\sin\theta_{def}\right) \tag{7.11}$$
$$= 0$$

It is clear that if there is no work associated with the change of length and diameter of the actuator, the actuator will not undergo any twist as derived in (7.11). To cause a twisting action an additional constraint on the motion is needed. This additional constraint can be introduced by including the work effects of the internal pressure in the main cylinder and the end constraints on the motion of the actuator.

Constant Main Cylinder Diameter

To simplify our analysis, we will consider the case where the cylinder is closed at both ends with a circular end made from a high tensile strength fabric. For a short actuator, the effect of the end constraint can be approximated by keeping the diameter D of actuator constant. To compute the rotary motion achieved at one end of the actuator, we will modify the analysis of the previous subsection by including this assumption.

If the diameter D is held constant, the circumference $C = \pi D$ is constant. Therefore, the helix angle of the small tubes θ can be directly computed from (7.5):

$$\theta = \cos^{-1}\frac{n_v l}{C} \tag{7.12}$$

Using (7.12), (7.7) can be modified to:

$$\alpha = \frac{2W}{D}\sqrt{1 - \left(\frac{n_v l}{C}\right)^2} \tag{7.13}$$

Using the above analysis, for a prototype with the following geometric parameters: $D = 50$ mm, $\theta_{def} = \pi/4$, $l_{def} = 5$ mm, $H_{def} = 100$ mm, the net rotation $(\alpha_{inf} - \alpha_{def})$ obtained is 57.46° as-

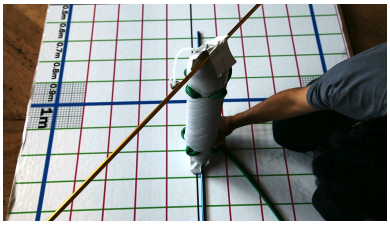

(a) Nominal configuration

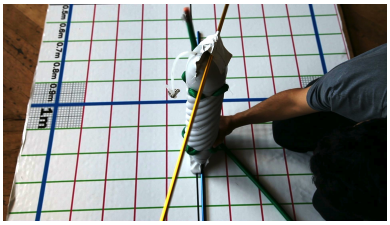

(b) Inflated configuration

Figure 7.10: Peano Skin type twist actuator

suming $\frac{l_{inf}}{l_{def}} = 0.64$.

7.3.4 Torque-Displacement Characteristics

The torque-displacement characteristics for the Rotary Peano actuators can be computed using the virtual work principle, while keeping the constant main cylinder diameter assumption from the previous subsection. From the virtual work principle:

$$\tau = P\frac{dV}{d\alpha} \tag{7.14}$$

where V is the volume of air in the small tubes and $\frac{dV}{d\alpha}$ is the derivative of the volume with respect to the end rotation of the actuator. The volume V is given by:

$$V = n_v A(l) W \tag{7.15}$$

where $A(l)$ is the cross-section of the small tube as a function of the width l of the smaller tube. As described in Fig. 7.6, the cross-section can also be parameterized using ϕ; we will use this

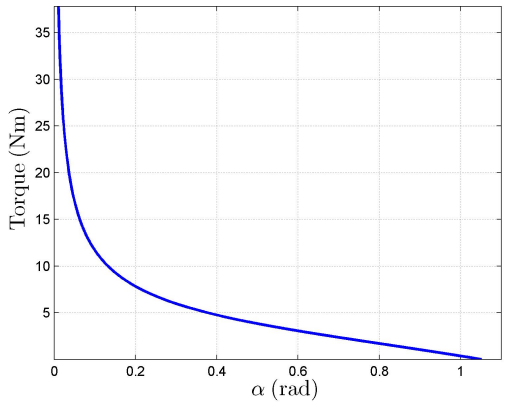

Figure 7.11: Example torque displacement characteristics for Peano Torque Actuators

parametrization instead to define the cross-sectional area of the small tube as shown below.

$$A(\phi) = \frac{l_{def}^2}{2\phi} - \frac{l_{def}^2 \sin(\phi)}{2\phi^2} \tag{7.16}$$

where the reparametrization between ϕ and l is given by:

$$l(\phi) = 2\frac{l_{def}}{\phi} \sin\left(\frac{\phi}{2}\right). \tag{7.17}$$

Using (7.16) and (7.17) we can derive $\frac{dA}{dl}$:

$$\frac{dA}{dl} = -\frac{l_{def} \cos\left(\frac{\phi}{2}\right)}{\phi} \tag{7.18}$$

Further using (7.13) we can write $\frac{dA}{d\alpha}$:

$$\begin{aligned} \frac{dV}{d\alpha} &= \frac{dV}{dl}\frac{dl}{d\alpha} \\ &= \frac{C^2 D\sqrt{1 + \frac{2ldef^2 n_v^2(-1+\cos(\phi))}{C^2\phi^2}}\cot\left(\frac{\phi}{2}\right)}{4n_v^2 W} \end{aligned} \tag{7.19}$$

Using (7.14) and (7.19), the torque-displacement characteristics of the rotary Peano actuators

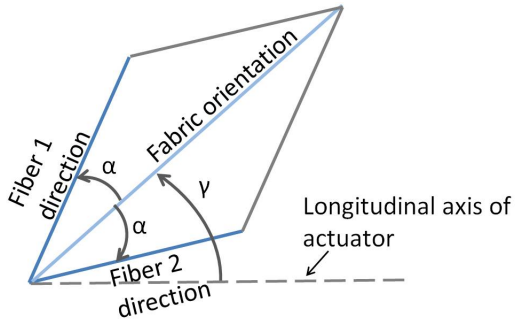

Figure 7.12: The geometry of a single block of the helical weave pattern fabric used for the torsion weave actuator

can be computed. Fig. 7.11 graphs the torque-displacement relationship at an inflation pressure of 10 psi; all other actuator parameters are the same as that stated in the previous subsection.

7.4 Torsion Weave Actuator

The Torsion Weave Actuator's motion is defined by the constraints due to the nearly inextensible fibers on its surface. The McKibben actuators use the same principle of constraining motion by using fibers aligned symmetrically about the direction of motion. By using an asymmetric arrangement of fibers on the surface it is possible to achieve rotary motion at the end.

7.4.1 Kinematics

The following constraint equations define the motion of the system:

$$l_1 \sin(\gamma+\alpha) = \pi D \tag{7.20}$$

$$l_2 \cos(\gamma-\alpha) = l \tag{7.21}$$

$$l_2 \sin(\gamma-\alpha) = \frac{\phi D}{2} \tag{7.22}$$

Above γ is a constant, $\gamma = \gamma_0$. l_1 and l_2 are the length of the two fibers along the actuator surface that make up the weave, $\gamma + \alpha$ and $\gamma - \alpha$ are the orientations of the two fibers with respect to the longitudinal axis of the actuator. Using (7.20) - (7.22) the derivative of the volume V of the actuator w.r.t to the net rotation ϕ at the end can be derived:

$$V = \frac{\pi l D^2}{4} \tag{7.23}$$

Using (7.20), (7.21), the volume can be represented explicitly as a function of α.

$$V = \frac{l_1^2 l_2 \cos(\alpha - \gamma_0) \sin^2(\alpha + \gamma_0)}{4\pi} \tag{7.24}$$

Taking the derivative of (7.24) w.r.t α and using (7.20) and 7.22), the derivative of the volume V w.r.t. the end rotation ϕ can be found:

$$\begin{aligned} \frac{dV}{d\phi} &= \frac{dV}{d\alpha}\frac{d\alpha}{d\phi} \\ &= -\frac{l_1^3 (3\cos(2\alpha) + \cos(2\gamma_0)) \csc(2\gamma_0) \sin^3(\alpha + \gamma_0)}{16\pi^2} \end{aligned} \tag{7.25}$$

7.4.2 Static Torque-Displacement Characteristics

The torque-displacement relation for the actuator can be computed using the virtual work principle and the volume-displacement derivative in (7.25):

$$\tau = P\frac{dV}{d\phi} \tag{7.26}$$

The torque displacement characteristics for the actuator prototyped by us (see Fig. 7.14) can be generated by substituting numerical values for l_1, l_2 and γ_0 into (7.26). Fig. 7.13 graphs the torque-displacement variation at an actuator pressure of $P = 25$ psi. For the above geometric parameters

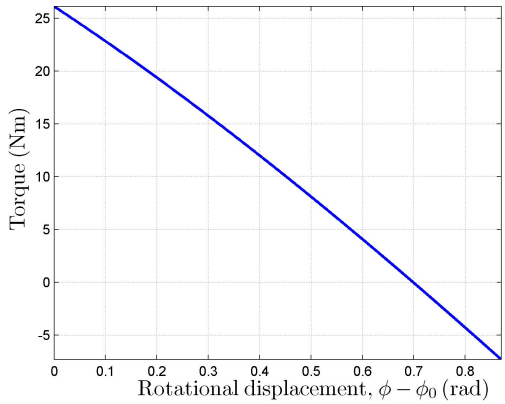

Figure 7.13: Example torque displacement characteristics for the torsion weave actuator

and operating pressure, the maximum rotational motion obtained was 40°. The maximum obtainable torque corresponding to zero displacement is 25 N-m. Clearly, geometric parameters and maximum operating pressure can be modified to change these characteristics.

7.5 Discussion

An issue we have ignored in this chapter is the structural role of the actuator if it is to be used in a soft bodied robot. Clearly, if the actuators were connected between two rigid bodies, the actuators only need to supply motive force in the torsional direction while structural loads can be carried by the rigid component. However, for a soft bodied robot like an inflatable manipulator, the actuator and the load bearing structure (can be the same) need to work together to achieve the desired torsional motion. The load bearing structure needs to support loads in all directions except torsional loads and must provide little resistance to torsional motion. Therefore the load bearing structure needs to be stiff to axial and bending loads but compliant to torsional loads. The low structural stiffness in the torsional direction will allow the torsional actuator to efficiently produce torsional motion while minimizing energy expenditure to torsionally deform the load bearing structure. A long beam with a star shaped cross-section is one example of a load bearing structure which can

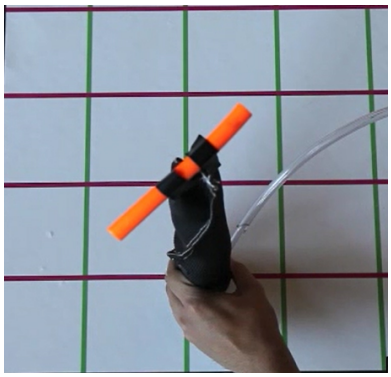

(a) Nominal configuration

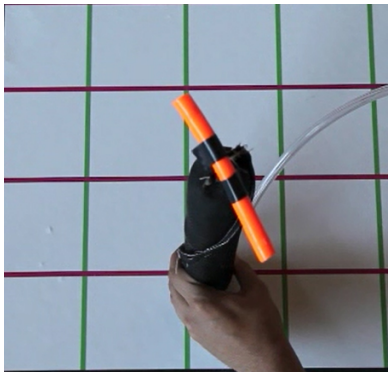

(b) Inflated configuration

Figure 7.14: Prototyped torsion weave actuator in its nominal and inflated configuration.

compliment a torsional actuator well.

7.6 Summary

In this chapter, we have discussed three different ways of realizing fluidic membrane or skin based rotary actuators. The primary motivation to develop these actuators was to provide such motion to an inflatable manipulator. The purpose of this chapter is not to recommend but explore the design space of such actuators and understand the underlying principles that govern their motion. However, our initial evaluation suggests certain advantages and disadvantages to each.

From our experimentation, it was observed that shape actuators can provide the most range of motion but they suffer from a non-deterministic or highly complex motion models. This is because

of the presence of wrinkling on the actuator structure in intermediate states. The shape actuators are the easiest to implement in order to obtain bi-directional torque using a single actuator structure. However, in their current development stage, these actuators are best suited to applications requiring binary actuation, i.e, motion between two states only. From our experiments and theoretical models, the Peano rotary actuators provide relatively less range of motion compared to the other two actuator types. These actuators can provide higher speeds because of the low volume of air needed to generate motion. The Peano actuators also have a deterministic model of operation for all states that span its range of motion. The McKibben actuators have a highly deterministic model for their motion because of the relatively simple length constraints that cause its motion; no fabric shear is involved unlike the other two actuator types. Bi-directional torque is somewhat complicated to achieve with a single McKibben type actuator, however this can be done with two actuators in an antagonistic configuration connected end to end.

Chapter 8

Accuracy

This chapter discusses modeling, control and sensing for inflatable robots. The goal is to develop models that help in the design of inflatable structures for robots and to utilize models for improving accuracy in position control tasks. Models that allow prediction of strength and deformations of inflatable manipulators are identified and experimentally verified. An inverse kinematics scheme is developed that utilizes the deformation model. Simulations showing the effectiveness of the scheme are presented. We also address the problem of joint angle estimation for inflatable manipulators which is necessary for accurate positioning of the manipulator.

8.1 Design and Modeling of Inflatable Structures

Fig. 8.1 provides one framework within which we can think of modeling inflatable robots. For the purpose of designing inflatable robot structures for desired payload and strength properties a strength model is needed. The strength model can be used to predict strength properties of the structure given the 3D inflated geometrical model of the structure and vice versa. There has been some prior work in developing models to predict the strength of inflatable volumes [21, 68], we will build on these existing models and explain them in Sec. 8.1.1.

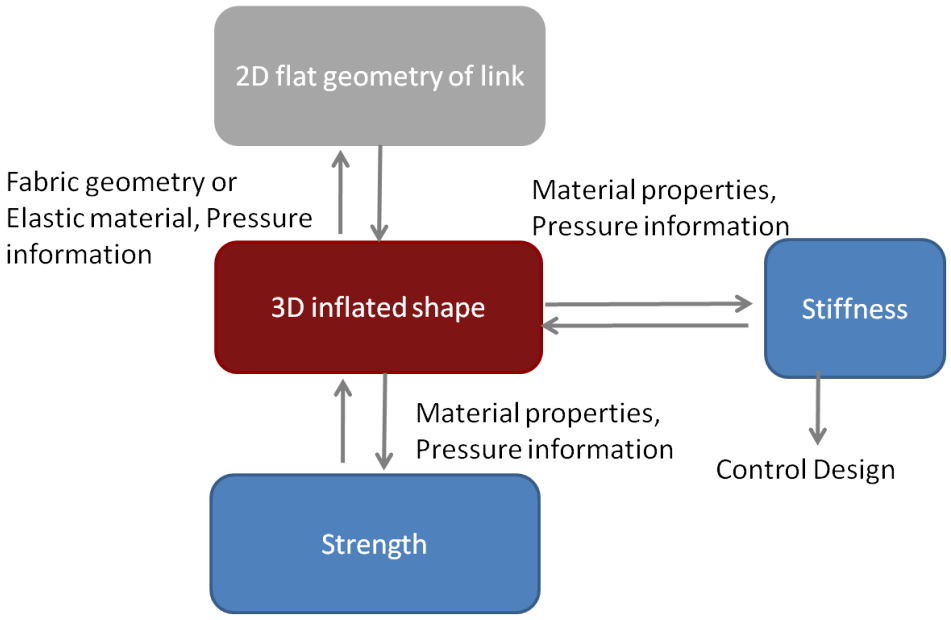

Figure 8.1: Rolling Flexure Joint.

The other important modeling component in the design framework described in Fig. 8.1 is the stiffness model which uses the 3D inflated geometry, material characteristics and pressure information of the structure to provide information regarding the deformations in the systems. Such a stiffness model can then be utilized during control design to compensate for deformations within a system during positioning tasks. We will present one such algorithm in Sec. 8.2.

One key difference between traditional rigid structures and inflatable structures is the realization of 3D volumes. Traditional rigid structures are most often manufactured using a 3D subtractive process (3D additive processes have also matured in recent years) allowing physical realization of virtually any shape from a solid block of metal. Inflatable structures on the other hand involve generating a 3D volume from 2D planar surfaces. The third component in the framework in Fig. 8.1 deals with this mapping. Fortunately, it is fairly trivial to construct simple zero-gaussian curvature surfaces such as cylinders and cones. We will mostly use only such simple geometric surfaces to build the AIRArm prototype. We shall not discuss here the problem of generating general 3D shapes from flat panels.

8.1.1 Structural Model for Strength and Stiffness

The simplest approach to modeling the strength and deformation characteristics of an inflatable link in the absence of wrinkling is to use conventional beam theory as applied to thin walled beams. Comer and Levy [21] developed one such model for an inflated beam using conventional beam theory. Main et al. [68] used a similar formulation where the deflection characteristics of the beam, before wrinkling occurs, is given by the Euler Bernoulli beam theory for small deflections. Maine et al. [68] also provide a model to predict deflections post wrinkling.

The load at which an inflatable structure begins to wrinkle is determined by the internal pressure in the structure and its geometry. This is the minimum load at which compressive stress occurs anywhere on the surface of the structure. It must be noted, that the maximum load that can be carried by the structure is greater than the wrinkling load. This is because failure of the link occurs when wrinkling occurs in a large percentage of the cross-section at a certain location on the beam, not at a single location alone [21, 68]. Theoretically, the maximum load is twice the wrinkling load for any given pressure of the inflatable beam [68]. The wrinkling load is important information nonetheless, because once wrinkling first occurs in the structure, the deflection characteristics deviate from the nominal behavior. Prescribed loads for inflatable structures are therefore usually based on the wrinkling loads.

In a cantilever load condition, the wrinkling load can be found by equating the bending stress due to the external load to the longitudinal stress due to the internal pressure. For a straight cylindrical inflatable link of radius r and length l, the relationship between internal pressure P_{in} and wrinkling load F_w is given by:

$$F_w = \frac{\pi r^3}{2l} P_{in} \tag{8.1}$$

While there is general agreement in inflatable structure literature regarding the wrinkling load and failure load, there multiple deflection models that may be reasonably accurate for predicting deflections before wrinkling occurs. As mentioned earlier, one approach is to utilize only the

geometry and material properties of the structure and apply these to regular beam theory. Clearly this approach disregards any influence of the pressure on the stiffness of the structure. Fichter [29] proposed a more general formulation of the deflection problem for inflatable beams using a minimum potential energy approach. They derived a model consistent with that of Timoshenko beam theory with additional terms relating to the axial force caused by the internal pressure of the beam. More recently, Le and Wielgosz [64] developed a similar model that also accounts for the initial stresses and strains in the structure due to pressure. The models developed indicate a stiffening effect of pressure on the structure. The overall effect of pressure is the following: 1) For thin inflatable beams ($l/r > 20$), the pressure has the effect of increasing the apparent Young's modulus of the material 2) For thick beams, in addition to increasing the apparent Young's modulus of the material, the apparent shear modulus (G) of the material is increased as well. Although the stiffening effect is present, as is noted by the authors, these effects may be unnoticeable at low pressures (10psi, for an 8cm dia. polyethylene beam) [68]. Deflection experiments with our prototype low pressure inflatable beams agree with this observation. We will briefly discuss our experiments below.

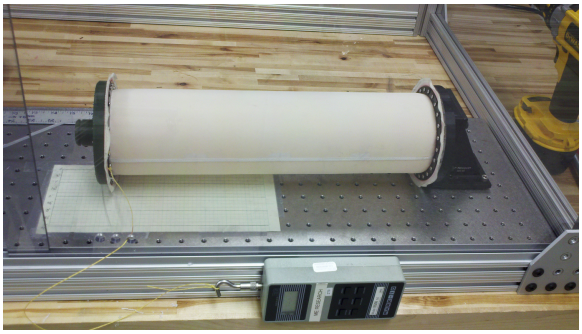

Figure 8.2: Experimental setup for deflection tests for an inflatable link.

To identify and verify a suitable model for the inflatable link, deflection experiments for the fabricated prototype links were conducted. The setup for the deflection experiments is shown in Fig. 8.2. The data from these experiments were compared with predictions from a two models: a) The Euler-Bernoulli (EB) beam model, and b)Pressure corrected Euler-Bernoulli beam model

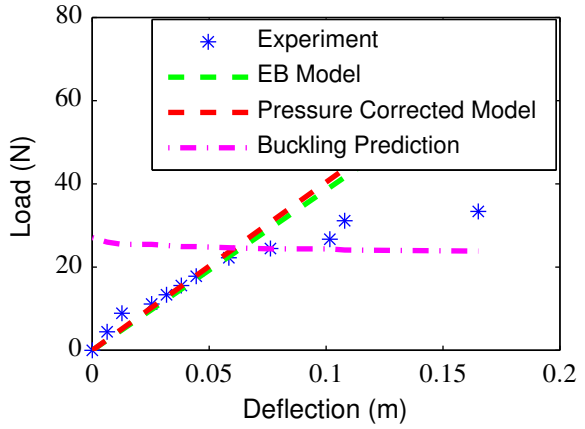

(a)

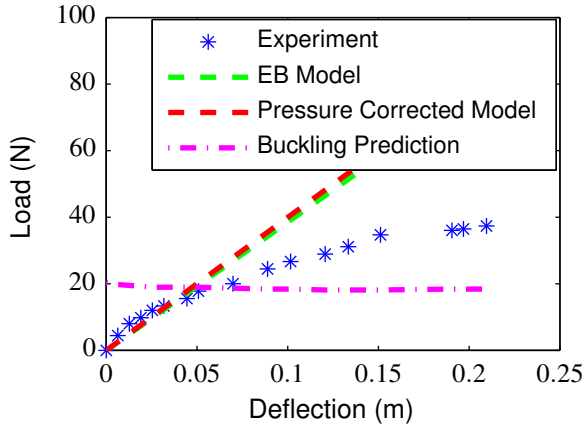

(b)

Figure 8.3: Model prediction and experimental data for load-deflection curve and buckling for 10 psi (top) and 5 psi (bottom) internal pressure.

according to [64]. During each experiment the load at which wrinkling was visually observed was also noted. Fig. 8.3 shows the load deflection experimental data collected for internal pressures of 10 psi (top) and 5 psi (bottom) and the loads at wrinkling is observed. Also shown are load deflection predictions using two models: a) the Euler-Bernoulli (EB) beam model and b) the Pressure corrected Euler-Bernoulli beam model. Fig. 8.3 also shows the load at which wrinkling is predicted for the experiment according to (8.1).

For the sake of completeness the equations used to compute the load-deflection line for the EB and Pressure corrected EB model are presented below:

The Euler-Bernoulli model:

$$F = ky \tag{8.2}$$

$$k = \frac{3E\pi t r^3}{l^3} \tag{8.3}$$

The Pressure correct Euler-Bernoulli model:

$$F = ky \tag{8.4}$$

$$k = \frac{3\bar{E}\pi t r^3}{l^3} \tag{8.5}$$

$$\bar{E} = E + \frac{P}{\pi r^2} \tag{8.6}$$

From Fig. 8.3, it is clear that prior to the wrinkling load prediction according to (8.1), the predictions from both the EB and Pressure corrected EB models match the load deflection experimental observations reasonably well. For loads that are larger than the predicted wrinkling load, these models are expected to be invalid and the experimental observations match this expectation. An abrupt reduction in stiffness of the link is observed for loads larger than the predicted wrinkling load, as is expected when wrinkling actually occurs on the structure. This shows that in our experiments the predicted wrinkling load is a good indicator of the true load at which wrinkling occurs.

Note on Pressure Effects on Deflection

We will attempt to provide a brief intuitive description of the effect of internal pressure on link stiffness here. For the sake of this analysis we will assume the inflatable link is cantilevered and that it admits Euler-Bernoulli beam mechanics. To understand the effect of internal pressure on link stiffness, we can think of an inflatable link as a solid beam with an end load F_L and an axial load F_P due to the internal pressure, like the beam in Fig. 8.4.

We will first derive the governing differential equation for the angular deflection θ of the beam cross-section along its length s with respect to the coordinate frame X,Y at the tip. Using large deflection Euler-Bernoulli beam mechanics, this can be derived as:

$$EI\frac{d\theta}{ds} = -F_p\int_0^s \sin\theta(\sigma)d\sigma + F_L\int_0^s \cos\theta(\sigma)d\sigma \tag{8.7}$$

Differentiating (8.7) w.r.t s again and rearranging, we get:

$$EI\frac{d\theta}{ds^2} + F_p\sin\theta = F_L\cos\theta \tag{8.8}$$

If θ is small, (8.8) reduces to:

$$EI\frac{d\theta}{ds^2} + F_p\theta = F_L\theta \tag{8.9}$$

The integral solution of (8.9) with the appropriate boundary conditions of the problem is:

$$\theta = \frac{F_L}{F_p} - \frac{F_L}{F_p}cos\left(\sqrt{\frac{F_p}{EI}}\right) \tag{8.10}$$

A series expansion of the cosine term in (8.10) reveals the role of F_p in the angular deflection of the beam:

$$\theta = \frac{F_L}{2EI}s^2 - \frac{F_L}{24E^2I^2}s^4F_p + O(F_p^2) \tag{8.11}$$

From (8.11), it can be seen that the effect of the axial force F_p due to internal pressure is to reduce the angular deflection at all locations along the length of the beam. In other words the internal pressure can be seen to have a stiffening effect on the inflatable link. In a first order analysis, the magnitude of the stiffening effect is directly proportional to the internal pressure P because $F_p = P\pi r^2$ (r is the radius of the link at the end) and is inversely proportional to the square of the Young's modulus E and the square of the second moment of area of cross-section of the link I.

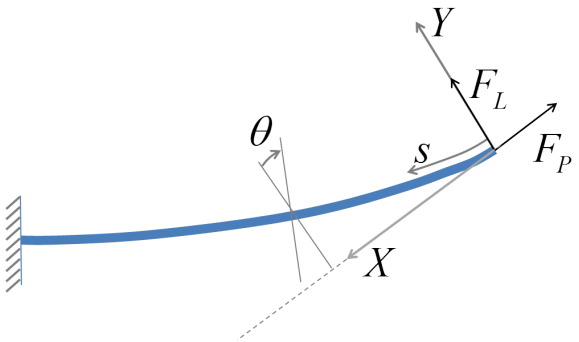

Figure 8.4: Inflatable link with end load and axial load due to internal pressure.

8.2 Inflatable Manipulator Control

We shall now discuss how the modeling effort directed toward inflatable links can be utilized to control the an inflatable manipulator like the AIRarm, consisting of many such inflatable links. We shall address here the issue of inverse kinematics (IK) in the presence of a gravitational field.

8.2.1 Soft Inverse Kinematics using assumed kinematics

An inflatable manipulator consisting of inflatable links has a flexible structure and can therefore deform when it is loaded due to its own weight and the weight of the payload it is carrying. Therefore the payload will not be correctly positioned if the joint angles of the arm are computed using inverse kinematics for a rigid manipulator. The deformations in the structure need be accounted for. This is a consequence of using materials with a lower Young's modulus than conventional materials such as aluminum, steel or carbon fiber. This issue is also present in traditional manipulators with flexible links and has been studied in the past. Methods have been developed that include deformation models of the system in the kinematic model [104, 103]. We will adapt these methods for application to an inflatable manipulator and provide a brief description of the methodology next.

We need to develop an inverse kinematics (IK) map that relates some location on the manipulator (typically the tip) to desired joint angles in presence of deformations due to gravity. We will

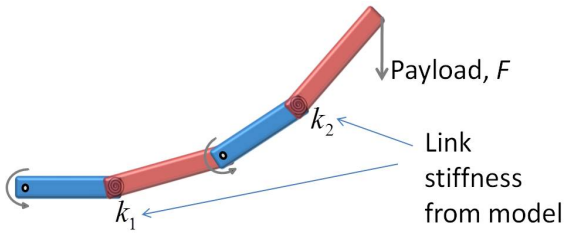

Figure 8.5: Finite segment model of a two link planar inflatable manipulator. Each flexible link is split into two segments that are connected by a torsional spring that has stiffness derived from the stiffness model.

call this map I:

$$I : \mathbf{x}_s \mapsto \mathbf{q}_s \tag{8.12}$$

In (8.12), $\mathbf{x}_s$ is the position of the manipulator tip and $\mathbf{q}_s$ is the configuration of the arm model that includes joint angles and deformations. The subscript s is used to indicate that the map is only defined for steady state.

To develop this map for the AIRarm, we will make use of a finite segment model shown in Fig. 8.5. The model consists of two rigid joint and two flexible joints with a torsion spring whose stiffness is obtaining using the stiffness model described in Sec 8.1.1. The tip stiffness of the links, defined by (8.6), can be mapped to the torsional stiffness k_1, k_2 of Fig. 8.5 by:

$$k_\tau = \frac{kl^2}{4} \tag{8.13}$$

where, k_τ is the equivalent torsional stiffness of the finite segment model that results in a tip stiffness k and l is the length of the link. The torsional spring of the finite segment model divides each link into two segments of equal length.

The configuration $\mathbf{q}_s = (\theta, \delta)^T$ for this model is defined by the pair of joint angles $\theta = (\theta_1, \theta_2)^T$ and the angular deformations of the torsion springs $\delta = (\delta_1, \delta_2)$. The forward map F that relates the configuration variables to the tip position can be easily derived for this model. We will not

repeat it here for the sake of brevity:

$$\begin{aligned} \mathbf{x}_s &= F(\mathbf{q}_s) \\ &= F(\theta, \delta) \end{aligned} \tag{8.14}$$

Furthermore, a stiffness matrix $\mathbf{K} = diag(k_1, k_2)$ relates the torques and deformations at the torsion spring. Using this stiffness matrix $\mathbf{K}$, we can rewrite (8.14) as:

$$\mathbf{x}_s = F\left(\theta, \mathbf{K}^{-1} G_\delta(\theta)\right) \tag{8.15}$$

$$= \bar{F}(\theta) \tag{8.16}$$

In (8.15), $G_\delta(\theta)$ is the gravitational load on the torsion springs a given θ. If $\bar{F}^{-1}$ can be analytically derived then the soft inverse kinematics can be explicitly derived as:

$$\begin{pmatrix} \theta \\ \delta_s \end{pmatrix} = \begin{pmatrix} \bar{F}^{-1}(\mathbf{x}_s) \\ \mathbf{K}^{-1}\left(G_\delta\left(\bar{F}^{-1}(\mathbf{x}_s)\right)\right) \end{pmatrix} \tag{8.17}$$

In general, $\bar{F}^{-1}$ cannot be analytically derived we can proceed by computing the differential $d\mathbf{x}$ from 8.15:

$$\begin{aligned} d\mathbf{x} &= J_\theta d\theta + J_\delta K^{-1} \frac{\partial G_\delta}{\partial \theta} d\theta \\ &= \left(J_\theta + J_\delta K^{-1} \frac{\partial G_\delta}{\partial \theta}\right) d\theta \end{aligned} \tag{8.18}$$

In (8.18), J is the partial derivative of $F(\theta, \delta_s)$ with respect to the subscript. The expression within the parentheses in (8.18) resembles a regular Jacobian found in the differential kinematic equations for rigid systems with some additional terms that account for variation of tip position due to gravity loads on the torsion springs.

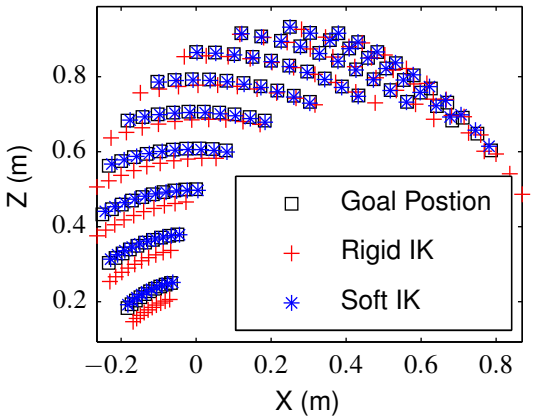

Figure 8.6: Inverse kinematics (IK) based on soft kinematics that accounts for deformations due to external loads results in more accurate tip positioning as compared to rigid inverse kinematics.

The algorithm presented above can be evaluated using a more complex model of the arm, such as an FEM model. We used the SPACAR matlab toolbox [57] for our evaluation, which allows dynamic simulations using nonlinear finite element method. Fig. 8.6 shows evaluation of the scheme using a finite element model of the inflatable manipulator using flexible links with structural properties as identified by the link modeling procedure. The tip positions resulting from IK computations using a rigid model are also shown. The IK computations using the approximate gravity corrected Jacobian derived above result in tip positions relatively close to the goal position as compared to those from the rigid body IK.

8.2.2 Soft Inverse Kinematics for Jointless Soft Robots

In the derivation above we assumed that the motion of the structure is a composition of rigid body displacements (θ) and elastic deformations (δ). As a result, we could predict and command rigid body displacements (joint angles) that would lead to a desired position of the end effector. While this is a reasonable assumption for inflatable manipulators, it is nonetheless an approximation because in reality no rigid joints exist on the structure. Such kinematic assumptions may also be entirely infeasible for general inflatable or soft bodied robots such as that shown in Fig. 8.7. We

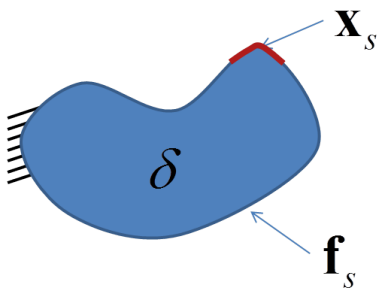

Figure 8.7: A soft robot with only elastic deformations and no joints.

will briefly describe a variation of the method described earlier to position an end effector in the absence of these kinematic assumptions.

$$C : \mathbf{x}_s \mapsto \mathbf{f}_s \tag{8.19}$$

For a soft bodied robot that has an elastic structure such as that depicted in Fig. 8.7, it is useful to command forces instead of joint angles (since no joints exist). We are then interested in the problem of finding the static forces $\mathbf{f}_s$ needed to position some point (the end effector or tip) on the soft robot to a desired location $\mathbf{x}_s$, i.e, the map (8.19). As in the previous section, we will use the forward map $S : \mathbf{f} \mapsto \mathbf{x}_s$ to compute the inverse map using a Jacobian transpose method. To derive this map we will use the elastic map $E : \mathbf{q}_s \mapsto \mathbf{f}$ that relates the configuration of the structure to the actuation forces on it. For linear elastic problems, the elastic map and its inverse can be represented as:

$$\begin{aligned} \mathbf{f} &= K\delta \\ \delta &= K^{-1}\mathbf{f} \end{aligned} \tag{8.20}$$

Now, we define the forward deformation map that relates the deformations to the tip position:

$$\mathbf{x} = l(\delta) \tag{8.21}$$

Note that we can arrive at the identical derivation as in 8.2.1, by substituting the finite segment forward kinematic map in (8.21). Composing (8.21) and (8.20) we get the forward map S:

$$\mathbf{x} = l(\mathbf{K}^{-1} f) \tag{8.22}$$

Using (8.22), we can compute the differential $d\mathbf{x}$:

$$d\mathbf{x} = \frac{\partial l(\delta)}{\delta} \frac{\partial \delta}{\mathbf{f}} d\mathbf{f} \tag{8.23}$$

$$= J_\delta K^{-1} d\mathbf{f} \tag{8.24}$$

Using (8.24), we can employ a Jacobian transpose method to compute the inverse map $I : \mathbf{x}_s \mapsto \mathbf{f}$. The usefulness of such a map lies in the fact that we can plan in the space of forces being exerted on the robot which is a lower dimensional space than the full configuration space is the elastic body.

8.3 Inflatable Joint Angle Estimation

In the above section on soft kinematics (8.2.1), we were able to achieve accurate positioning of a soft manipulator by factoring in the load dependent deformations in the system to compute the desired joint angles of the system. Clearly, it is necessary to be able to accurately control joint angles in the system in order to realize accurate positioning using the soft inverse kinematics scheme. For inflatable joints this is not a straightforward to achieve due to two reasons: (1) inflatable joint kinematic models are an approximation and (2) sensors for direct measurement of inflatable joint angles are not readily available. The issue of kinematic models can be addressed by improving joint design so that its motion more closely approximates the desired motion between links. In this section, we will address the issue of sensors for estimating inflatable joint angles.

8.3.1 Joint Angle Estimation using Pressure Sensors at the Joints

It is possible to derive a simple map between the motor shaft angle (θ_{2m}) and the inflatable joint angle θ_2 under the assumption that the tendon is taut, we shall refer to this map as the transmission map, $T : \theta_{2m} \mapsto \theta_2$. Since the tendons are pull only, i.e. compressive loads cannot be supported, loads that have a positive moment about joint 2 will cause deflection of link 2 based on the stiffness of the joint. This deflection is not resisted by the tendon causing it to slack. A joint angle estimation method that is not dependent on the tendon transmission kinematics is therefore useful.

It is observed that the pressure (P_J) in the joint varies with the joint angle θ_2. It is therefore possible to estimate the joint angle θ_2 by measuring the pressure P_J in the inflatable joint 2. We shall refer to this estimate as the pressure model joint angle, θ_2^P. A pressure sensor (Freescale MPXV5100GC6U) connected to the joint via a tube was utilized to measure the pressure P_J. Data shown in Fig. 8.8 was collected by driving the joint to various angles. A cubic polynomial was fit to the data, resulting in the model $\theta_2^P = z(P_J)$ for predicting the joint angle θ_2 using the pressure measurement P_J. From the experimental data, it was observed that a resolution of $\approx 5^\circ$ can be achieved for θ_2 estimated using pressure measurements.

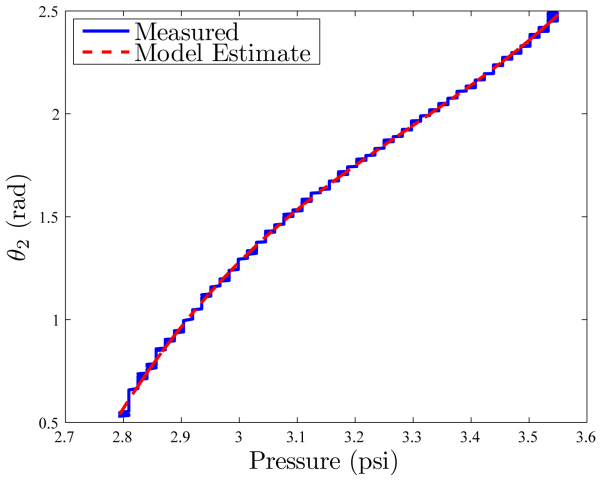

Figure 8.8: Joint pressure (P_J), joint angle (θ_2) data and joint angle prediction using fit model.

The identified model can be utilized in a contact detection scheme, we will describe the working

of such a scheme next.

Contact Detection

It is possible to detect contact with an external object when the contact location is on the second link of the manipulator. This is done by comparing the angle estimate from the transmission map (θ_2^T)and the pressure model (θ_2^P) to generate a boolean contact variable (α), given by:

$$\alpha = \begin{cases} 1, & \text{if } \left(\theta_2^T - \theta_2^P\right) > \varepsilon_{th} \\ 0, & \text{if } \left(\theta_2^T - \theta_2^P\right) \leq \varepsilon_{th} \end{cases} \tag{8.25}$$

where, $\alpha = 1$ indicates contact has occurred while $\alpha = 0$ indicates no contact, $\theta_2^T = T(\theta_{2m})$ and $\theta_2^P = z(P_J)$. Fig. 8.9 shows the evolution of the kinematic and pressure model joint angle estimate along with the generated contact variable for a particular trial. The detection scheme successfully infers contact (the time period when $\alpha = 1$) with an external agent. The threshold ε_{th} can be used to control the sensitivity of the detection scheme. Typically, its value is chosen to be close to the obtainable resolution for the joint angle using the pressure model.

8.3.2 Joint Angle Estimation using Inertial Measurement Units (IMUs)

Using pressure sensors is a feasible method for joint angle estimation, but the sensing is highly dependent on the geometry and inflation pressure of the joint. The only implication is that the joint angle to pressure mapping needs to calibrated each time the robot is pressurized. Another issue is the accuracy of the geometrical model that relates the tendon length to the joint angle which is used to develop the joint angle to pressure mapping. It is therefore highly desirable to have some direct measurement of joint angles that is independent of the robot model. In this section, we will describe the use of inertial measurement units (IMUs) placed on the inflatable manipulator structure to provide direct measurement of joint angles.

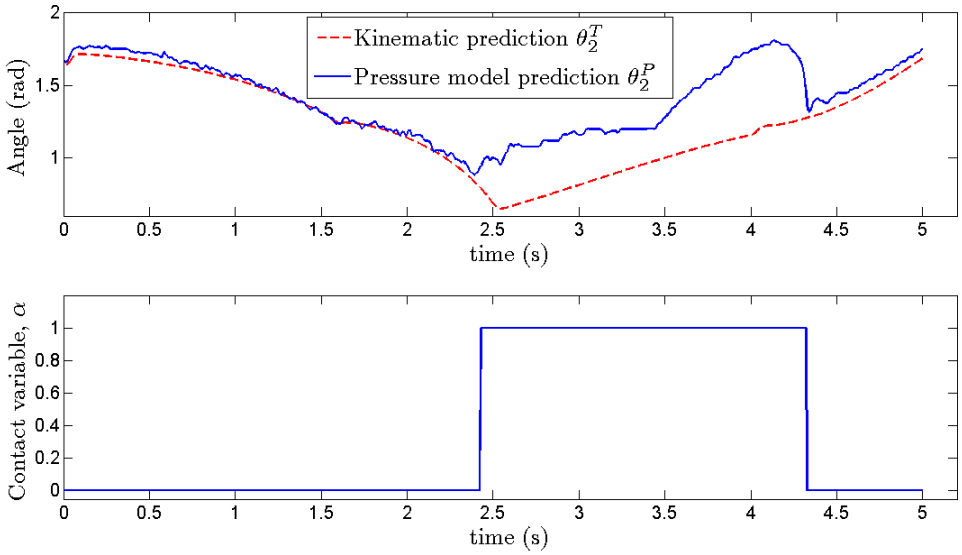

Figure 8.9: Kinematic and pressure model joint angle estimates are shown during a trial. When contact occurs, the discrepancy between the two increases causing the contact variable to become true.

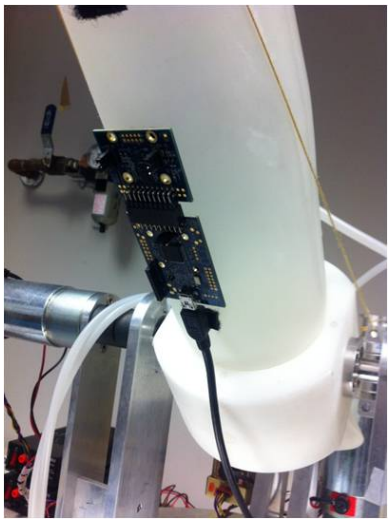

Figure 8.10: An IMU on the inflatable manipulator's structure.

Fig. 8.10 show an IMU (Invensense MPU-6050) attached to a link of the inflatable arm. The measurements from the IMU accelerometer and gyroscope are fused in an orientation estimator (based on the algorithm described in [67]) to provide an estimate of the joint angle. In Fig. the joint angle estimated by the IMU and the motor encoders are plotted. The estimate from the IMU

matches the motor encoder estimate well. The joint angle estimator uses data from the IMU which is sampled at 200Hz.

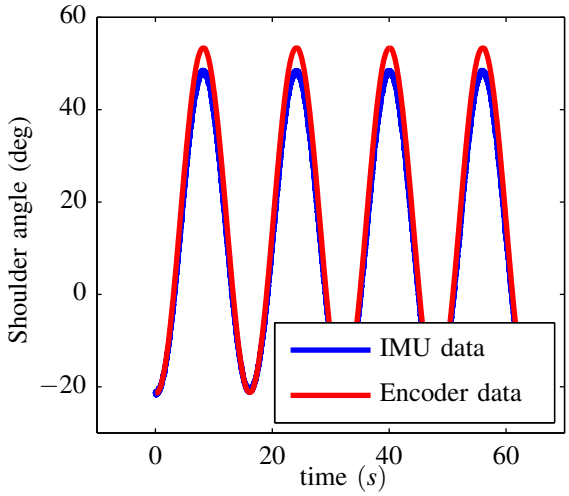

Figure 8.11: Inverse kinematics (IK) based on soft kinematics that accounts for deformations due to external loads results in more accurate tip positioning as compared to rigid inverse kinematics.

The joint angle estimate can be used to close the loop on the joint angle of the inflatable as shown in Fig 8.12. In Fig 8.12, θ^{imu} is the joint angle estimate from the attached to the inflatable arm, θ^{d} is the desired joint angle, K is a proportional controller that outputs a desired angular velocity $\dot{\theta}_d$. The desired angular velocity $\dot{\theta}_d$ is sent to the motor controllers. Fig. 8.13 shows one of the links of the inflatable arm being driven to different joint angles based on the joint angle estimates from the IMU using this control scheme.

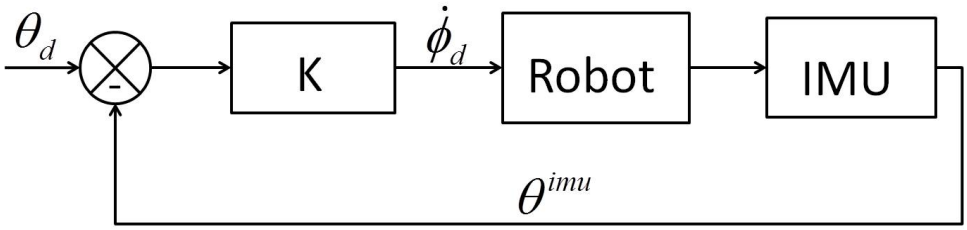

Figure 8.12: Control structure for IMU based joint angle servo

As described earlier, the second joint of the inflatable arm (the elbow) is actuated using tendons

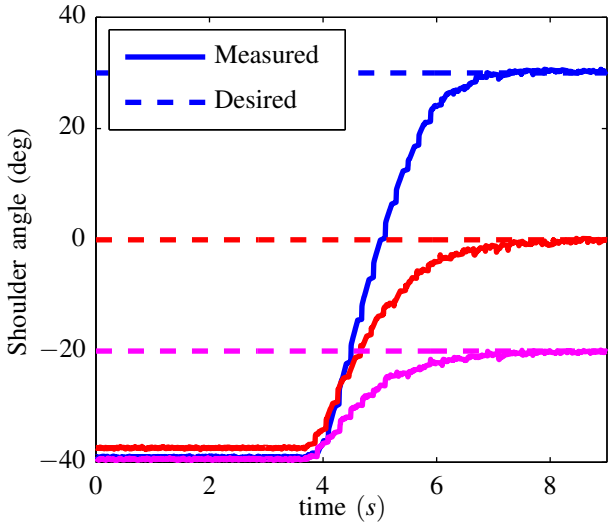

Figure 8.13: Control structure for IMU based joint angle servo

and can therefore be controlled using by prescribing desired motor angles that correspond to the desired joint angle of the elbow. The correspondence is based on a transmission model based on certain assumptions regarding the behavior of the inflatable joint. The transmission model may not be accurate because of the underlying assumption in the inflatable joint model. The IMU based joint servo can minimize the effect of such modeling uncertainties. We will use a Lyapunov like argument to show why this is true.

Let $g(\phi)$ be a known model that relates the joint angle θ to the motor angle ϕ. Let $\Delta(.)$ be the uncertainty in the model. We will assume it has functional dependency on ϕ.

$$\theta = g(\phi) + \Delta(\phi) \tag{8.26}$$

Clearly, if $\Delta(\phi) = 0$ everywhere in its domain then we can simply compute $\phi = g^{-1}(\theta^d)$ to achieve a desired joint angle θ^d of the robot by commanding a motor angle ϕ. Note that $\Delta(\phi)$ may have also have dependency on other external parameters such as payload carried by the arm, joint pressure, etc. Also we assume below $\Delta(.)$ does is not explicitly dependent on time. Differentiating the

known model $g(.)$:

$$\dot{\theta} = \frac{\partial g(\phi)}{\partial \phi}\dot{\phi} + \frac{\partial \Delta(\phi)}{\partial \phi}\dot{\phi} \tag{8.27}$$

Based on the control scheme in Fig. 8.12, we can substitute $\dot{\phi}$

$$\dot{\theta} = \left(\frac{\partial g(\phi)}{\partial \phi} + \frac{\partial \Delta(\phi)}{\partial \phi}\right) k\left(\theta^d - \theta\right) \tag{8.28}$$

Defining the error function $e = \theta^d - \theta$ and $\dot{e} = \dot{\theta}$, we can rewrite the above as:

$$\dot{e} = \left(\frac{\partial g(\phi)}{\partial \phi} + \frac{\partial \Delta(\phi)}{\partial \phi}\right) ke \tag{8.29}$$

Using the Lyapunov function $V(e) = \frac{1}{2}e^2$, we can write the condition for convergence of error e to 0:

$$\begin{aligned} & \dot{V} && < 0 \\ \implies & e\dot{e} && < 0 \\ \implies & \left(g' + \Delta'\right) ke^2 && < 0 \end{aligned} \tag{8.30}$$

Above, we have abbreviated the partial derivatives of g and Δ for compactness. A reasonable assumption is that $|g'| > |\Delta'|$, which means the known model correctly predicts the sign of the velocity map. Under this assumption, using 8.30 convergence can be guaranteed if $\operatorname{sgn} k = \operatorname{sgn} g'$.

8.3.3 Discussion on Alternate Sensors for Joint Angle estimation

Since joint angle sensing using IMUs may suffer from drift, noise and other calibration issues, other sensing methods which allow direct measurement of joints angles might be useful. Strain sensors that can measure the stretch across the inflatable joint are one possible alternative. Clearly the strains that we need to measure will be large. Commercially available sensors do not meet this

requirement. Sensors that can be integrated on soft robots have been the topic of recent research, with a number of *soft* sensors that can be used to measure strain and pressure being reported [88, 62]. Based on this work, a similar prototype sensor was developed for the CMU inflatable arm and is shown in Fig 8.14.

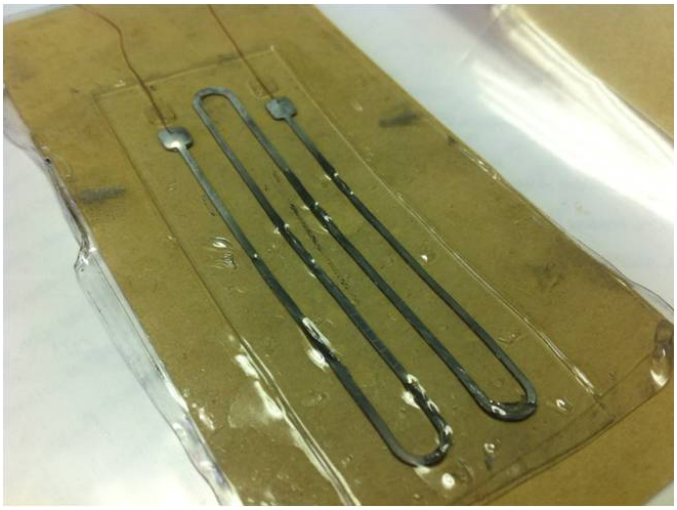

Figure 8.14: Soft strain sensor

The soft sensor in Fig. 8.14 is capable of measuring strain of up to 300%. It consists of three layers of VHB®tape with a channel that is filled with liquid conductive Eutectic Gallium Indium (eGaIn). The fabrication process is depicted in Fig 8.15. As the sensor is stretched the geometry of the channels filled with liquid conductive Eutectic Gallium Indium (eGaIn) changes causing the resistance to increase.

Sensors such as the one soft strain sensor described above have the potential to be integrated on to the surface of inflatable structure for providing a whole range sensor information such as internal pressure, contact force, surface strains, etc.

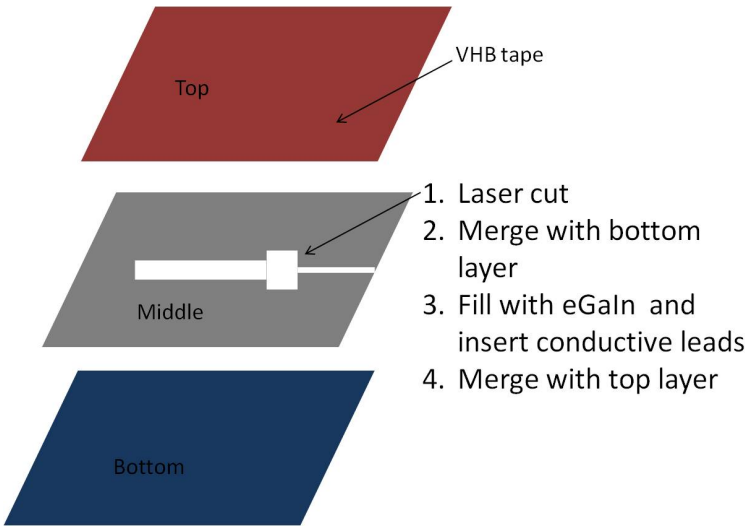

Figure 8.15: Fabrication process of soft strain sensor

8.4 Vibrations and Bandwidth

Since the CMU inflatable arm has an inherently low stiffness, significant vibrations can be expected from such a system. Clearly, different materials with either higher stiffness or damping can be used to reduce these vibrations. The PnueArm and AIRarm in Chapter 4, are two example inflatable systems where higher stiffness materials lead to less significant oscillations in the structure.

Vibrations in the CMU inflatable arm are observable visually (see video here add video link here). Using IMUs placed on the inflatable arm it is possible to measure these vibrations using acceleration data. Fig. 8.16 shows acceleration data for an IMU placed at the tip of the arm.

The power spectrum density of the signal in Fig. 8.16 is shown in Fig. 8.17. From this power spectrum density, a peak at around 2Hz can be identified which corresponds to the fundamental frequency of the system. This fundamental frequency closely matches the fundamental frequency identified from simulation, (see Fig. 8.18 which is based on the stiffness model described in Sec. 8.1.1. This fundamental frequency at around 2 Hz limits the control bandwidth for any tip position or force controller using non-collocated sensors and actuation.

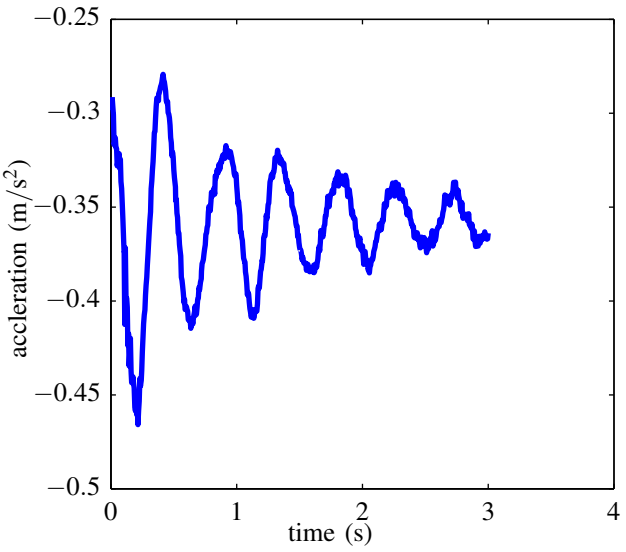

Figure 8.16: Acceleration at the tip of the CMU inflatable arm measured using the IMU accelerometer. The vibrations are excited by a step input in the angle ($theta_1$) of link 1.

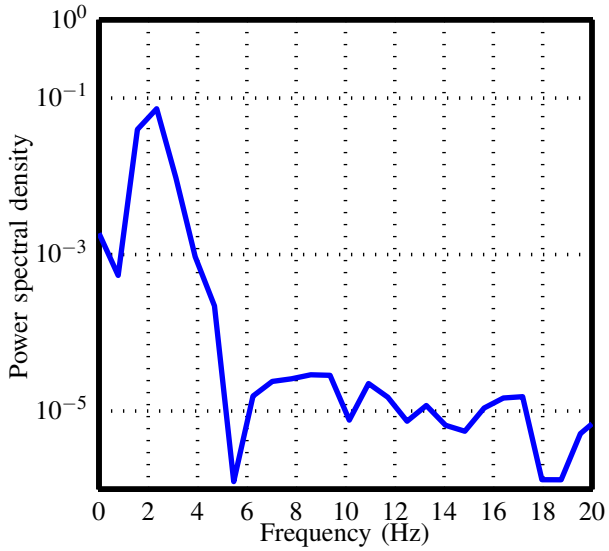

Figure 8.17: Power spectrum density of the tip acceleration. A peak can be observed at approximately 2 Hz

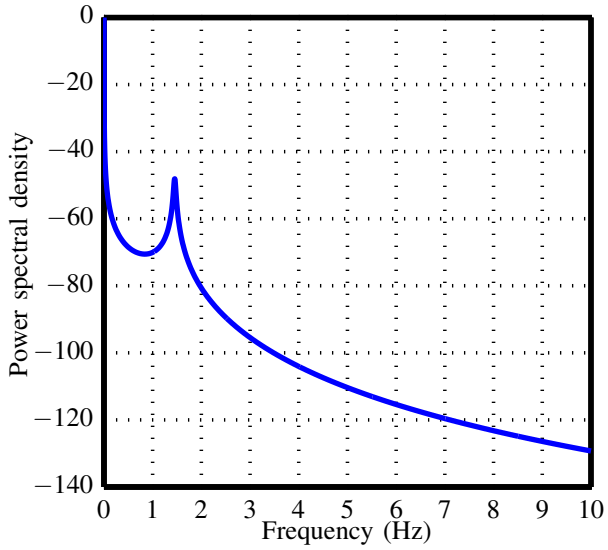

Figure 8.18: Power spectrum density of the tip vibrations from simulated data. A peak can be observed at approximately 1.5 Hz

8.4.1 Reducing Vibrations

Many techniques can be used to minimize vibrations in inflatable robots. We will list a few techniques here:

Increasing Structural Stiffness and Damping

Using materials that have higher stiffness or elasticity modulus can increase the stiffness of the structure. The PneuArm and AIRarm use a fabric shell that has a much higher stiffness and as a results leads to reduced vibrations. Materials with greater damping factors can also be employed to reduce vibrations. Other techniques that increase stiffness such as adding high stiffness elements such as kevlar strings at key load bearing areas of the structure. Some increase in stiffness is also possible by increasing the internal pressure in the inflatable structure.

To reduce the amplitude of vibrations in the CMU inflatable arm, additional stiffness was added at the first link in the form of a kevlar string reinforcement between the base and the link, as seen in Fig. 8.19. Fig. 8.20 shows the reduction in amplitude of acceleration at the tip of the arm when

the kevlar reinforcement is added in response to a step input in the desired angle at joint 1 (θ_1).

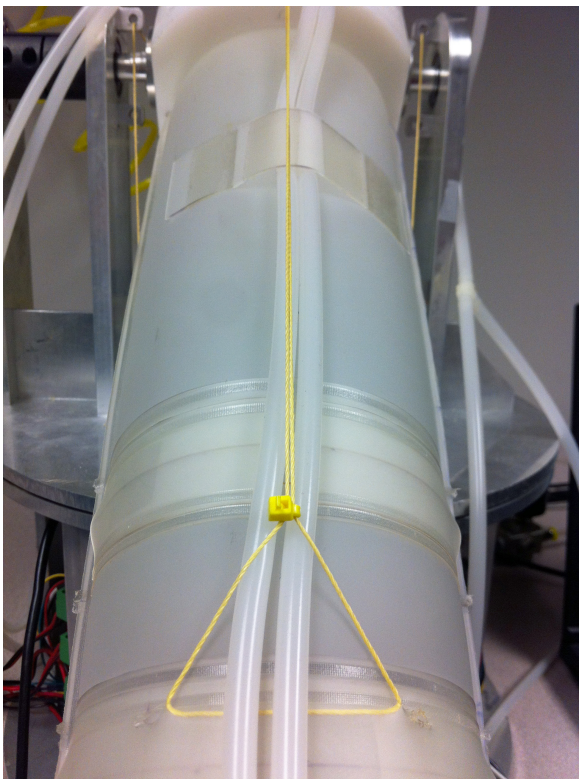

Figure 8.19: Kevlar string reinforcement between the base and the top side of link 1. The kevlar reinforcement provides additional support to the link increasing its overall stiffness.

Feedforward Control Techniques

If the structural stiffness is limited by safety or other factors (such as size limitations) a number of open loop control techniques exist to decrease vibrations. This has been studied in the past for flexible link robots and other systems that exhibit residual vibrations ([110, 27, 106, 120] and many others) . A relatively simply idea is to utilize reference trajectories that minimize jerk. Limiting jerk in trajectories reduces the transient vibrations in flexible systems ([66, 63]).

Fig. 8.21 shows the response of two control schemes used for positioning a simulated CMU inflatable arm. The first control scheme uses a joint level PD control along with gravity compensation to drive the joints to desired angles. The second control scheme uses minimum jerk reference

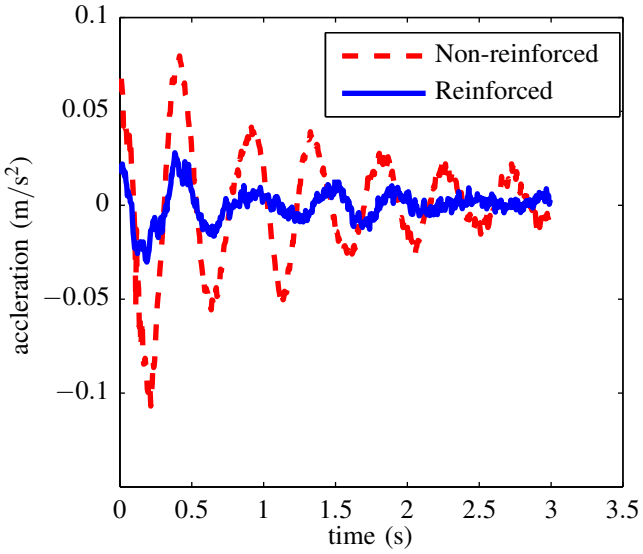

Figure 8.20: Comparison of the acceleration at the tip of the CMU inflatable arm with and without the kevlar reinforcement. A reduction in the amplitude of the vibrations can be observed. The vibrations are excited by a step input in the angle ($theta_1$) of link 1.

trajectories that are fourth order polynomial trajectories between the start and end (desired) joint angles. The reference trajectories are sent to the joint level controller which again uses PD control with gravity compensation. The reduction of vibrations at the tip of the arm can be clearly observed.

Another well known technique is command input shaping ([106]) where the input command is shaped such that the energy corresponding to the under-damped poles of the system is reduced. Input shaping requires knowledge of the poles of the system.

Feedback Control Techniques

Vibration suppression using feedback control based on deformations in the system has been employed in the past for flexible link manipulators. One approach has been to use optical or vision based systems to measure deformation at some point of interest in the system, typically the end effector ([82, 7]). Another approach has been to utilize IMUs, to sense accelerations and velocities due to deformations and to use these as feedback to reduce vibrations ([47, 65, 111]).

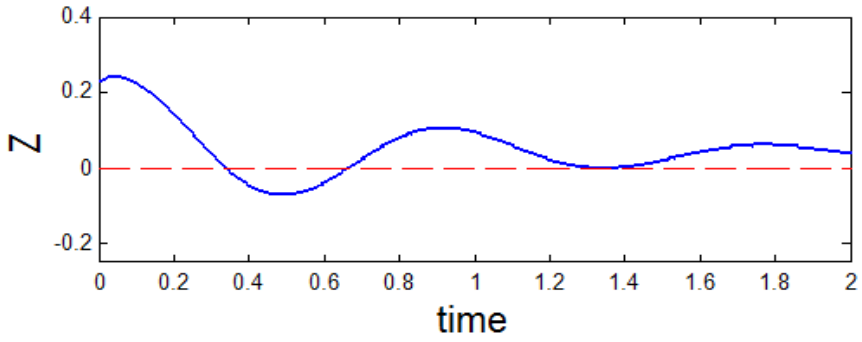

(a) Arm tip vertical position (in meters) when only PD control + gravity compensation is used to move between desired joint angles of the simulated inflatable arm

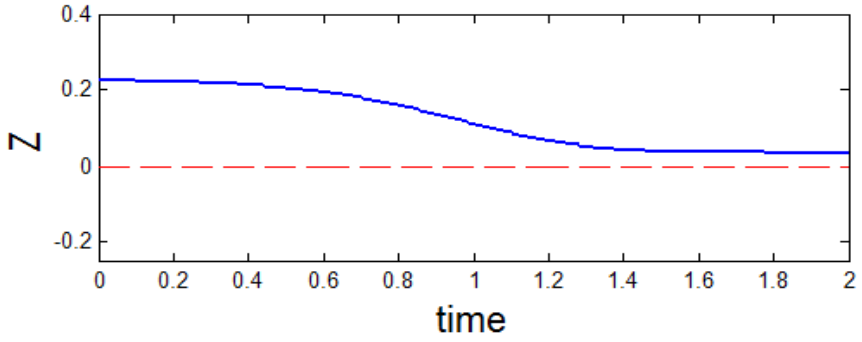

(b) Arm tip vertical position (in meters) when minimum jerk trajectories are used to move between desired joint angles of the simulated inflatable arm

Figure 8.21: Time histories of arm tip vertical position in meters, showing reduction in vibrations at the tip when minimum jerk trajectories are commanded for the joint angles. The time axis is in seconds.

The tip deformation rate was used in a feedback control scheme to reduce tip vibrations of the CMU inflatable arm, in simulation. In Fig. 8.22, the tip position using deformation rate feedback is plotted along with the tip position in the case where deformation rate feedback is not used. As expected, a reduction in tip vibrations can be observed in the case where deformation rate feedback is utilized.

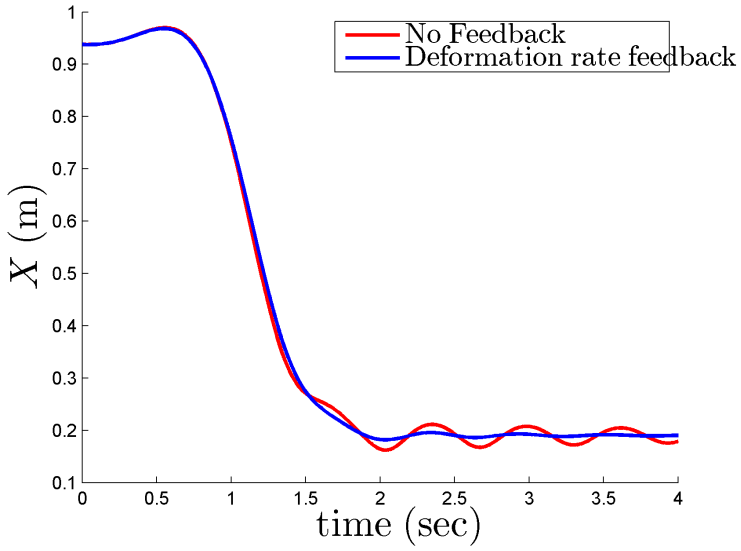

Figure 8.22: Simulation results showing comparison of tip vibrations with and without the use of deformation rate feedback in the joint controller. The deformation rate feedback reduces vibrations at the tip.

8.5 Discussion

In this chapter, we identified and utilized strength and stiffness models for inflatable links. These models can then be plugged into the soft inverse kinematics scheme for quasi-static positioning of inflatable manipulators like the AIRarm or CMU inflatable arm in its workspace. However, we ignored the role of deflections that occur across the joint. For accurate positioning, it is important to account for such deflections and therefore some effort needs to be devoted to incorporating joint deflections in the soft inverse kinematics scheme.

8.6 Summary

In this chapter, we developed models and state estimation methods to improve the accuracy of motion of inflatable manipulators. Models to predict the strength and stiffness of inflatable links were identified and these models were compared with experimental data. The strength model predicts the load at which wrinkling begins to occur on the structure. We use this load to specify payload capacity for the links and the manipulator. The stiffness model is used in to predict deflections of the links when loaded. While the internal pressure of the links, directly influences the payload capacity of the links, for the range of pressures used in our experiments, the effect on stiffness was not significant.

The Soft Inverse Kinematics scheme developed utilizes the stiffness model to allow quasi-static positioning of the inflatable manipulator in the presence of link deflections. The scheme was evaluated using a nonlinear finite element simulation an inflatable manipulator. The results indicate that the soft inverse kinematics scheme allows more accurate positioning of the arm tip when compared to rigid inverse kinematics. A generalization of the scheme was also developed to allow positioning of soft robots using actuator forces rather than joint angles. Tracking control for the arm which is not addressed in this chapter needs to be developed to allow the arm to follow trajectories that respect the deformations in the system.

Another issue which unique to soft and inflatable robots is that of estimating configuration variables like joint angles. In this chapter, we address joint angle sensing is addressed by the use of pressure sensors and inertial measurement units (IMUs). One key assumption is that the joint kinematics are assumed to be idealized. Further work is needed to either improve joint design to match the idealized joint kinematics or to use methods that do not rely on these assumptions.

Chapter 9

Physical Human Interaction

This chapter describes some of the capabilities developed for the CMU inflatable arm to handle tasks involving human interaction. We will describe a contact detection scheme based on joint pressure sensing using which the arm handles unintended contacts. Contact detection is also used to initiate a task where contact is intended, such as wiping. Experiments verifying the efficacy of the contact detection scheme are shown using the two interaction scenarios. We will also describe the inflatable arm carrying a feeding task. Result from a user study to evaluate user safety and comfort during the task are also presented.

9.1 Inflatable Joint Angle Estimation using Pressure Sensors

For the sake of clarity, we will restate the pressure sensor based joint angle estimation and contact detection scheme described in Sec. 8.3.1 in this section.

It is possible to derive a simple map between the motor shaft angle (θ_{2m}) and the inflatable joint angle θ_2 under the assumption that the tendon is taut, we shall refer to this map as the transmission map, $T : \theta_{2m} \mapsto \theta_2$. Since the tendons are pull only, i.e. compressive loads cannot be supported, loads that have a positive moment about joint 2 will cause deflection of link 2 based on the stiffness

of the joint. This deflection is not resisted by the tendon causing it to slack. A joint angle estimation method that is not dependent on the tendon transmission kinematics is therefore useful.

It is observed that the pressure (P_J) in the joint varies with the joint angle θ_2. It is therefore possible to estimate the joint angle θ_2 by measuring the pressure P_J in the inflatable joint 2. We shall refer to this estimate as the pressure model joint angle, θ_2^P. A pressure sensor (Freescale MPXV5100GC6U) connected to the joint via a tube was utilized to measure the pressure P_J. Data shown in Fig. 9.1 was collected by driving the joint to various angles. A cubic polynomial was fit to the data, resulting in the model $\theta_2^P = z(P_J)$ for predicting the joint angle θ_2 using the pressure measurement P_J. From the experimental data, it was observed that a resolution of $\approx 5^\circ$ can be achieved for θ_2 estimated using pressure measurements.

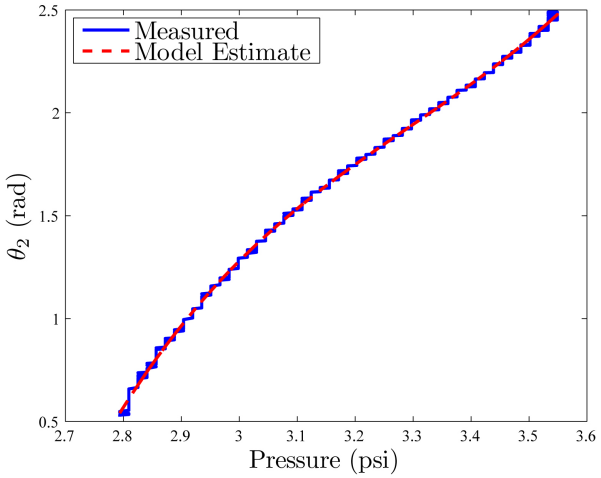

Figure 9.1: Joint pressure (P_J), joint angle (θ_2) data and joint angle prediction using fit model.

The identified model can be utilized in a contact detection scheme, we will describe the working of such a scheme next.

9.1.1 Contact Detection

It is possible to detect contact with an external object when the contact location is on the second link of the manipulator. This is done by comparing the angle estimate from the transmission map

$(\theta_2^T)$and the pressure model (θ_2^P) to generate a boolean contact variable (α), given by:

$$\alpha = \begin{cases} 1, & \text{if } \left(\theta_2^T - \theta_2^P\right) > \varepsilon_{th} \\ 0, & \text{if } \left(\theta_2^T - \theta_2^P\right) \leq \varepsilon_{th} \end{cases} \tag{9.1}$$

where, $\alpha = 1$ indicates contact has occurred while $\alpha = 0$ indicates no contact, $\theta_2^T = T(\theta_{2m})$ and $\theta_2^P = z(P_J)$. Fig. 9.2 shows the evolution of the kinematic and pressure model joint angle estimate along with the generated contact variable for a particular trial. The detection scheme successfully infers contact (the time period when $\alpha = 1$) with an external agent. The threshold ε_{th} can be used to control the sensitivity of the detection scheme. Typically, its value is chosen to be close to the obtainable resolution for the joint angle using the pressure model.

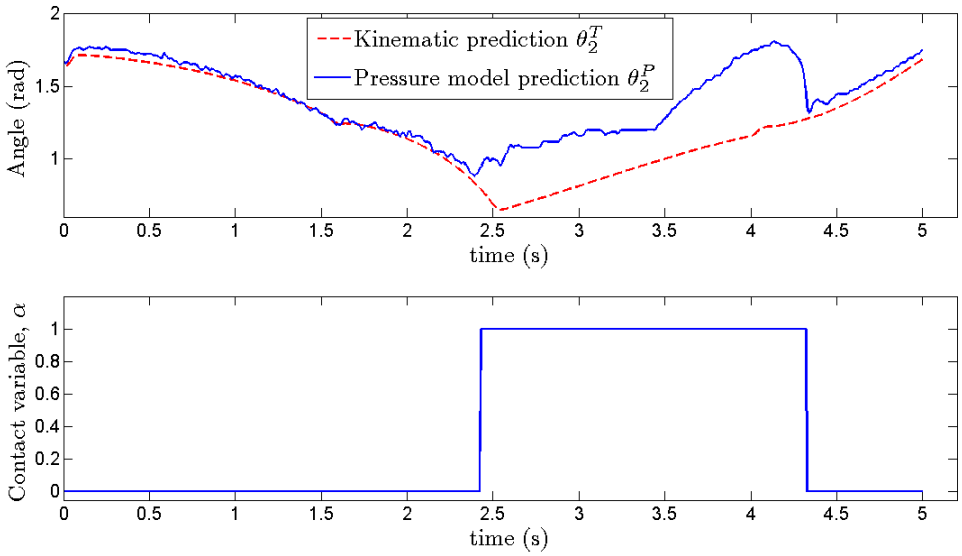

Figure 9.2: Kinematic and pressure model joint angle estimates are shown during a trial. When contact occurs, the discrepancy between the two increases causing the contact variable to become true.

9.2 Reaction Schemes

A reaction scheme coupled with the above contact detection scheme can be used to generate a variety of behavior for the inflatable manipulator. For instance, the reaction scheme can be used to minimize unintended interactions between the manipulator and an external agent by causing the manipulator to move away from the external agent once contact is detected. In other cases when interaction is intended, such as for sponging, the reaction scheme can also be used to execute a wiping motion upon detecting contact. We will next describe these two reactions schemes as implemented on the inflatable manipulator.

9.2.1 Unintended Interaction

As mentioned above, the reaction scheme may be used to minimize unintended interactions. Such a reaction scheme is useful, for instance, when the manipulator is following a trajectory and an unobserved external agent enters the path of the manipulator. For this reaction scheme, the contact detection scheme must initiate motion of the manipulator away from the external agent, when contact is detected. Fig. 9.3 shows the typical operation of the manipulator using such a reaction scheme.

Fig. 9.4 shows the contact forces occurring with the above reaction scheme implemented on the inflatable manipulator. A flat surface instrumented with a force/torque sensor was used to obstruct the path of the manipulator. Fig. 9.5a shows the motion of the manipulator under this reaction scheme when contact occurs with a human.

9.2.2 Intended Interaction - Sponging

For the simplified sponging task shown in Fig. 9.5b, the contact detection scheme is used to switch between two motion primitives: 1) Approach and 2) Wipe. The approach primitive essentially prescribes an end effector motion to seek contact with an external object. The wipe motion assumes

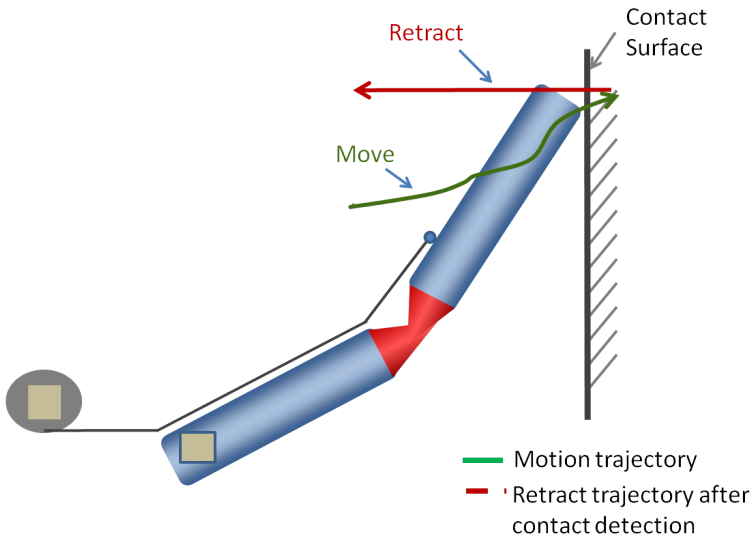

Figure 9.3: Schematic showing typical motion of the end effector for the reaction scheme to handle unintended interactions.

the contact surface is vertical and prescribes a vertical motion for the end effector. The robot is controlled to follow a desired path in its task space without explicitly taking contact force interaction into account. Contact forces are generated due to the torsional stiffness of joint 2 (inflatable joint) characterized in Sec. 4.1.5.

Fig. 9.6 shows the typical motion of the end effector when contact occurs. The desired path consists of 4 phases - Wipe, Lift, Move, Approach (Fig. 9.6). During the wipe phase, the desired trajectory lies within the contacting object. This leads to a contact force which is dependent on the joint stiffness described in Sec. 4.1.5. The desired duration of motion can be set for each phase. The resulting trajectory is mapped to desired actuator trajectories using the inverse kinematics map described in Sec. 4.1.4.

The desired geometric path and the measured path (computed using the kinematic model only and not accounting for joint deflections due to contact) is shown in Fig. 9.7a. For measuring the possible contact forces during the wipe phase, the sponging task was performed on a flat surface coupled to a force/torque sensor (ATI Mini85). The measured contact forces are shown in Fig. 9.7b. Fig. 9.8 shows snapshots of the inflatable manipulator sponging the upper body of a

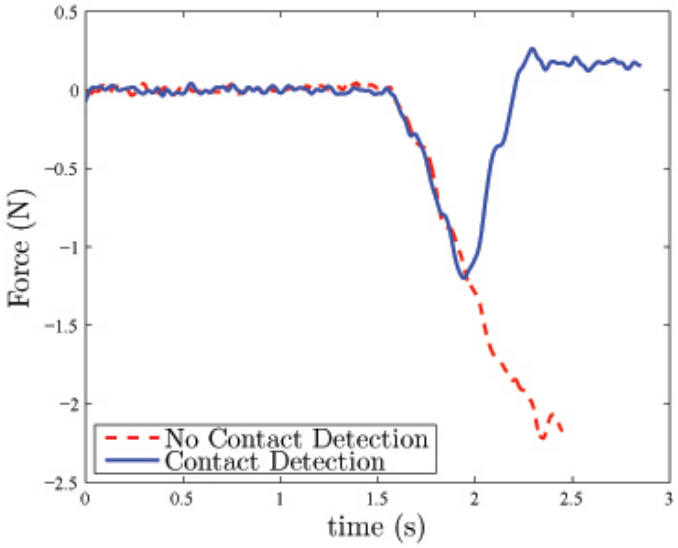

Figure 9.4: Contact forces with and without the contact detection scheme. When the contact detection scheme is not employed, the robot continues to follow its desired task space path. In the presence of contact detection, the manipulator stops following its desired task space path and instead retracts from the external agent.

mannequin. The manipulator is equipped with a towel at its end which is held in place using the inflatable torus. As the inflatable torus can rotate with some resistance about its joint (thermally welded seam), there is some additional compliance at the end of the arm.

9.2.3 Nudging

Using the estimated model of the relationship between joint pressure and joint angle in Sec. 8.3, it is possible to achieve compliant behavior at link 2. This allows for link 2 to be pushed or nudged to a new configuration by human interaction. As the link weight is very small, only a small force is needed to do this.

Such compliant behavior is achieved using a simple control scheme that drives the tendon motor to an angle θ_{2m}^{d} which corresponds to the current joint angle θ_2^P estimated using the pressure

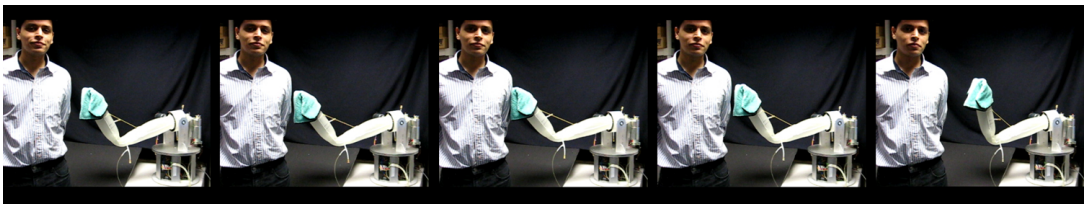

(a) Scheme to handle unintended interactions

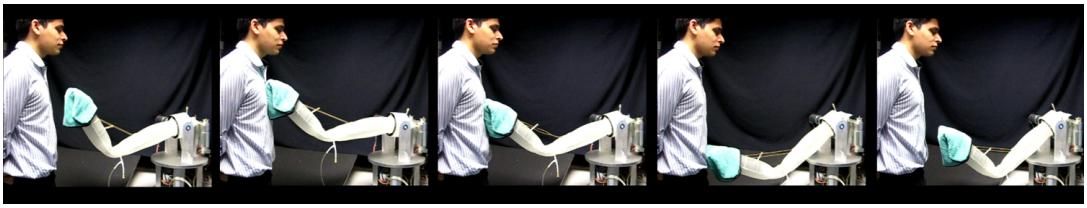

(b) Scheme to handle intended interaction during a simplified sponging task.

Figure 9.5: Motion of the manipulator under two reaction schemes for unintended and intended interactions

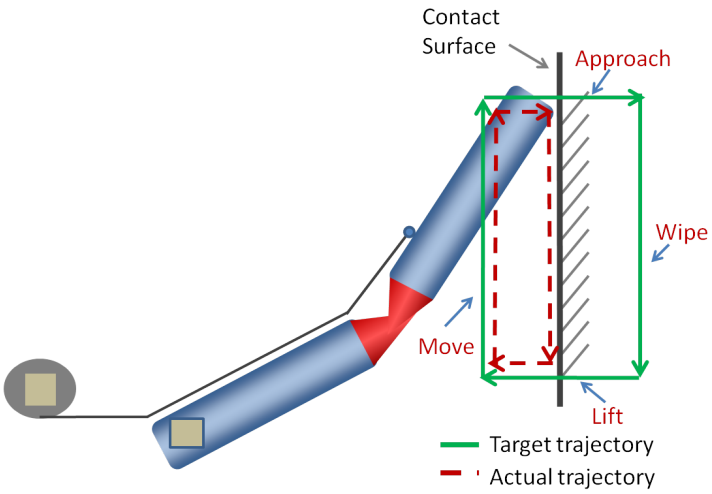

Figure 9.6: Schematic showing typical motion of the end effector for the sponging task.

measurement P_J:

$$u = k_p(\theta_{2m}^d - \theta_{2m}) \tag{9.2}$$

$$\theta_{2m}^d = T^{-1}(\theta_2^P) \tag{9.3}$$

$$\theta_2^P = z(P_J) \tag{9.4}$$

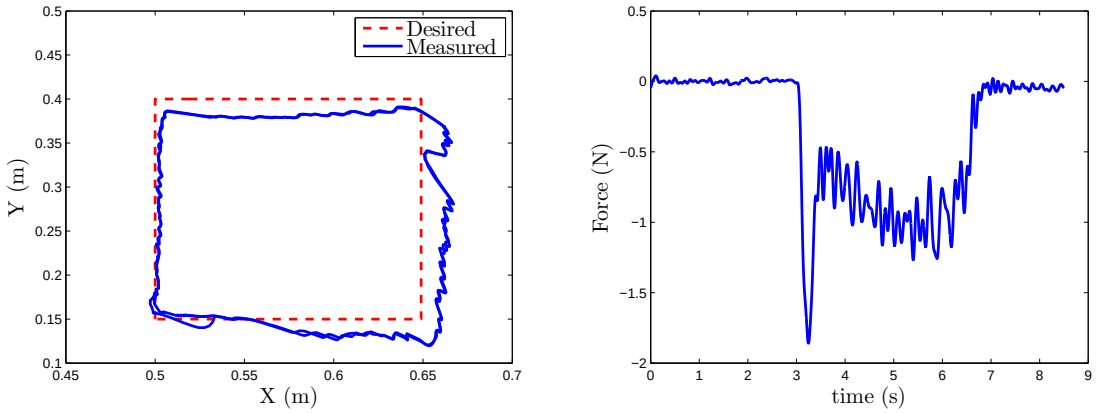

(a) Desired and measured geometric path of the end effector.

(b) Contact forces during sponging action measured on a flat panel coupled to a force/torque sensor.

Figure 9.7: End effector path and contact forces during execution of sponging action.

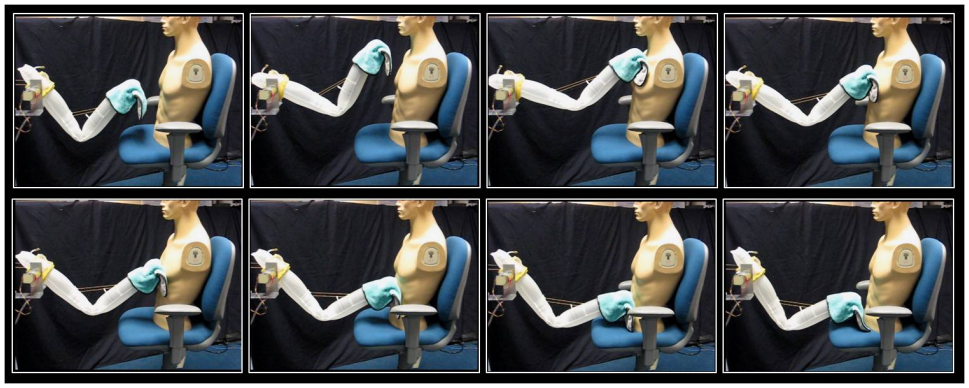

Figure 9.8: Snapshots of the inflatable manipulator performing the sponging action on a mannequin. The inflatable arm was equipped with a towel at its end, held in place using the inflatable torus.

In the above equations, u is the control which is the voltage on the motors, k_p is the proportional gain on the position error.

Fig. 9.9 shows the evolution of the joint angle estimate (θ_2^P) as predicted by the pressure model, and the joint angle estimate ($\theta_2^T = T(\theta_{2m})$) as predicted by the transmission model. As link 2 is pushed, the tendon slacks and there is a deviation between the estimate from the pressure model and the transmission model. This deviation is corrected using the controller in (9.2). The accompanying video shows the nudging behavior.

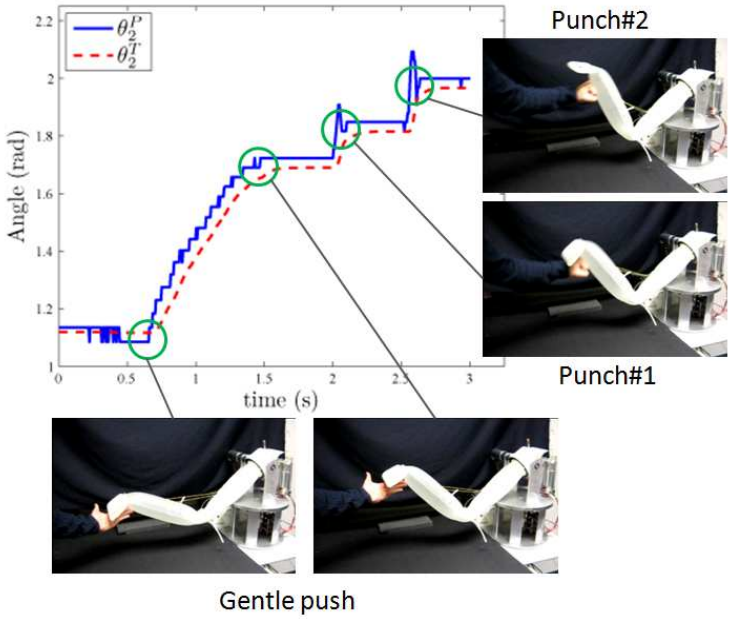

Figure 9.9: Joint angle estimates for inflatable joint 2 from joint pressure measurements and transmission kinematics while pushing link 2.

9.3 Feeding

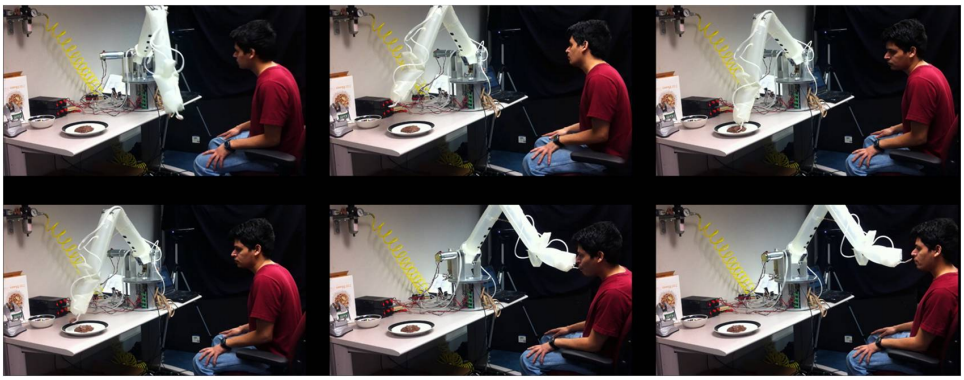

Figure 9.10: Contact force during the sponging task using the contact detection scheme.

Fig. 9.10 shows snapshots of the inflatable arm feeding a human. The feeding strategy employed is passive, in that food is brought close to the human's mouth and the human proceeds to eat the food. An active strategy would involve actions by the robot that assist in the transfer of food to the persons mouth from the end effector. Therefore to complete the task successfully the

human needs to have complete neck functionality and some functionality in the back.

The task is carried out using three subtasks. The user controls which subtask is carried out by the inflatable arm. The following subtasks make up the feeding task: (1) Pick up food (2) Bring food close to mouth and (3) Eat. To carry out the task the wrist of the inflatable arm is equipped with a plastic spoon as shown in Fig. 9.11.

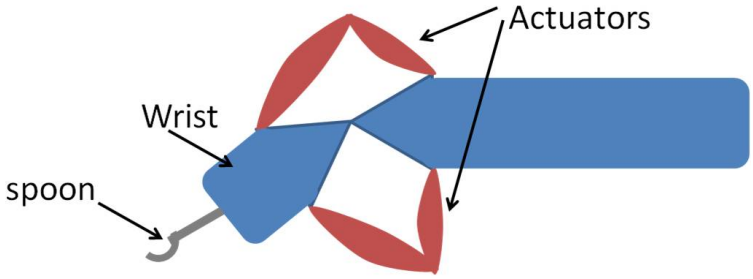

(a) Schematic showing spoon attached at the wrist interface

(b) Spoon affixed at end of the inflatable arm

Figure 9.11:

To pick up food, the inflatable arm is provided with information regarding the location of the plate and food. The arm uses a manually designed side scooping strategy to pick up food. During the pickup food task the location of the head of the user is constantly tracked by a Kinect sensor that is mounted away from the inflatable arm. The arm only believes the position of the head obtained by the Kinect sensor prior to its approach towards the head. This is to avoid noisy head

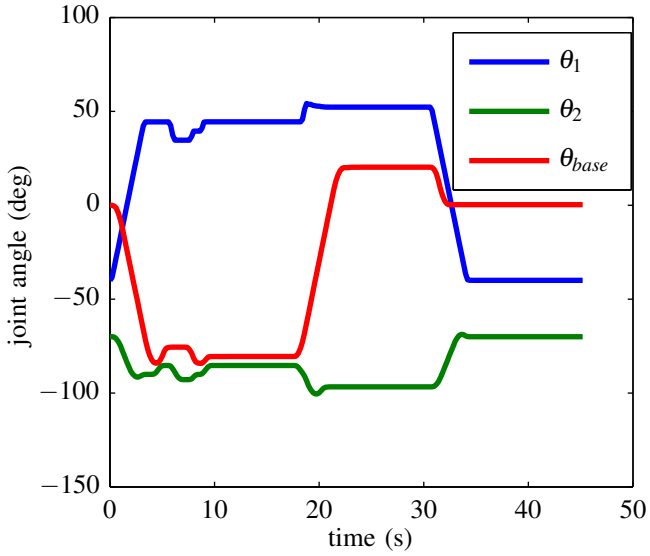

Figure 9.12: Time histories of joint angles for a single trial of the feeding task. In the data shown above, the task is completed at approximately 30 sec when the person finishes eating from the spoon and the robot moves to its default configuration.

tracking data due to occlusions caused by the inflatable arm as it approaches the head. When the arm is commanded to bring the food close to the mouth, it inputs the position of the head to an inverse kinematics (IK) scheme that uses the damped least squares (DLS) method [10]. The spoon moves towards the head based on the output of the IK scheme. Once the spoon reaches close to the mouth, the arm stays in position and the user can continue to eat the food. As the feeding strategy is passive the inflatable arm does not execute any behavior during the eating subtask. The user can repeat the procedure to eat more food or can stop at any time. Fig. 9.12 shows the joint angles of the arm during the feeding task.

9.3.1 User Studies

The above task was used to evaluate perceptions of safety, comfort level and usability of the inflatable arm via an IRB approved user study (see Sec. B for the protocol and related material used for the study).The study involved able bodied subjects above the age of 18. It should be noted that

one the biggest concern for conducting such a study is to ensure the safety of the subjects and with the inflatable arm this was easily achieved due to its inherent safety. Fig. 9.13 shows the subject responses on a variety of question regarding comfort, ease of eating and safety level during the task.

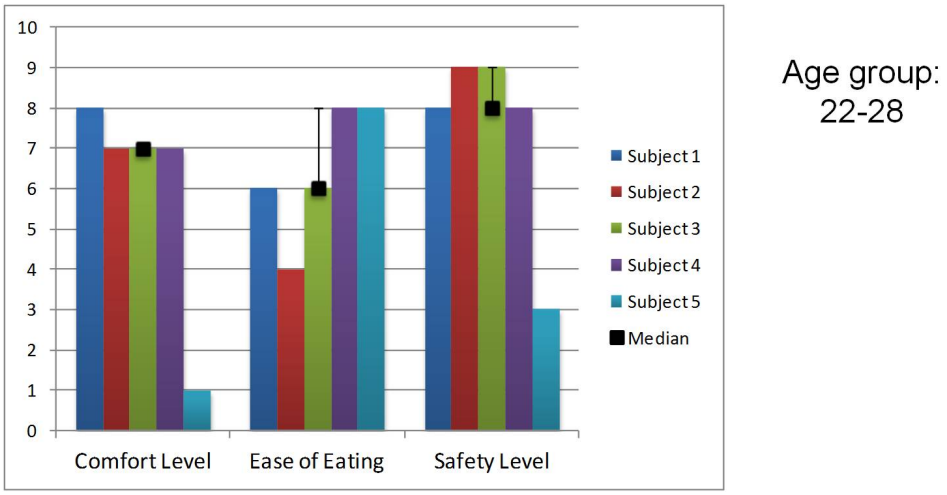

Figure 9.13: Results showing user evaluation of safety and comfort during the feeding task

9.4 Summary

In this chapter various cases of human interaction with the CMU inflatable arm are presented. A contact detection and reaction scheme for an inflatable manipulator, enabling safe physical human interaction, is described. The contact detection scheme uses pressure sensing at the inflatable joint to infer contact. Trials using the inflatable manipulator prototype indicate that the contact detection scheme can successfully detect contact. Using the reaction strategy for unintended interactions, the measured contact forces show that the manipulator is capable of very safe physical interaction with humans. For intended interactions, an alternate reaction strategy is also presented, wherein wiping action is performed once contact is detected.

Another human interaction context in which the CMU inflatable arm is used is feeding. An

IRB approved user study to asses various parameters concerning safety and ease of eating with the CMU inflatable arm was conducted. Only able bodied subjects were included in this study. The results indicate acceptable levels of comfort and safety as perceived by the users. In the future, developing active strategies for transferring food from the spoon to the subject mouth might be beneficial for target populations with severe disabilities. Some level of force/torque sensing will be needed at the wrist in order to successfully carry out an active feeding strategy.

Chapter 10

Conclusion

The thesis demonstrates the use of soft structured inflatable robots for safe physical human robot interaction. The primary motivation for this work is the need for intrinsically safe robots in assistive roles. Inflatable robots as demonstrated in this thesis satisfy requirements of intrinsic safety. This thesis addresses a number of key challenges towards developing inflatable robots for tasks involving close physical interaction with humans. We address questions regarding the design and manufacture, actuation methods, strength and accuracy of inflatable robots. Some of the contributions of this thesis are listed below:

10.1 Contributions

Understanding performance advantages of soft robots over rigid robots in human interaction tasks

Soft robots can have high inherent safety during impacts because of their highly compliant structure and low-weight. This allows soft robots to have relatively small safety constraints as compared to their rigid counterparts. At the same time, soft robots can be 'floppy', i.e, they can have large time constants leading to slower movements. Therefore, in the absence of safety constraints it

is absolutely true that a soft robot will be slower than a rigid robot. However safety constraints usually take the form of velocity constraints at multiple locations along the robot's structure where contact is expected. In theory, because these safety constraints are large for rigid robots they can make rigid robots slower than soft robots, in spite of the larger time constants in soft systems. This is demonstrated in Chapter 3. Our specific contribution lies in identifying that distributed compliance can contribute to performance improvements.

Framework for the design of soft robots

How does one proceed to design a soft robot? Are traditional static design requirements enough? Often soft systems can be engineered practically never fail for, e.g., a soft jelly fish like robot can be repeatedly smashed without incurring any damage at all. What should guide the design in such a case? Since the structural parameters of a soft robot affect the dynamic characteristics of a robot to a large extent these metric on these characteristic must be included in the design process. In Chapter 3 we developed a multi stage optimization framework that uses objective function scores from optimal control to iterate over the design variables.

Inverse kinematics for general elastic soft bodied robots

Kinematics of a soft robot are influenced by external factors such a loads and constraints due to contact, as well as its own weight. Therefore a purely geometric description of the kinematics for a soft robot is not possible. In Chapter 8 we developed methods to solve inverse kinematics problems for soft robots of various types by including a deformation model in the kinematics. One insight from these methods is that it is useful to prescribe forces to generate motions rather than prescribing configurations. While the configuration space of general soft robots may be infinite dimensional, often these robots live in a lower dimensional subspace because of the finite dimensional actuation and external forces that drive these robots.

Direct actuation in shape space using shape based actuators

Inflatable structures when inflated are defined by maximum volume surfaces. However, when deflated, the structure can take on a variety of shapes. We use this property of inflatable structure to develop shape based actuators in Chapters 4 and 7. These actuators are formed by combining differently shaped inflatable volumes along common geometric features. This allows the actuator to take the shape of whichever actuator is inflated. Therefore, unlike traditional actuators that cause some scalar parameter to vary when they are actuated shape based actuators allow us to actuate a structure directly in the shape space.

Expanding the design space for inflatable robots

This thesis contributes towards expanding the relatively unexplored design space for inflatable robots. In Chapters 4, 6 and 7 we have developed a catalogue of inflatable robot components such as links, wrists, joints, grasping devices, actuators, etc. that can be utilized for future iteration of inflatable robots.

Low cost robots that can be made like clothes and inflatable pool toys

Inflatable robots represent a key departure from traditional robots in terms of the manufacturing techniques that are used to manufacture them. Instead of subtractive or more recent additive 3D processes, these robots are manufactured using from 2D planar surfaces (fabric/plastic sheets) that are seamed together. This can be potentially transformative from a cost perspective because these robots can be manufactured like clothes with embedded sensing and actuation. Alternate seamless techniques can also be used such as that used in knitting. Further, if all seams in the structure are flat these robots can be manufactured using batch processing techniques similar to that found in the semiconductor industry.

10.2 Future Work

This section presents some possible directions for future research based on the work presented in this thesis. We also explore some future application for robotics based on inflatable structures.

Visual Servoing

Some of the drawbacks that exist, in terms of sensor hardware for accurate state estimation and motion of inflatable robots, can be overcome by the use of task space visual servoing. Visual servoing has been used in the past to improve accuracy for manipulators with flexible links and rigid manipulators ([85, 59]) and these techniques can be applied to inflatable robots. One distinction for inflatable robots is the lack of joint angle sensing which was addressed in Chapter 8.

State Estimation

In Chapter 8, we developed a method to estimate joint angles using Inertial Measurement Units (IMUs). The use of IMUs can be further extended to develop a state observer for the inflatable robots based on the acceleration and angular rate observations from the IMU. The state observer can be used be employed in a control scheme for force control, vibration suppression, load estimation etc. New sensor hardware similar to the stretch sensors described in Chapter 8 are also needed.

Vibration Suppression Techniques

Slow oscillations caused by external forces is often observed with inflatable robots. Methods to introduce damping into the structure either via design or control are needed. Developments in state estimation, joint design, actuation techniques and materials can aid progress in the area.

Variable Morphology Robots

Variable morphology robots refers to robots that can take on different physical forms based on the task. For instance, the robot can have different number of links based on the environment it is operating it to give it greater dexterity. Inflatable robots can be built to have such variable morphology. The variable buckling mechanism in Chapter 2 explores this idea by introducing variability in the location of the joint on the robot structure. Much more general variability is possible and can lead to interesting applications.

Appendix A

Synthesis of Safe Systems

A.1 Closed Loop Performance Based Synthesis

In Sec. 3.2, we detailed a synthesis procedure for soft robots to obey safety constraints and maximize some performance criteria. The performance criteria mentioned therein optimized some metric of the trajectory being followed by the system, in other words the metric was based on performance parameters in the time domain. This allowed for optimizing gross motions of the system for specific properties such as maneuver completion time, actuator effort along the trajectory etc. It is also possible to consider performance of the system from the perspective of its response to disturbances i.e its behavior with a feedback controller.

The purpose of the exercise in this chapter is to optimize the structure of the system such that the behavior of the system is acceptable across the frequency spectrum of disturbances. In some sense, we are attempting to improve the shape of the frequency response shown in the illustration in Fig. A.1.

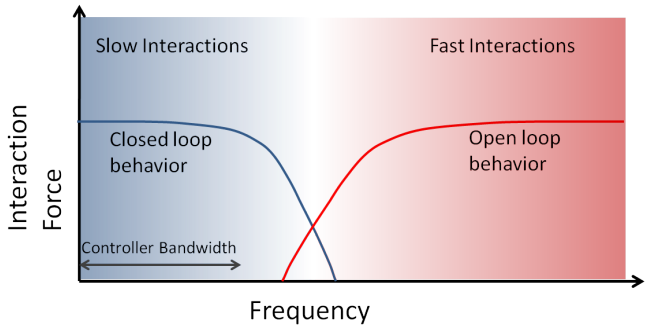

Figure A.1: Force interaction at various frequency. While introducing compliance in the structure of the robot improves open loop characteristics, it can adversely affect closed loop performance.

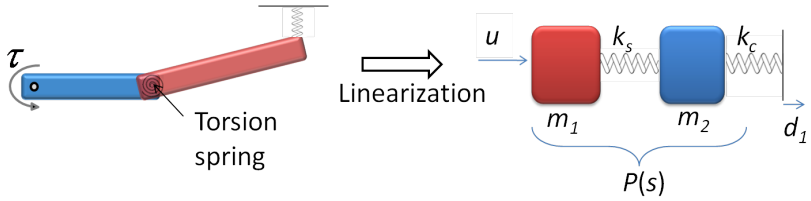

Figure A.2: Model of the system being utilized to illustrate the synthesis procedure.

A.1.1 System Model and Problem Formulation

We shall utilize the system shown in Fig. A.2 to explore the synthesis concept and procedure. The system consists of a 2 DoF planar arm with a compliant joint shown. Only the first link of the 2 DoF planar arm is actuated while the second link is connected to the first link via a torsion spring. The purpose of the torsion spring is to add passive compliance. Such a structure allows the possibility of limiting interaction forces at all frequencies, which is desired for safe pHRI. This system can be linearized by writing the equations of motion of the system in Cartesian space for the frame at the contact point. The linearized system can be represented by the two mass-spring system shown in Fig. A.2. The equations that relate the Cartesian masses to the inertias of the actual system are given by the following equations:

$$M_x = J^{-T} M_\theta J^{-1} \tag{A.1}$$

$$K_x = J^{-T} K_\theta J^{-1} \tag{A.2}$$

Here the subscript θ refers to the joint space parameters, while the subscript x refers to the Cartesian parameters of the system, J is the Jacobian from the angular velocities at the joints to the linear velocities at the contact end. In Fig. A.2, k_s is referred to as the structural stiffness and is derived using (A.2) and the stiffness of the torsion spring. The contact with the external object is represented by a linear contact spring connected to the second mass m2 in Fig A.2, while the other end of the contact spring connects to the external object. The system is actuated with a single actuator applying force u to the base mass m_1. The system is underactuated. The system equations are given by:

$$\begin{pmatrix} \dot{z}_1 \\ \dot{z}_2 \\ \dot{z}_3 \\ \dot{z}_4 \end{pmatrix} = \begin{pmatrix} 0 & 0 & 1 & 0 \\ 0 & 0 & 0 & 1 \\ -\frac{k_s}{m_1} & \frac{k_s}{m_1} & -\frac{b_s}{m_1}\frac{b_s}{m_1} & \\ -\frac{k_s}{m_2} & \frac{-k_s-k_c}{m_2} & \frac{b_s}{m_2} - \frac{b_s}{m_2} & \end{pmatrix} \begin{pmatrix} z_1 \\ z_2 \\ z_3 \\ z_4 \end{pmatrix} + \begin{pmatrix} 0 \\ 0 \\ \frac{1}{m_1} \\ 0 \end{pmatrix} u + \begin{pmatrix} 0 \\ 0 \\ 0 \\ \frac{k_c}{m_2} \end{pmatrix} d \tag{A.3}$$

$$\begin{pmatrix} y_1 \\ y_2 \\ y_3 \end{pmatrix} = \begin{pmatrix} 1 & 0 & 0 & 0 \\ 0 & 1 & 0 & 0 \\ 0 & k_c & 0 & 0 \end{pmatrix} \begin{pmatrix} z_1 \\ z_2 \\ z_3 \\ z_4 \end{pmatrix} + \begin{pmatrix} 0 \\ 0 \\ -k_c \end{pmatrix} d \tag{A.4}$$

Here $z_1 = x_1, z_2 = x_2, z_3 = \dot{x}_1, z_4 = \dot{x}_2$. The objective for the above system is to minimize the contact force F_c, exerted on the external surface, in the presence of disturbances d on the position

of the external surface. We shall attempt to do this by synthesizing a controller K_u for the actuator force u and the stiffness K_s for minimizing a given criteria. The measured outputs from the system are the position of the two masses and the contact force. The system described by (A.3) and A.4 can be used to form the interconnected system P, used to put the control synthesis problem in the standard form shown in Fig. A.3.

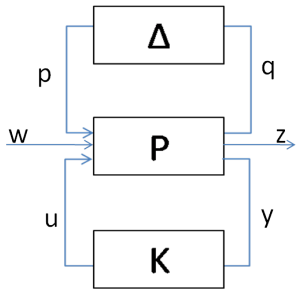

Figure A.3: Standard form of the system.

The definition of the variables in Fig. A.3 for our model is given below:

$$\begin{aligned} w &= \begin{bmatrix} d_1 & d_2 & d_3 \end{bmatrix}^T \\ z &= \begin{bmatrix} F_c & u \end{bmatrix}^T \\ y &= \begin{bmatrix} x_1 & x_2 & F_c \end{bmatrix}^T \end{aligned} \tag{A.5}$$

In (A.5) $d_1 \equiv d$, is the position disturbance on the contact surface, d_2 and d_3 are additional force disturbances on the masses m_1 and m_2. These disturbances are included to make the system well suited to H_∞ and H_2 design methods. The output variable z which we attempt to minimize includes the contact force F_c and the control input u. As is usually done, we shall ignore the upper half of the system in Fig. A.3 for the control design procedure. The definition in (A.5) is going to be used for the most part in the rest of this document. However, there is another approach suitable for control-structure synthesis wherein the force F_s due to the structural element is treated as a control input. Therefore the control input is augmented with the variable F_s i.e $u = [F_a \; F_s]^T$. This

approach shall be briefly described at the end of this section.

A.1.2 A Simplified Problem: Stand-alone Control Synthesis

For the purpose of gaining some intuition for the problem at hand, we shall first consider a simplified design problem for the system described by (A.4, A.3 and A.5). Here we shall attempt to synthesize the controller K only, while keeping the structural stiffness k_s fixed to some reasonable value. We shall first use H_∞ design to synthesize our controller.

The objective is to find a controller K such that the infinity norm of the transfer function $\|T_{zw}\|_\infty$ from w to z is less than some bound γ, given the structural stiffness k_s. The Bode plot of for the open loop system, and two systems with different penalties on the control input are shown in Fig. A.4.

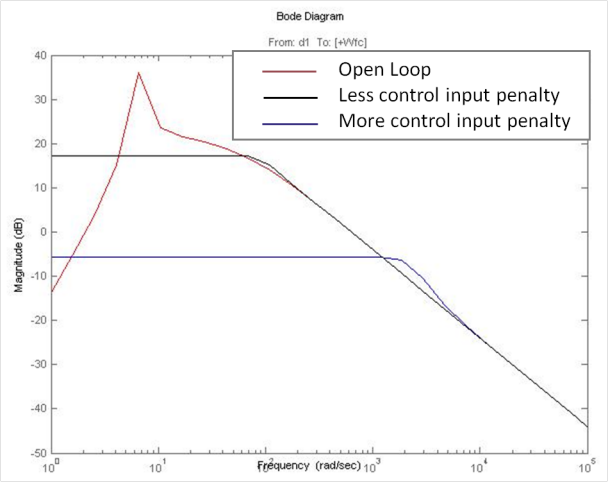

Figure A.4: Bode plot of transfer function from d_1 to F_c.

Fig. A.4 shows that the H_∞ controller can reduce the H_∞ norm of the transfer function provided the dominant pole of the open loop transfer function is within the bandwidth of the controller. As the pole moves further away from the controller bandwidth, it becomes harder to reduce the H_∞ norm. This motivates the need for working with the controller and the mechanical structure of the system simultaneously.

Fig. A.5 shows the time domain response of the closed loop system with a synthesized controller K, to a step disturbance d_1. For this system, $\|T_{zw}\|_\infty = 7.29$ and $\|T_{zw}\|_2 = 2144.8$. As can be seen, the H_∞ design is good at attenuating the peak of the force F_c, but does not do particularly well at regulating the force to zero. Instead it has a fairly large steady state error. This problem can possibly be reduced by the use of an integrator in the H_∞ controller.

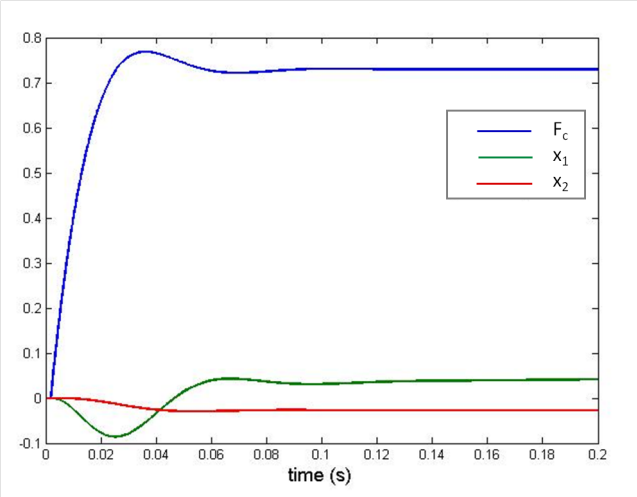

Figure A.5: Time domain response to a step disturbance d_1.

A.1.3 Control-Structure Synthesis

We now focus our attention to the complete problem of synthesizing both the control and mechanical structure simultaneously. The design objective for our synthesis procedure shall be to minimize $\|T_{zw}\|_\infty$ over the control u and the structural stiffness k_s. We are therefore, attempting to minimize the infinity norm of the transfer function over a larger number of matrices. The algorithm we shall use to do this is described in Fig. A.6

Fig. A.7 shows the Bode plot for the first and final iteration of the algorithm described in Fig. A.6. The figure clearly shows a reduction in $\|T_{zw}\|_\infty$. If Fig. A.7bis seen carefully, it can be noticed that both the control and the structure play an important role in reducing $\|T_{zw}\|_\infty$. The controller K reduces the magnitude of the first peak, while the stiffness k_s reduces magnitude of the second

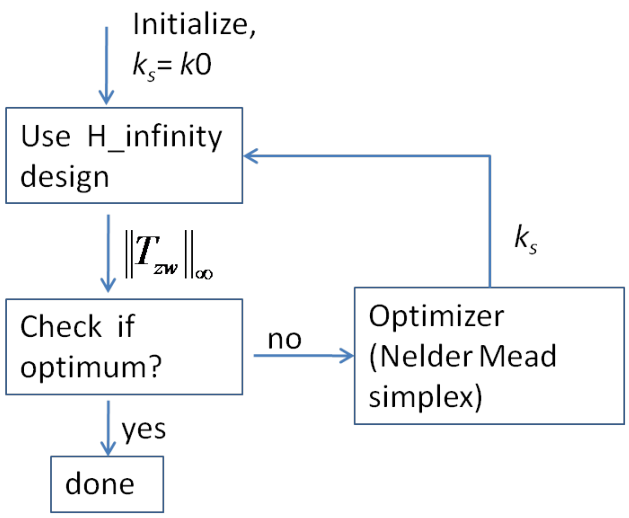

Figure A.6: Optimization procedure for control-structure synthesis.

peak. Thus, the controller and the structure work together to decrease $\|T_{zw}\|_\infty$.

Although the H_∞ norm for system obtained after control-structure synthesis is significantly lower than the original system, the Bode plot in Fig. A.7b reveals the fact that H_∞ is perhaps not the best strategy at lower frequencies. It can be seen that at lower frequencies, the magnitude of the Bode plot for the open loop system is lower than that of the system with an H-infinity based controller. This informs us that at lower frequencies which are not close to the poles of the system, a different controller may be better.

A.1.4 An Alternate Approach

For the system being studied it is also possible to replace k_s by a second control input u_2. We shall ultimately replace the synthesized controller K_2 for this control input with a physical system that approximates the behavior of the controller. Since this synthesized controller represents a physical system it can be treated as an infinite bandwidth controller. The artificial controller for the artificial input u_2 along with the actual controller for input u can be synthesized using H_∞ design. Once this is done the controller can be approximated by a physical system consisting of masses and springs

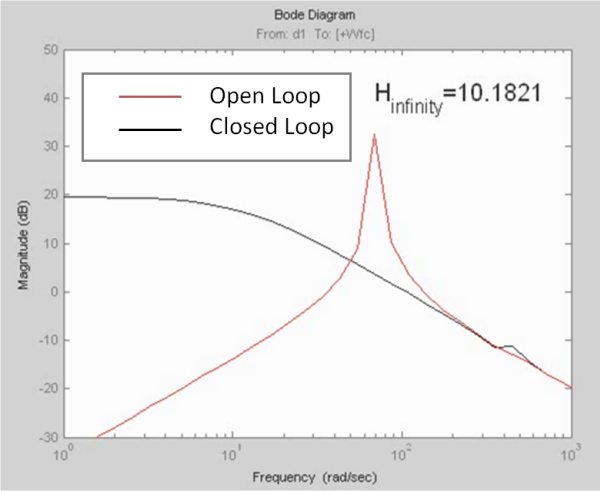

(a) Bode plot from w to z at the first iteration of the algorithm

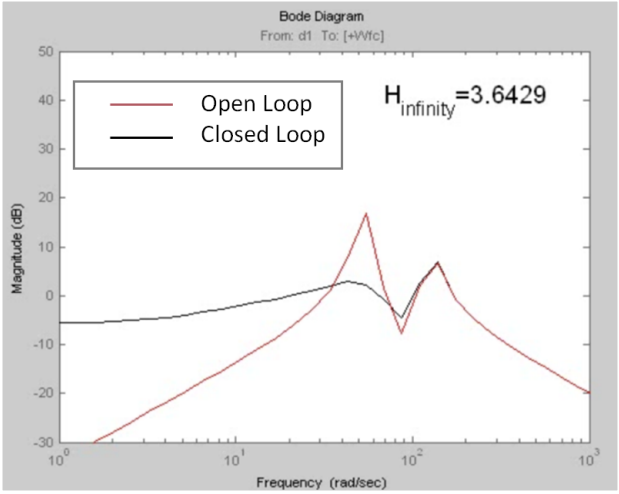

(b) Bode plot from w to z at the final iteration of the algorithm

Figure A.7: Bode plot for first and final iteration of the control-structure synthesis procedure

as shown in Fig. A.8. In the approximation $\|\Delta\|_\infty$ may be limited based on robust stability margin obtained for the previously synthesized controller for the input u.

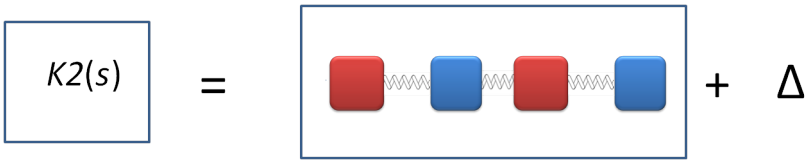

Figure A.8: Optimization procedure for control-structure synthesis.

This approach has not been entirely explored. We mention it here only to bring up the possibility of generalizing the closed loop synthesis procedure to allow synthesis of structural topologies in addition to structural parameters such as stiffness.

Appendix B

User Study Protocol

In this chapter we will present the CMU IRB approved protocol and associated material that was utilized to conduct the user study in Sec. 9.3 of Chapter 9. The CMU IRB application which includes the study protocol, the consent form and questionnaire used in the user study are included in the following pages.

Carnegie Mellon University

For IRB Office Use
IRB No:_____
Rec'd:_____

APPLICATION FOR IRB REVIEW OF RESEARCH INVOLVING HUMAN SUBJECTS

(Not for exempt research)

Please complete this application as thoroughly as possible. Your application should include the following:

1. A consent form using the current CMU template that the participants and/or parent/guardian will be required to sign.
2. A copy of any questionnaires, surveys, images, de-briefings that will be used.
3. A copy of any recruitment documents (including advertisements, flyers, letters, invitations, email) to be used;
4. A copy of the training certificates for all individuals working on the research unless they are on file with the CMU IRB. Training is available at: http://www.citiprogram.org. See the IRB website for details.
5. If the PI is a student, the faculty advisor must submit a Faculty Advisor Assurance Form.

Please email all documents to irb-review@andrew.cmu.edu. For assistance call the CMU Office of Research Integrity and Compliance @ 412-268-5460 or email irb-review@andrew.cmu.edu. Additional information and templates are available at http://www.cmu.edu/osp/regulatory-compliance/human-subjects.html

1. Protocol		
Title: Robot-Assisted Feeding using the Inflatable Manipulator		
☐ This is a previously approved study that has lapsed.	Previous IRB No: HS	
2. Principal Investigator (PI)		
Name: Siddharth Sanan		Department: Robotics
Telephone: 412-999-6115	E-mail: sanan@cmu.edu	Training Cert. ☒ Attached ☐ On File
☒ I am a student. If so, please provide information about your faculty advisor below.		
Faculty Advisor Name: Christopher G. Atkeson	E-mail: cga@cmu.edu	Training Cert. ☐ Attached ☒ On File
If a student is the PI, the faculty advisor must complete and submit a Faculty Advisor Assurance Form.		
If there is someone other than PI to correspond with regarding this protocol, please list below.		
Contact Person Name:	Telephone:	E-mail:
Business Manager for your department:		E-mail:
3. Co-investigators		
Name:	E-mail:	Training Cert. ☒ Attached ☐ On File
Name:	E-mail:	Training Cert. ☐ Attached ☐ On File
Name:	E-mail:	Training Cert. ☐ Attached ☐ On File
Name:	E-mail:	Training Cert. ☐ Attached ☐ On File
Name:	E-mail:	Training Cert. ☐ Attached ☐ On File
Name:	E-mail:	Training Cert. ☐ Attached ☐ On File
Name:	E-mail:	Training Cert. ☐ Attached ☐ On File
4. Funding		
☐ Unfunded research	☒ External Funding	☐ Internal Funding
Sponsor/Source: ☒ NSF ☐ NIH ☐ Other, please specify:		
Grant Title: Quality of Life Technology Engineering Research Center #0540865		
If federally funded, is this application consistent with the grant? ☒ Yes ☐ No		
Is CMU the prime recipient of funding? ☒ Yes ☐ No	Is CMU a sub-recipient? ☐ Yes ☐ No	

For IRB Office Use

IRB No:_____

Rec'd:_____

☐ SPEX Proposal #:	☐ SPEX Award #:

If you don't know the funding/grant information, please get it from your department's business manager.

5. Protocol Description

a. Provide, in lay terms, a summary of your proposed study as outlined below. You may attach the protocol to this form if you like.
This study aims to evaluate the usability of a new inflatable manipulator for providing assistance during a feeding task.

b. What is the purpose of the study (what is your research question) and how will the data collected be used? The purpose of the study is to gather preliminary evidence of the usability of a new inflatable robotic manipulator for providing assistance to non-disabled adults during a feeding task. Consistent with principles of user-centered design, the data thus gathered will be used to improve the design and functionality of the manipulator.

c. Describe the research procedures (include the activity(s), location(s) and time required of the participant).

Inflatable Manipulator:

The Inflatable Manipulator consists of a soft light-weight inflatable structure (as shown in Addendum, Fig. 1), that is similar to an inflatable pool toy and is very safe for use near humans. The base of the manipulator (as shown in Addendum, Fig. 1), that houses all the motors to drive this inflatable structure, is mounted on a table. This base is stable to tipping and needs deliberate action to be moved. The manipulator has four degrees of freedom, i.e., it can move its wrist (as shown in Addendum, Fig. 1) in 3D position space and also orient it in a plane. The robotic manipulator is equipped with a Kinect sensor to obtain visual perception of its environment, which is used to infer the location of human in its workspace.

The robot can be commanded to stop power to all motors at any time by both the investigator (using keyboard, control pad, etc.) as well as the subject (using the provided STOP button). In addition, all power to the robot can be completely shut off at any time by the investigator using a hardware switch. In either case, when the power supply to the motors is shut off, the inflatable structure gradually falls to its natural position under gravity. Since this inflatable structure is extremely light-weight (< 1 ounce), this falling motion poses minimal risk to the subject.

Location and Duration:

The study will be conducted at Carnegie Mellon University, Newel Simon Hall A428, Pittsburgh, PA. The expected duration of subject's participation in the study is approximately 1 hour.

Procedure:

In this study, the subjects will be fed a food item by the inflatable robotic manipulator. The subject may also choose to get their face wiped by the robot. After the feeding task is completed, the subject will be asked to rate their experience with the robot by responding to a questionnaire and/or few verbal questions. The entire session will be video recorded.

The details of the procedure are given below:

- After providing written informed consent, the subject will be shown a video depicting the inflatable robotic manipulator feeding the PI while seated in the laboratory in Newell-Simon Hall.
- The subject will be then shown the robot and oriented to its functionalities. The subject will also be shown how to STOP the robot at any time during the task.
- The subject will be informed of the food item that will be fed to him/her by the inflatable robot. The food items may include pudding, cereal, yogurt, applesauce, canned fruit, etc.
- The subject will be provided protective eyewear to be worn during the task. The subject will also be offered an apron or bib to wear, if they prefer.
- When the subject is ready to proceed with the feeding task, the investigator will first issue a "Pick up food" command to the robot. The robot will then pick up the food item from a dish using a feeding utensil such as a rubberized spoon attached to the wrist of the manipulator. The investigator will then issue a "Bring food close to mouth" command, upon which the robot will proceed to bring the food close to the subject's mouth. The subject will then be asked to eat the food item. At this time, the subject may choose to get his/her mouth wiped by the robot. If the subject chooses to do so, the investigator will issuing a "Wipe face" command to the robot. This command causes the robot's tool to change from a spoon to a towel, which is used to wipe the subject's face. This this procedure will be repeated at least 3 times.
- After completing the above feeding task, the subject will be asked to rate their experience with the robot by responding to a questionnaire and/or few verbal questions. Specifically, they will be queried about their comfort and sense of safety while being fed.

d. Who will be asked to participate? Typical adults, without any disability

e. Will questionnaires or surveys be used? ☒ Yes ☐ No If yes, please attach.

f. Will tasks be done on a computer? ☐ Yes ☒ No
If yes, how will the tasks be accessed? ☐ Remotely via the internet? ☐ In the research lab? ☐ Other, please explain:

g. Will deception be used? ☐ Yes ☒ No
If yes, describe how participants will be debriefed. Please include the de-briefing material and/or script.

h. In what country will the research be conducted (check all that apply)? ☒ United States ☐ Qatar
☐ Other country, please list:

i. Will the research be conducted on a CMU campus? ☒ Pittsburgh ☐ Silicon Valley ☐ Qatar ☐ No
If no, please indicate the location(s).
If applicable, please attach documentation of permission to conduct research in private, non-CMU space.

6. Participants

a. Will any of the following classes of vulnerable subjects be involved in the proposed study? *(check all that apply)*

Class	*Comments*
Pregnant women, human fetuses ☐ Yes ☐ No ☒ Pregnant women will not be specifically included or excluded. (See http://www.hhs.gov/ohrp/humansubjects/guidance/45cfr46.htm, research that is incidental to pregnancy and has no risk to the fetus can only include pregnant women if ALL aspects of Subpart B are met.)	
Neonates ☐ Yes ☒ No	
Prisoners ☐ Yes ☒ No	
Children ☐ Yes ☒ No	

b. Individuals with compromised mental status ☐ Yes ☒ No
If yes, indicate how this will be determined.

For IRB Office Use

IRB No:_____

Rec'd:_____

c. Will the participants be capable of understanding the nature of the study and the consent process? ☒ Yes ☐ No
If no, explain.

d. What is the age range of participants in the proposed study? 18 years and older

e. How many participants are needed for the study? 10
How was that number determined? Consistent with usability testing, we will be recruiting a small sample and have not conducted a power analysis to determine sample size. We anticipate that our small number of participants will be sufficient to achieve our iterative design objective.

f. What do you estimate the ratio of males to females to be? 50:50
Will this be reflective of the local population? ☒ Yes ☐ No
Will you target a certain population? ☐ Yes ☒ No Please explain

g. Do you anticipate that your participants will represent a cross-section of the population in the region where the study is being conducted? ☒ Yes ☐ No
If yes, please describe and estimate the percentage that will be from minority groups. 20%
If no, please describe your study population and address why minority representation is not considered.

h. Please list inclusion and exclusion criteria.
Inclusion criteria:
- Age 18 and older
- Able to read and understand the consent form

Exclusion criteria:
- Any physical or mental disability
- Known allergy to food items used in the study

7. Participant Recruitment

a. Describe how participant recruitment will be performed. Include how and by whom potential participants are introduced to the study. Participants will be solicited using emails on mailing lists (misc.cmu) and posters at CMU (see attached recruitment poster/email template).

Check all boxes below that apply.

☒ Flyers Where will they be posted? CMU campus

☐ Radio, TV

☒ E-mail solicitation Indicate how the email addresses are obtained.public email lists like misc.cmu

☐ Web-based solicitation. Specify sites:

☐ Participant Pool. Specify what pool:

☐ Other, please specify:

b. Will participants undergo screening prior to their participation? If yes, please describe. No

Please attach any recruiting materials you plan to use and the text of e-mail or web-based solicitations you will use.

8. Consent

a. Do you plan to use consent forms? ☒ Yes ☐ No
If no, you must complete the section 8e below on waiver of informed consent.
If yes, describe how consent will be obtained and by whom. Written informed consent will be obtained by the PI prior to initiating any study procedures.
Will consent be obtained online? ☐ Yes ☒ No
If yes, you must request a waiver of written documentation below in section 8h.

For IRB Office Use

IRB No:_____

Rec'd:_____

b. If participants are minors will assent forms be used? ☐ Yes ☐ No If no, please explain. ☒ NA no minors

c. Will the consent form be presented on paper or online? ☒ Paper ☐ Online

d. Are you requesting to use a consent format that is different from the CMU model consent? ☐ Yes ☒ No
If yes, please explain.

e. Are you requesting a **waiver of informed consent**? ☐ Yes ☒ No
If yes, please explain how each of the elements listed apply to your request for a waiver:
- The research involves no more than minimal risk to the subjects;
- The waiver will not adversely affect the rights and welfare of the subjects;
- The research could not practicably be carried out without the waiver and ;
- Whenever appropriate, the subjects will be provided with additional pertinent information after participation.

Explain:

f. Is the waiver for all study participants? ☐ Yes ☐ No
If no, to whom does the waiver apply?

g. Is the waiver for all study procedures? ☐ Yes ☐ No
If no, to what procedures does the waiver apply?

h. Are you requesting a **waiver of written documentation** (signed) of informed consent? ☐ Yes ☒ No
If yes, please indicate which one of the following applies:
☐ The only record linking the participant and the research will be the consent document and the principal risk to the participant harm would be from breach of confidentiality.
☐ I consider this a minimal risk study that involves no procedures for which written consent is normally required outside of research.

i. Explain how the study meets the criteria checked above.

9. Risks and Benefits (Note: payments to participants are not considered to be a benefit)

a. Will participants receive intangible benefit from the study? ☐ Yes ☒ No

b. Discuss the direct and indirect benefits to participants. The participants will gain knowledge of state-of-the-art robotics research being conducted at CMU, and they may derive satisfaction from helping to improve robotic manipulation for feeding.

c. Discuss the risks to participants. 1) Injury resulting from contact with the robotic manipulator or feeding utensil; 2) Anxiety related to the robot's proximity to the participant; 3) Soiling of clothing; 4)Breach of confedentiality

d. Discuss how any risks will be managed and/or minimized.

To minimize risk of injury:
The inflatable manipulator consists of an entirely soft lightweight inflatable moving structure and therefore, is very safe for use near humans. This inflatable structure can be thought of as an inflatable pool toy, which is unlikely to cause physical injury. Preliminary investigations by the researchers regarding collisions with inflatable robots support this intuition, and this has been our experience in the laboratory as the manipulator has been developed. Therefore, accidental physical contact with the inflatable structure poses minimal risk to the subject. The only significant non-inflatable appendage on the inflatable structure will be the feeding utensil (rubberized spoon). All edges on the spoon will be rounded, minimizing the risk of puncture wounds, lacerations or contusions due to contact with the spoon. The spoon will also be extremely lightweight because of its plastic construction. To prevent any accidental contact of the manipulator with the subject's eyes, protective eyegear will be mandatory for all subjects and will be made available by the investigator.

To minimize risk of anxiety:
Subjects will be oriented to the robot and its functionalities before interacting with it, so that they know its capabilities and limitations when moving within their personal space. In addition, the robot's design includes software and hardware stops that completely render the system powerless, when necessary, to minimize accidental contact. At all times during every experiment, the subject and the investigator will have access to buttons that can shut-off power supply to the system. When power is shut-off, the inflatable structure does not maintain its position, but rather falls under gravity to its rest position. Since the inflatable structure is lightweight (< 1 ounce) and will not be carrying a heavy payload, its free motion under gravity does not pose a significant risk.

To minimize risk of soiled clothing:
Subjects will be offered to wear an apron or bib during the feeding task.

To minimize risk of breach of confidentiality:
All study data will be coded by assigning a unique case number. The information linking the case number to the subject's identity will be stored electronically in a secure machine with restricted access. The study data and consent forms will be stored in separate secure locations at CMU, with access available only to the investigators involved in the study. All email correspondence with prospective subjects will be carried out via a secure CMU email account that is accessible by only the PI of the study.

e. If deception is involved, please explain.

f. Indicate the degree of physical or psychological risk you believe the research poses to human subjects *(check which one applies).*

☒ Minimal Risk: A risk is minimal where the probability and magnitude of harm or discomfort anticipated in the proposed research are not greater, in and of themselves, than those ordinarily encountered in daily life of during the performance o routine physical or psychological examinations or tests.

☐ Greater than Minimal Risk: A risk is greater than minimal where the probability and magnitude of harm or discomfort anticipated in the proposed research are greater than those ordinarily encountered in daily life or during the performance of routine physical or psychological examinations or tests.

g. Describe how the study fits in this risk level. The magnitude and probablity of harm have been minimized by various hardware design choices and study protocols.

10. Participant Compensation and Costs

a. Are participants to be compensated for the study? ☒ Yes ☐ No
If yes, what is the amount, type and source of funds?

Amount: **$20**	Source:Grant	Type (gift card, cash):Cash

b. Will participants who are students be offered class credit? ☐ Yes ☒ No
If yes, please indentify the class and instructor.

c. Are other inducements planned to recruit participants? ☐ Yes ☒ No
If yes, please describe.

d. Are there any costs to participants? ☐ Yes ☒ No
If yes, please explain.

e. Will you compensate participants for injury resulting from participation? ☐ Yes ☒ No ☐ NA
If yes, please describe.

11. Confidentiality and Data Security

a. Will personal identifiers be collected? ☒ Yes ☐ No

If yes, list the personal identifiers to be collected. Personal identifiers such as name, signature, age and gender will be collected.

b. Will identifiers be translated to a code? ☒ Yes ☐ No
If no, indicate why.

c. Will audio recordings be made? ☐ Yes ☒ No
If yes, please describe.

d. Will video recordings be made? ☒ Yes ☐ No
If yes, please describe. Video recording of the entire session will be made. Identifiers will be removed from these recordings.

e. Is the information so sensitive that you will obtain a certificate of confidentiality from NIH? ☐ Yes ☒ No

f. Who will have access to data (surveys, questionnaires, recordings, interview records, etc.)? Investigators assigned to this study will have access to data. Research records may be disclosed, if required by federal law.

g. Describe how you will protect participant confidentiality and secure research records (Will they be stored on a secure computer, locked cabinet, etc?). All study data will be coded by assigning a unique case number. The information linking the case number to the subject's identity will be stored electronically in a secure machine with restricted access. The study data and consent forms will be stored in separate secure locations at CMU, with access available only to the investigators involved in the study. All email correspondence with prospective subjects will be carried out via a secure CMU email account that is accessible by only the PI of the study.

h. Describe your process for monitoring data to ensure that study goals are met. (Review of lab notebooks, frequency of meetings to review data, who will be present at the meetings, how recruitment and retention will be monitored, etc.) Analysis on the data collected will be performed by the investigators involved in the study. Weekly meetings to review the study progress will be held to ensure study procedures are being followed and to discuss any unforeseen concerns that might have arisen during the study.

12. Conflict of Interest

Do you or any individual who is associated with or responsible for the design, the conduct of or the reporting of this research have an economic or financial interest in, or act as an officer or director for any outside entity whose interests could reasonably appear to be affected by this research project? ☐ Yes ☒ No
If yes, please provide detailed information to permit the IRB to determine if such involvement should be disclosed to potential research subjects.

13. Cooperating Institutions

a. Is this research being done in cooperation with any institutions, individuals or organizations not affiliated with CMU? ☐ Yes ☒ No
If yes, please list and describe their role in this research.

b. Have you received IRB approval from another IRB for this study? ☐ Yes ☒ No ☐ Pending
If yes, please attach a copy of the IRB approval.

c. If multiple institutions are involved in this study indicate who is responsible for oversight of the entire study. N/A

If applicable, please provide the name(s) and address(es) of all officials authorizing to access human subjects in cooperating institutions not affiliated with CMU. N/A

Please attach documentation of approval.

Principal Investigator's Assurance Statement for Using Human Subjects in Research

Carnegie Mellon University

For IRB Office Use
IRB No:_____
Rec'd:_____

I certify that the information provided in this IRB application is complete and accurate.

I understand that as Principal Investigator, I have ultimate responsibility for the conduct of IRB approved studies, the ethical performance of protocols, the protection of the rights and welfare of human participants, and strict adherence to the studies protocol and any stipulations imposed by Carnegie Mellon University Institutional Review Board.

I understand that it is my responsibility to ensure that the human participants' involvement as described in the funding proposal(s) is consistent in principle, to that contained in the IRB application. I will submit modifications and/or changes to the IRB as necessary.

I agree to comply with all Carnegie Mellon University policies and procedures, as well as with all applicable federal, state, and local laws, regarding the protection of human participants in research, including, but not limited to:

- Ensuring all investigators and key study personnel have completed human subjects training program;
- Ensuring protocols are conducted by qualified personnel following the approved IRB application;
- Implementing no changes in approved IRB applications or informed consent documents without prior IRB approval in accordance with CMU IRB policy (except in an emergency, if necessary to safeguard the well-being of a human participant, and will report to the IRB within 1 day of such change);
- Obtaining the legally effective informed consent from human participants or their representative, using only the currently approved date-stamped informed consent documents, and providing a copy to the participant.
- Ensuring that only IRB-approved investigators for this study obtain informed consent from potential subjects.
- Informing participants of any relevant new information regarding their participation in the research that becomes available.
- Promptly reporting to the IRB any new information involving risks to research participants, including reporting to the IRB, Data Safety and Monitoring Boards, sponsors and appropriate federal agencies any adverse experiences and all unanticipated problems involving risks to human subjects or others that occur in the course of the research.
- If unavailable to conduct research personally, as when on sabbatical leave or vacation, arrangements for another investigator to assume direct responsibility for studies will be made through modification requests to the IRB;
- Promptly providing the IRB with any information requested relative to protocols;
- Promptly and completely complying with IRB decisions to suspend or withdraw approval for projects;
- Obtaining Continuing Review approval prior to the date the approval for a study expires (approval for the study will automatically expire);
- Maintaining accurate and complete research records, including, but not limited to, all informed consent documents for 3 years from the date of study completion;
- Informing the CMU IRB of all locations in which human participants will be recruited for protocols and being responsible for obtaining and maintaining current IRB approvals/letters of cooperation when applicable;
- Complying with federal, state and local laws and regulations and sponsor terms and conditions; and
- Complying with CMU policies on the responsible conduct of research.

Siddharth Sanan 12/19/2012

Principal Investigator Name and Signature Date

Note: If e-mailed from the PI's CMU e-mail account a hand written signature is not needed. Please type in name and date. If the PI is a student, the faculty advisor must submit a Faculty Advisor Assurance Form.

Please email all documents to irb-review@andrew.cmu.edu.

Note: Links to the policies and Federal regulations for the protection of human research subjects (including the Code of Federal Regulations [.CF.R.] Title 45 CFR Part 46 and Title 21 C.F.R. parts 50 and 56) are available on the IRB web page

For IRB Office Use

IRB No:_____

Rec'd:_____

(http://www.cmu.edu/provost/spon-res/compliance/hs.htm).

Comments:

Addendum to Protocol:
Robot-Assisted Feeding using the Inflatable Manipulator

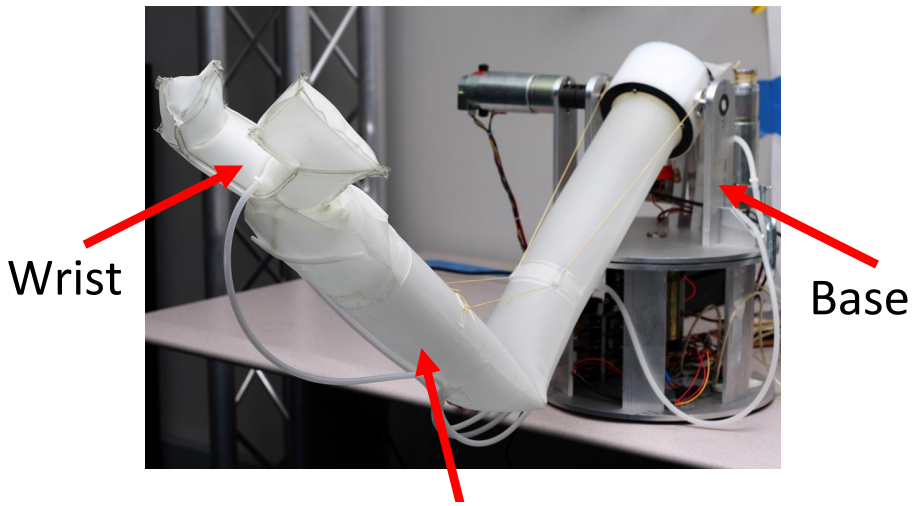

Fig. 1: The Inflatable Manipulator with the base, inflatable structure and wrist shown. The base is used to actuate the inflatable structure that has a wrist at the end. The wrist is also inflatable. The inflatable structure does not have a rigid skeleton inside it.

Carnegie Mellon University

Consent Form for Participation in Research

Study Title: Robot-Assisted Feeding using the Inflatable Manipulator

Principal Investigator:
Siddharth Sanan
The Robotics Institute
NSH A428
Pittsburgh, PA 15213
Email: sanan@cmu.edu
412-999-6115

Faculty Advisor:
Christopher G. Atkeson
The Robotics Institute
NSH A428
Pittsburgh, PA 15213
Email: cga@cmu.edu

Purpose of this Study
The purpose of this study is to evaluate usability of a new inflatable robotic arm (as shown in Fig. 1) for providing assistance to adults during a feeding task. The data gathered from the study will be used to improve the design and functionality of the inflatable robotic arm.

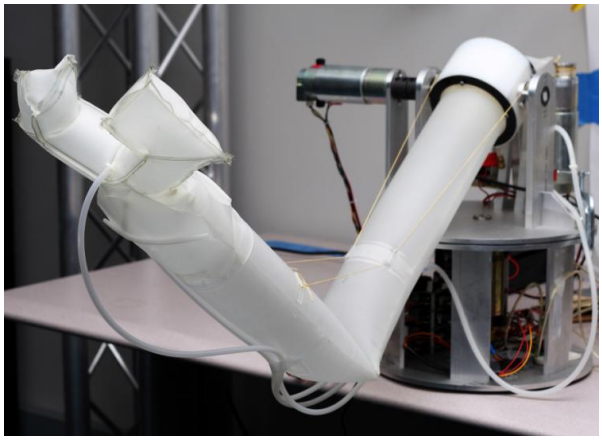

Fig. 1: Inflatable Robotic Arm

Consent Form for Participation in Research

Procedures

This study is estimated to take 1 hour to complete and will be conducted at the following address:
Carnegie Mellon University
5000 Forbes Ave
Newell Simon Hall A428
Pittsburgh, PA 15213

In this study, you will be fed a food item with the help of an inflatable robotic arm (Fig. 1). The task of feeding will be divided into four smaller tasks: 1) robot picking up food, 2) robot bringing the food item close to your mouth, 3) you eating the food item, and 4) robot wiping your face (optional). This series of tasks will be repeated at least three times. After the feeding task is completed, you will be asked to rate your experience with the robot arm by responding to a questionnaire and/or verbal questions. The entire study will be video recorded.

The details of the procedures are given below:

1. You will be shown a video of the inflatable robotic arm feeding a person.
2. You will then be familiarized with the robot arm and oriented to its functionalities. You will be shown how to STOP the robot at any time during the task. There is no harm to the robot if you issue a stop command, so you should not hesitate to issue a stop command at any time.
3. You will be informed of the food item being used in the task. If the food item is not to your preference, you can request the use of a different food item that is available.
4. At this point, you will be provided with protective eyewear that you will be required to wear during the task. Aprons and bibs will also be made available and you can choose to wear these.
5. When you are ready to proceed with the feeding task, the investigator will command the robot to pick up the food item using a spoon from a dish in front of you.
6. After the robot arm finishes picking up the food item, the investigator will ask the robot to bring food close to your mouth.
7. When the robot arm brings the food close to your mouth, the investigator will ask you to eat the food item from the spoon.
8. After eating the food item, if you wish to wipe your face, you may indicate this to the investigator. If you do so, the investigator will command the robot arm to wipe your face with a towel. You can choose to skip this step.
9. The feeding task (steps 5 to 8) will be repeated at least 3 times.
10. After completing the feeding task with the robot arm, you will be asked to rate your experience with the robot arm by responding to a questionnaire and/or verbal questions.

Consent Form for Participation in Research

Participant Requirements
You must be above the age of 18 to participate and have no physical or mental disabilities. You must be able to read and understand the contents of this consent form.

Risks
During the task, the inflatable robotic arm may have accidental contact with you. Since the arm has a soft and lightweight inflatable structure, accidental contact poses minimal risk of physical injury to you. To minimize any risk of injury due to the spoon attached at the end of the inflatable arm, it will be made of plastic and will have rounded edges. You will be provided with protective eyewear during the study to prevent any accidental contact of the arm with your eyes.

You may also not be certain of the robot's intent and actions during the task. To reduce your discomfort regarding the robot's movements, the investigator will familiarize you with the robot and its functions. The investigator will be present during the entire duration of the task and can stop the robot at any time. You will also have the ability to stop the robot at any time during the task using the provided stop button. You will be shown how to use this stop button before the feeding task begins.

Food spillage may also occur during the task. Aprons and bibs will be available for use by you during the study.

There is a risk that confidentiality of your personal identifiable information may be compromised. This risk will be minimized by assigning a unique case number to the data collected from this study. The information linking the case number to your identity will be stored electronically in a secure machine with restricted access. The study data and consent forms will be stored in separate secure locations at CMU, with access available only to the investigators involved in the study. Your email address will be kept confidential. All email correspondence with you was carried out via a secure CMU email account that is accessible by only the PI of the study.

Benefits
There is no personal benefit to you from your participation in the study, but the knowledge received may be of value to robotics research conducted at Carnegie Mellon University and humanity.

Compensation & Costs
You will be compensated $20 (cash) upon completion of the study. Partial payment will not be given if you choose to withdraw from the study at any time.

Consent Form for Participation in Research

There will be no cost to you if you participate in this study.

Confidentiality

By participating in the study, you understand and agree that Carnegie Mellon may be required to disclose your consent form, data and other personally identifiable information as required by law, regulation, subpoena or court order. Otherwise, your confidentiality will be maintained in the following manner:

Your data and consent form will be kept separate. Your consent form will be stored in a locked location on Carnegie Mellon property and will not be disclosed to third parties. By participating, you understand and agree that the data and information gathered during this study may be used by Carnegie Mellon and published and/or disclosed by Carnegie Mellon to others outside of Carnegie Mellon. However, your name, address, contact information and other direct personal identifiers in your consent form will not be mentioned in any such publication or dissemination of the research data and/or results by Carnegie Mellon.

The researchers will take the following steps to protect participants' identities during this study: (1) Each subject will be assigned a unique number; (2) The researchers will record any data collected during the study by number, not by name; (3) Only members of the research group will view collected data in detail; (4) Any recordings or data files will be stored in a secured location accessed only by authorized researchers.

Optional Permission

I understand that the researchers may want to use portions of any video or audio recording for illustrative reasons in presentations of this work for scientific or educational purposes, including videos put on the internet (research web pages, youtube.com, etc.). I give my permission to do so provided that my name will not appear.

☐ YES ☐ NO (Please initial here _____)

Rights

Your participation is voluntary. You are free to stop your participation at any point. Refusal to participate or withdrawal of your consent or discontinued participation in the study will not result in any penalty or loss of benefits or rights to which you might otherwise be entitled. The Principal Investigator may at his/her discretion remove you from the study for any of a number of reasons. In such an event, you will not suffer any penalty or loss of benefits or rights which you might otherwise be entitled.

Consent Form for Participation in Research

Right to Ask Questions & Contact Information
If you have any questions about this study, you should feel free to ask them now. If you have questions later, desire additional information, or wish to withdraw your participation please contact the Principal Investigator by mail, phone or e-mail in accordance with the contact information listed on the first page of this consent.

If you have questions pertaining to your rights as a research participant; or to report objections to this study, you should contact the Research Regulatory Compliance Office at Carnegie Mellon University. Email: irb-review@andrew.cmu.edu . Phone: 412-268-1901 or 412-268-5460.

Voluntary Consent
By signing below, you agree that the above information has been explained to you and all your current questions have been answered. You understand that you may ask questions about any aspect of this research study during the course of the study and in the future. By signing this form, you agree to participate in this research study.

PARTICIPANT SIGNATURE DATE

I certify that I have explained the nature and purpose of this research study to the above individual and I have discussed the potential benefits and possible risks of participation in the study. Any questions the individual has about this study have been answered and any future questions will be answered as they arise.

SIGNATURE OF PERSON OBTAINING CONSENT DATE

Robot-Assisted Feeding using the Inflatable Manipulator

Questionnaire

1. In general, how comfortable or uncomfortable you were being fed by the robot?
   (circle one number below; 1 – Completely Uncomfortable; 10 – Completely Comfortable)

   1 2 3 4 5 6 7 8 9 10

2. How easy or difficult was it to eat with the assistance of the robot?
   (circle one number below; 1 – Extremely Difficult; 10 – Extremely Easy)

   1 2 3 4 5 6 7 8 9 10

3. How concerned were you about safety when being fed by the robot?
   (circle one number below; 1 – Extremely Concerned; 10 – Not At All Concerned)

   1 2 3 4 5 6 7 8 9 10

4. How much would you trust the robot versus a human caregiver to help you eat safely, if you needed assistance while eating?
   - ☐ Trust the robot a lot less than a human to help me eat safely
   - ☐ Trust the robot a little less than a human to help me eat safely
   - ☐ Trust the robot and human about the same to help me eat safely
   - ☐ Trust the robot a little more than a human to help me eat safely
   - ☐ Trust the robot a lot more than a human to help me eat safely

5. How do you think the robot would compare to a human caregiver in terms of providing efficient (i.e., timely) help with eating?
   - ☐ Robot would provide much less efficient assistance with eating than a human
   - ☐ Robot would provide slightly less efficient assistance with eating than a human
   - ☐ Robot and human would be equally efficient
   - ☐ Robot would provide slightly more efficient assistance with eating than a human
   - ☐ Robot would provide much more efficient assistance with eating than a human

6. Which of the following statements about social interaction while eating best describes your usual preference?
   - ☐ I prefer not to interact socially when I eat
   - ☐ I'm fine with a little conversation while I eat, but not too much
   - ☐ I prefer to combine a eating a meal with having a stimulating conversation
   - ☐ The conversation and socializing is more important than the food

7. How important would it be for you to have a robot that could interact socially (e.g., talk, express emotion) while helping you eat?
   - ☐ Extremely important - without social interaction I would prefer a human caregiver
   - ☐ Somewhat important - I prefer social interaction, but I would be OK with a non-social robot
   - ☐ Not important – I prefer a non-social robot

8. Overall, to what extent would you prefer having a robot versus a human provide assistance with eating, if you needed assistance while eating?
   ☐ Definitely prefer robot
   ☐ Probably prefer robot
   ☐ No preference
   ☐ Probably prefer human
   ☐ Definitely prefer human

9. If you were using this robot to assist you with eating, how much control would you want over the operation of the technology versus allowing the system to be automated?
   ☐ 100% automatic
   ☐ 75% automatic, 25% user control
   ☐ 50% automatic, 50% user control
   ☐ 75% user control, 25% automatic
   ☐ 100% user control

10. How well do you think each of the following statements describe this technology? Please rate how accurate you think each is in describing this specific technology application.
    (check <u>one</u> box for each item below; 1 – Not At All Accurate; 10 – Extremely Accurate)

	1	**2**	**3**	**4**	**5**	**6**	**7**	**8**	**9**	**10**
I was anxious about being fed by the robot.										
The robot is attractive from a physical standpoint.										
It would be embarrassing to be seen being fed by the robot.										
Being fed by the robot would be an invasion of my privacy.										

11. How likely do you think it is that you will need help with eating at some point in the future?
    (cross-mark <u>one</u> point on the sliding % scale below)

    0%----------100%

The following questions are about your attitudes and views toward technology in general.
To what extent do you believe that technology…
(check <u>one</u> box for each item below; 1 – Not At All; 10 – Completely)

	1	2	3	4	5	6	7	8	9	10
a. Makes life easy and convenient										
b. Makes life complicated										
c. Gives people control over their daily lives										
d. Makes people dependent										
e. Makes life comfortable										
f. Makes life stressful										
g. Brings people together										
h. Makes people isolated										
i. Increases personal safety and security										
j. Reduces privacy										

If you were considering using a particular technology to assist you with important daily tasks, how important would each of the following factors be to you in deciding whether or not to use it?
(check <u>one</u> box for each item below; 1 – Not At All Important; 10 – Extremely Important)

	1	2	3	4	5	6	7	8	9	10
a. How well it meets your needs										
b. Ease of use										
c. Cost										
d. The way it looks (attractiveness)										
e. How visible it is to others										
f. How it affects your privacy										
g. How safe it is to use										

Background

Please answer the following questions. All of your answers will be treated confidentially. **If there is a question you do not wish to answer, please leave it blank and go on to the next question.** Thank you in advance for your help.

Gender: □ Male □ Female

Age: _____

What is your highest level of education?

- □ No formal education
- □ Less than high school graduate
- □ High school graduate / GED
- □ Vocational training
- □ Some college / Associate's degree
- □ Bachelor's degree (BA, BS)
- □ Master's degree (or other post-graduate training)
- □ Doctoral degree (PhD, MD, EdD, DDS, JD, etc.)

Current marital status

- □ Single
- □ Married
- □ Separated
- □ Divorced
- □ Widowed
- □ Other (please specify) _____

Do you consider yourself Hispanic or Latino?

- □ Yes
- □ No

How would you describe your primary racial group?

- □ No primary group
- □ White Caucasian
- □ Black / African American
- □ Asian
- □ American Indian / Alaska Native
- □ Native Hawaiian / Pacific Islander
- □ Multi-racial
- □ Other (please specify) _____

Which category best describes your yearly household income? (Do not give the dollar amount, just check the category.)

- □ Less than $5,000
- □ $5,000-$9,999
- □ $10,000-$14,999
- □ $15,000-$19,999
- □ $20,000-$29,999

- □ $30,000-$39,999
- □ $40,000-$49,999
- □ $50,000-$59,999
- □ $60,000-$69,999
- □ $70,000-$99,999
- □ $100,000 or more
- □ Do not know for certain
- □ Do not wish to answer

What is your primary occupational status?

- □ Work full-time
- □ Work part-time
- □ Student
- □ Homemaker
- □ Retired
- □ Volunteer worker
- □ Seeking employment, laid off, etc.
- □ Other (please specify) _____

Have you ever interacted with anyone (e.g., family member, friend, co-worker) who needed assistance with eating? □ Yes □ No

Do you know anyone (family, friend, co-worker), who because of a health problem, needs assistance with (Check one or many):

- □ Bathing
- □ Dressing
- □ Grooming (e.g., shaving, brushing teeth)
- □ Feeding
- □ Taking medications
- □ Completing other treatments (e.g., exercise, speech therapy, special diet)
- □ Transferring in and out of bed or chair
- □ Walking
- □ Preparing meals
- □ Doing laundry
- □ Cleaning
- □ Shopping
- □ Transportation
- □ Going to medical appointments
- □ Other (please specify) _____

Have you ever interacted with a robot before? □ Yes □ No
(If yes), What kind of robot was it? What was the name and what did you do with the robot?

_____

Bibliography

[1] D.L. Allsop, T.R. Perl, and C.Y. Warner. Force/Deflection and Fracture Characteristics of the Temporor-Parietal Region of the Human Head. 1991.

[2] D.L. Allsop, C.Y. Warner, M.G. Wille, D.C. Schneider, and A.M. Nahum. Facial Impact Response–A Comparison of the Hybrid III Dummy and Human Cadaver. 1988.

[3] I. Asimov. *The Caves of Steel*. 1954.

[4] C.G. Atkeson, A.W. Moore, and S. Schaal. Locally weighted learning. *Artificial Intell. Rev.*, 11(1):11–73, 1997.

[5] R. Baldur and W. Blach. *Inflatable manipulator*. Society of Manufacturing Engineers, 1985.

[6] E. Barbieri and U. Ozguner. A new minimum-time control law for a one-mode model of a flexible slewing structure. *IEEE Transactions on Automatic Control*, 38(1):142–146, 1993.

[7] Luca Bascetta and P Rocco. Task space visual servoing of eye-in-hand flexible manipulators. In *Advanced Intelligent Mechatronics, 2003. AIM 2003. Proceedings. 2003 IEEE/ASME International Conference on*, volume 2, pages 1442–1448. IEEE, 2003.

[8] A. Bicchi and G. Tonietti. Fast and soft-arm tactics. *IEEE Robot. Autom. Mag.*, 11(2):22–33, 2004.

[9] J.N. Bricout, J.C. Debus, and P. Micheau. A finite element model for the dynamics of flexible manipulators. *Mech. Mach. Theory.*, 25(1):119–128, 1990.

[10] Samuel R Buss. Introduction to inverse kinematics with jacobian transpose, pseudoinverse and damped least squares methods. *IEEE Journal of Robotics and Automation*, 17, 2004.

[11] R.H. Cannon Jr and E. Schmitz. Initial experiments on the end-point control of a flexible one-link robot. *The International Journal of Robotics Research*, 3(3):62, 1984.

[12] J.L. Chang and Y.P. Chen. Force control of a single-link flexible arm using sliding-mode theory. *Journal of vibration and control*, 4(2):187, 1998.

[13] B.C. Chiou and M. Shahinpoor. Dynamic stability analysis of a one-link force-controlled flexible manipulator. *Journal of robotic systems*, 5(5):443–451, 2007.

[14] G.S. Chirikjian. Hyper-redundant manipulator dynamics: A continuum approximation. *Advanced Robotics*, 9(3):217–243, 1994.

[15] G.S. Chirikjian and J.W. Burdick. Kinematics of hyper-redundant manipulators. In *Proc. 2nd International Workshop on Advances in Robot Kinematics, Linz*, page 392, 1990.

[16] G.S. Chirikjian and J.W. Burdick. A modal approach to hyper-redundant manipulator kinematics. *IEEE Trans. Robot. Autom.*, 10(3):343–354, Jun 1994.

[17] G.S. Chirikjian and JW Burdick. Design and Experiments with a 30 DOF Robot. In *Robotics and Automation, 1993. Proceedings., 1993 IEEE International Conference on*, pages 113–119. IEEE, 2002.

[18] Wonseok Choi and Nancy B Powell. Three dimensional seamless garment knitting on v-bed flat knitting machines. *Journal of Textile and Apparel, Technology and Management*, 4(3):1–33, 2005.

[19] C.P. Chou and B. Hannaford. Measurement and modeling of mckibben pneumatic artificial muscles. *Robotics and Automation, IEEE Transactions on*, 12(1):90–102, 1996.

[20] W.S. Cleveland and S.J. Devlin. Locally weighted regression: an approach to regression analysis by local fitting. *J. Amer. Stat. Assoc.*, 83(403):596–610, 1988.

[21] RL Comer and S. Levy. Deflections of an inflated circular-cylindrical cantilever beam. *AIAA journal*, 1(7), 2012.

[22] J.J. Craig. *Introduction to Robotics*. Addison-Wesley Reading, MA, 1989.

[23] F. Daerden and D. Lefeber. Pneumatic artificial muscles: actuators for robotics and automation. *European journal of mechanical and environmental engineering*, 47(1):11–21, 2002.

[24] A. De Luca and B. Siciliano. Closed-form dynamic model of planar multilink lightweight robots. *Systems, Man and Cybernetics, IEEE Transactions on*, 21(4):826–839, 2002.

[25] S.K. Dwivedy and P. Eberhard. Dynamic analysis of flexible manipulators, a literature review. *Mechanism and Machine Theory*, 41(7):749–777, 2006.

[26] S. Eppinger and W. Seering. Understanding bandwidth limitations in robot force control. In *IEEE International Conference on Robotics and Automation*, volume 4, pages 904 – 909, Mar 1987.

[27] RL Farrenkopf. Optimal open-loop maneuver profiles for flexible spacecraft. *Journal of Guidance, Control, and Dynamics*, 2(6):491–498, 1979.

[28] Festo AG. *Festo Handling Assistant*.

[29] WB Fichter. *A theory for inflated thin-wall cylindrical beams*. National Aeronautics and Space Administration, 1966.

[30] Javad Foroughi, Geoffrey M Spinks, Gordon G Wallace, Jiyoung Oh, Mikhail E Kozlov, Shaoli Fang, Tissaphern Mirfakhrai, John DW Madden, Min Kyoon Shin, Seon Jeong Kim, et al. Torsional carbon nanotube artificial muscles. *Science*, 334(6055):494–497, 2011.

[31] EC Framework. Improved Frontal Impact Protection through a World Frontal Impact Dummy. *Project No. GRD1 1999*, 10559, 2003.

[32] G. Gilardi and I. Sharf. Literature survey of contact dynamics modelling. *Mechanism and Machine Theory*, 37(10):1213–1239, 2002.

[33] M.D. Gilchrist, S. Keenan, M. Curtis, M. Cassidy, G. Byrne, and M. Destrade. Measuring knife stab penetration into skin simulant using a novel biaxial tension device. *Forensic science international*, 177(1):52–65, 2008.

[34] M.D. Gilchrist, S. Keenan, M. Curtis, M. Cassidy, G. Byrne, and M. Destrade. Mechanics of Stabbing: Biaxial Measurement of Knife Stab Penetration of Skin Simulant. *Imprint*, 2008.

[35] W. Goldsmith. *Impact: the theory and physical behaviour of colliding solids*. Dover Pubns, 2001.

[36] I.A. Gravagne, C.D. Rahn, and I.D. Walker. Large deflection dynamics and control for planar continuum robots. *IEEE/ASME transactions on mechatronics*, 8(2):299–307, 2003.

[37] I.A. Gravagne and I.D. Walker. Kinematic transformations for remotely-actuated planar continuum. In *IEEE Conf. on Robotics and Automation*, pages 19–26, 2000.

[38] I.A. Gravagne and I.D. Walker. On the kinematics of remotely-actuated continuum robots. In *IEEE International Conference on Robotics and Automation, 2000. Proceedings. ICRA'00*, volume 3, 2000.

[39] I.A. Gravagne and I.D. Walker. On the kinematics of remotely-actuated continuum robots. In *Proc. 2000 IEEE Int. Conf. Robot. Autom. (ICRA)*, volume 3, pages 2544–2550, 2000.

[40] S. Haddadin, A. Albu-Schaffer, and G. Hirzinger. Safe physical human-robot interaction: measurements, analysis & new insights. In *2007 Int. Symp. Robot. Res. (ISRR), Hiroshima, Japan*, 2007.

[41] Sami Haddadin, Alin Albu-Schaffer, and Gerd Hirzinger. Requirements for Safe Robots: Measurements, Analysis and New Insights. *The International Journal of Robotics Research*, 28(11-12):1507–1527, 2009.

[42] S.V. Hainsworth, R.J. Delaney, and G.N. Rutty. How sharp is sharp? Towards quantification of the sharpness and penetration ability of kitchen knives used in stabbings. *International Journal of Legal Medicine*, 122(4):281–291, 2008.

[43] MW Hannan and ID Walker. Analysis and initial experiments for a novel elephant's trunk robot. In *Intelligent Robots and Systems, 2000.(IROS 2000). Proceedings. 2000 IEEE/RSJ International Conference on*, volume 1, pages 330–337. IEEE, 2002.

[44] G. Hastings and W. Book. Reconstruction and robust reduced-order observation of flexible variables. In *ASME, Winter Annual Meeting, Annaheim, CA*, page 1986, 1986.

[45] G. Hastings and W. Book. Verification of a linear dynamic model for flexible robotic manipulators. In *1986 IEEE International Conference on Robotics and Automation. Proceedings*, volume 3, 1986.

[46] Chi haur Wu and Richard P. Paul. Manipulator compliance based on joint torque control. In *Decision and Control including the Symposium on Adaptive Processes, 1980 19th IEEE Conference on*, volume 19, pages 88–94, Dec. 1980.

[47] Kenneth L Hillsley and Stephen Yurkovich. Vibration control of a two-link flexible robot arm. *Dynamics and Control*, 3(3):261–280, 1993.

[48] H.O.S. Hirose, A. Ochiai, and T. Aoki. Study on Slime Robot. In *Proc. IEEE Int. Conf. Robot. Autom*, pages 2808–2813, 2004.

[49] N. Hogan and E. Colgate. *Robotics Review*. Cambridge, MA (US); MIT Press, 1989.

[50] L.L. Howell. *Compliant mechanisms*. Wiley-Interscience, 2001.

[51] LL Howell and A. Midha. A method for the design of compliant mechanisms with small-length flexural pivots. *Journal of Mechanical Design*, 116:280, 1994.

[52] L.L. Howell, A. Midha, and T.W. Norton. Evaluation of equivalent spring stiffness for use in a pseudo-rigid-body model of large-deflection compliant mechanisms. *Journal of Mechanical Design*, 118:126, 1996.

[53] J. Hurst, J. Chestnutt, and A. Rizzi. An actuator with physically variable stiffness for highly dynamic legged locomotion. In *IEEE International Conference on Robotics and Automation*, volume 5, pages 4662–4667. Citeseer, 2004.

[54] R.L. Huston and Y. Wang. Flexibility effects in multibody systems. *Computer-Aided Analysis of Rigid and Flexible Mechanical Systems*, pages 351–376, 1993.

[55] F. Ilievski, A.D. Mazzeo, R.F. Shepherd, X. Chen, and G.M. Whitesides. Soft robotics for chemists. *Angewandte Chemie*, 123(8):1930–1935, 2011.

[56] K.L. Johnson. *Contact mechanics*. Cambridge Univ Pr, 1987.

[57] Ben Jonker. A finite element dynamic analysis of spatial mechanisms with flexible links. *Computer Methods in Applied Mechanics and Engineering*, 76(1):17–40, 1989.

[58] I. Kao, K. Lynch, and J.W. Burdick. *Springer handbook of robotics*. Springer-Verlag New York Inc, 2008.

[59] Rafael Kelly. Robust asymptotically stable visual servoing of planar robots. *Robotics and Automation, IEEE Transactions on*, 12(5):759–766, 1996.

[60] Y.A. Khulief and A.A. Shabana. Impact responses of multi-body systems with consistent and lumped masses. *Journal of Sound Vibration*, 104:187–207, 1986.

[61] S. Kota, J. Joo, Z. Li, S.M. Rodgers, and J. Sniegowski. Design of compliant mechanisms: applications to MEMS. *Analog Integrated Circuits and Signal Processing*, 29(1):7–15, 2001.

[62] Rebecca K Kramer, Carmel Majidi, Ranjana Sahai, and Robert J Wood. Soft curvature sensors for joint angle proprioception. In *Intelligent Robots and Systems (IROS), 2011 IEEE/RSJ International Conference on*, pages 1919–1926. IEEE, 2011.

[63] Konstantinos J Kyriakopoulos and George N Saridis. Minimum jerk path generation. In *Robotics and Automation, 1988. Proceedings., 1988 IEEE International Conference on*, pages 364–369. IEEE, 1988.

[64] A. V. Le and C. Wielgosz. Bending and buckling of inflatable beams: Some new theoretical results. *J. Thin-Walled Struct.*, 43(8):1166–1187, 2005.

[65] YF Li and XB Chen. End-point sensing and state observation of a flexible-link robot. *Mechatronics, IEEE/ASME Transactions on*, 6(3):351–356, 2001.

[66] Sonja Macfarlane and Elizabeth A Croft. Jerk-bounded manipulator trajectory planning: design for real-time applications. *Robotics and Automation, IEEE Transactions on*, 19(1):42–52, 2003.

[67] Sebastian OH Madgwick, Andrew JL Harrison, and Ravi Vaidyanathan. Estimation of imu and marg orientation using a gradient descent algorithm. In *Rehabilitation Robotics (ICORR), 2011 IEEE International Conference on*, pages 1–7. IEEE, 2011.

[68] JA Main, SW Peterson, and AM Strauss. Load-deflection behavior of space-based inflatable fabric beams. *Journal of Aerospace Engineering*, 7(2):225–238, 1994.

[69] D. Maruyama, H. Kimura, M. Koseki, and N. Inou. Driving force and structural strength evaluation of a flexible mechanical system with a hydrostatic skeleton. *Journal of Zhejiang University-Science A*, 11(4):255–262, 2010.

[70] M.T. Mason. Compliance and Force Control. *IEEE Trans. Sys. Man Cyb*, 6:418–432, 1981.

[71] C.T. McCarthy, A.N. Annaidh, and M.D. Gilchrist. On the sharpness of straight edge blades in cutting soft solids: Part II-Analysis of blade geometry. *Engineering Fracture Mechanics*, 2009.

[72] C.T. McCarthy, M. Hussey, and M.D. Gilchrist. On the sharpness of straight edge blades in cutting soft solids: Part I–indentation experiments. *Engineering Fracture Mechanics*, 74(14):2205–2224, 2007.

[73] W. McMahan, B.A. Jones, and I.D. Walker. Design and implementation of a multi-section continuum robot: Air-Octor. In *2005 IEEE/RSJ International Conference on Intelligent Robots and Systems, 2005.(IROS 2005)*, pages 2578–2585, 2005.

[74] J. Melvin. Human tolerance to impact conditions as related to motor vehicle design. *SAE J885 APR80*, 1980.

[75] H. Moulin and E. Bayo. On the accuracy of end-point trajectory tracking for flexible arms by noncausal inverse dynamic solutions. *Journal of Dynamic Systems, Measurement, and Control*, 113:320, 1991.

[76] A. Mozeika, E. Steltz, and H.M. Jaeger. The first steps of a robot based on jamming skin enabled locomotion. In *Proceedings of the 2009 IEEE/RSJ international conference on Intelligent robots and systems*, pages 408–409. IEEE Press, 2009.

[77] T. Mukai, M. Onishi, T. Odashima, S. Hirano, and Z. Luo. Development of the Tactile Sensor System of a Human-Interactive Robot" RI-MAN". *IEEE Transactions on Robotics*, 24(2):505, 2008.

[78] T. Mukai, M. Onishi, T. Odashima, S. Hirano, and Zhiwei Luo. Development of the tactile sensor system of a human-interactive robot ri-man. *IEEE. Trans. Robot.*, 24(2):505–512, April 2008.

[79] S. Nagarajan and D.A. Turcic. Lagrangian Formulation of the Equations of Motion for Elastic Mechanisms With Mutual Dependence Between Rigid Body and Elastic Motions: Part II-System Equations. *Journal of Dynamic Systems, Measurement, and Control*, 112:215, 1990.

[80] A. Needleman. Inflation of spherical rubber balloons. *International Journal of Solids and Structures*, 13(5):409–421, 1977.

[81] I. Newton, T. Leseur, and F. Jacquier. Philosophiae naturalis principia mathematica. 1833.

[82] Celia M Oakley and Robert H Cannon. End-point control of a two-link manipulator with a very flexible forearm: Issues and experiments. In *American Control Conference, 1989*, pages 1381–1389. IEEE, 1989.

[83] S. Oberer and R.D. Schraft. Robot-dummy crash tests for robot safety assessment. In *Robotics and Automation, 2007 IEEE International Conference on*, pages 2934–2939, April 2007.

[84] P.T. O'Callaghan, M.D. Jones, D.S. James, S. Leadbeatter, C.A. Holt, and L.D.M. Nokes. Dynamics of stab wounds: force required for penetration of various cadaveric human tissues. *Forensic science international*, 104(2-3):173–178, 1999.

[85] L Ott, Ph Zanne, Fl Nageotte, M de Mathelin, and J Gangloff. Physiological motion rejection in flexible endoscopy using visual servoing. In *Robotics and Automation, 2008. ICRA 2008. IEEE International Conference on*, pages 2928–2933. IEEE, 2008.

[86] E. Paljug, T. Ohm, and S. Hayati. The JPL Serpentine Robot: a 12-DOF system for inspection. In *Robotics and Automation, 1995. Proceedings., 1995 IEEE International Conference on*, volume 3, pages 3143–3148. IEEE, 2002.

[87] L.Y. Pao. Characteristics of the time-optimal control of flexible structures with damping. In *IEEE Conference on Control Applications*, pages 1299–1304. Citeseer, 1994.

[88] Yong-Lae Park, Carmel Majidi, Rebecca Kramer, Phillipe Bérard, and Robert J Wood. Hyperelastic pressure sensing with a liquid-embedded elastomer. *Journal of Micromechanics and Microengineering*, 20(12):125029, 2010.

[89] G.A. Pratt and M.M. Williamson. Series elastic actuators. In *Proc. 1995 IEEE/RSJ Int. Conf. Intell. Robots Syst. (IROS) - 'Human Robot Interaction and Cooperative Robots'*, volume 1, pages 399–406, Aug 1995.

[90] G.A. Pratt and M.M. Williamson. Series elastic actuators. In *Proceedings of the IEEE/RSJ International Conference on Intelligent Robots and Systems (IROS-95)*, volume 1, pages 399–406, 1995.

[91] M.H. Raibert and J.J. Craig. Hybrid position/force control of manipulators. *Journal of Dynamic Systems, Measurement, and Control*, 102(127):126–133, 1981.

[92] R.D. Robinett, C. Dohrmann, G.R. Eisler, J. Feddema, G.G. Parker, D.G. Wilson, and D. Stokes. *Flexible robot dynamics and controls*. Kluwer Academic Pub, 2002.

[93] G. Robinson and JBC Davies. Continuum robots-a state of the art. In *Robotics and Automation, 1999. Proceedings. 1999 IEEE International Conference on*, volume 4, pages 2849–2854. IEEE, 2002.

[94] N. Salomonski, M. Shoham, and G. Grossman. Light robot arm based on inflatable structure. *CIRP Annals-Manufacturing Technology*, 44(1):87–90, 1995.

[95] S. Sanan, P. Lynn, and S. T. Griffith. Pneumatic torsional actuators for inflatable robots. In *submitted*, 2012.

[96] S. Sanan, P. Lynn, and S. T. Griffith. Pneuarm: An anthropomorphic pneumatically actuated inflatable manipulator. *submitted to the IEEE Transactions on Robotics*, 2013.

[97] S. Sanan, J.B. Moidel, and C.G. Atkeson. Robots with Inflatable Links. In *IEEE/RSJ International Conference on Intelligent Robots and Systems, IROS 2009*, pages 4331–4336, 2009.

[98] R. Schiavi, G. Grioli, S. Sen, and A. Bicchi. Vsa-ii: a novel prototype of variable stiffness actuator for safe and performing robots interacting with humans. In *IEEE International Conference on Robotics and Automation*, pages 2171 –2176, May 2008.

[99] W.O Schiehlen and J. Rauh. Modeling of flexible multibeam systems by rigid-elastic superelements. *Revista Brasiliera de Ciencias Mecanicas*, 8(2), 1986.

[100] HF Schulte. The characteristics of the mckibben artificial muscle. *The application of external power in prosthetics and orthotics*, pages 94–115, 1961.

[101] A.A. Shabana. Flexible multibody dynamics: review of past and recent developments. *Multibody system dynamics*, 1(2):189–222, 1997.

[102] Robert F Shepherd, Filip Ilievski, Wonjae Choi, Stephen A Morin, Adam A Stokes, Aaron D Mazzeo, Xin Chen, Michael Wang, and George M Whitesides. Multigait soft robot. *Proceedings of the National Academy of Sciences*, 108(51):20400–20403, 2011.

[103] Bruno Siciliano. An inverse kinematics scheme for a flexible arm in contact with a compliant surface. In *Decision and Control, 1998. Proceedings of the 37th IEEE Conference on*, volume 4, pages 3617–3622. IEEE, 1998.

[104] Bruno Siciliano. Closed-loop inverse kinematics algorithm for constrained flexible manipulators under gravity. *Journal of Robotic Systems*, 16(6):353–362, 1999.

[105] N. Simaan, R. Taylor, and P. Flint. A dexterous system for laryngeal surgery. In *Proc. 2004 IEEE Int. Conf. Robot. Autom. (ICRA)*, volume 1, pages 351–357, April-1 May 2004.

[106] N.C. Singer and W.P. Seering. Preshaping command inputs to reduce system vibration. *ASME, Transactions, Journal of Dynamic Systems, Measurement, and Control*, 112:76–82, 1990.

[107] G. Singh, P. Kabamba, and N. McClamroch. Planar, time-optimal, rest-to-rest slewing maneuvers of flexible spacecraft. *Journal of Guidance, Control, and Dynamics*, 12:71–81, 1989.

[108] W. Singhose, W. Seering, and N. Singer. Residual vibration reduction using vector diagrams to generate shaped inputs. *Journal of Mechanical Design*, 116:654, 1994.

[109] J.J.E. Slotine, W. Li, et al. *Applied nonlinear control*, volume 461. Prentice hall Englewood Cliffs, NJ, 1991.

[110] Otto JM Smith. Posicast control of damped oscillatory systems. *Proceedings of the IRE*, 45(9):1249–1255, 1957.

[111] Peter Staufer and Hubert Gattringer. Passivity-based tracking control of a flexible link robot. In *Multibody System Dynamics, Robotics and Control*, pages 95–112. Springer, 2013.

[112] W.J. Stronge. *Impact mechanics*. Cambridge Univ. Pr., 2000.

[113] J.D. Suhey, N.H. Kim, and C. Niezrecki. Numerical modeling and design of inflatable structures–application to open-ocean-aquaculture cages. *Aquacultural Engineering*, 33(4):285–303, 2005.

[114] K. Suzumori, S. Iikura, and H. Tanaka. Development of flexible microactuator and its applications torobotic mechanisms. In *Proc. 1991 IEEE Int. Conf. Robot. Autom. (ICRA)*, pages 1622–1627, 1991.

[115] R.J. Theodore and A. Ghosal. Comparison of the assumed modes and finite element models for flexible multilink manipulators. *The International Journal of Robotics Research*, 14(2):91, 1995.

[116] William T. Thomson. *Theory of Vibration with Applications*. Prentice Hall, 1988.

[117] M.O. Tokhi, Z. Mohamed, and A.K.M. Azad. Finite difference and finite element approaches to dynamic modelling of a flexible manipulator. *Proceedings of the Institution of Mechanical Engineers, Part I: Journal of Systems and Control Engineering*, 211(2):145–156, 1997.

[118] Azad A. K. M. Tokhi M. O. *Flexible robot manipulators: modelling, simulation and control*. IET, 2008, 2008.

[119] G. Tonietti, R. Schiavi, and A. Bicchi. Design and control of a variable stiffness actuator for safe and fast physical human/robot interaction. In *IEEE International Conference on Robotics and Automation*, volume 1, page 526. IEEE; 1999, 2005.

[120] Anthony P Tzes and Stephen Yurkovich. Adaptive precompensators for flexible-link manipulator control. In *Decision and Control, 1989., Proceedings of the 28th IEEE Conference on*, pages 2083–2088. IEEE, 1989.

[121] R. Van Ham, B. Vanderborght, M. Van Damme, B. Verrelst, and D. Lefeber. MACCEPA, the mechanically adjustable compliance and controllable equilibrium position actuator: Design and implementation in a biped robot. *Robotics and Autonomous Systems*, 55(10):761–768, 2007.

[122] S.L. Veldman. *Design and analysis methodologies for inflated beams*. 2005.

[123] J. Versace. A review of the severity index. 1971.

[124] L. Villani and J. D. Schutter. *Springer handbook of robotics*. Springer-Verlag New York Inc, 2008.

[125] S Voisembert, A Riwan, N Mechbal, and A Barraco. A novel inflatable robot with constant and continuous volume. In *Robotics and Automation (ICRA), 2011 IEEE International Conference on*, pages 5843–5848. IEEE, 2011.

[126] ID Walker. Some issues in creating invertebraterobots. In *Proceedings of the International Symposium on Adaptive Motion of Animals and Machines*. Citeseer, 2000.

[127] P.K.C. Wang and J.D. Wei. Vibrations in a moving flexible robot arm. *Journal of sound and vibration*, 116(1):149–160, 1987.

[128] Q.F. Wei, P.S. Krishnaprasad, and W.P. Dayawansa. Modeling of impact on a flexible beam. 1993.

[129] D.E. Whitney. Historical perspective and state of the art in robot force control. *The International Journal of Robotics Research*, 6(1):3, 1987.

[130] A. Wolf, HB Brown, R. Casciola, A. Costa, M. Schwerin, E. Shamas, and H. Choset. A mobile hyper redundant mechanism for search and rescue tasks. In *Intelligent Robots and Systems, 2003.(IROS 2003). Proceedings. 2003 IEEE/RSJ International Conference on*, volume 3, pages 2889–2895. IEEE, 2004.

[131] S. Wolf and G. Hirzinger. A new variable stiffness design: matching requirements of the next robot generation. In *IEEE International Conference on Robotics and Automation*, pages 19–23, 2008.

[132] KS Yeung and YP Chen. Regulation of a one-link flexible robot arm using sliding-mode technique. *International Journal of Control*, 49(6):1965–1978, 1989.

[133] K.S. Yeung and Y.P. Chen. Sliding-mode controller design of a single-link flexible manipulator under gravity. *International Journal of Control*, 52(1):101–117, 1990.

[134] A.S. Yigit, A.G. Ulsoy, and R.A. Scott. Dynamics of a radially rotating beam with impact, Part 1: theoretical and computational model. *Journal of Vibration and Acoustics*, 112:65, 1990.

[135] A.S. Yigit, A.G. Ulsoy, and R.A. Scott. Dynamics of a radially rotating beam with impact, part 2: experimental and simulation results. *Journal of Vibration and Acoustics*, 112:71, 1990.

[136] B.S. Yuan, J.D. Huggins, and W.J. Book. Small motion experiments on a large flexible arm with strain feedback. In *1989 American Control Conference, 8 th, Pittsburgh, PA*, pages 2091–2095, 1989.

[137] M. Zinn, O. Khatib, and B. Roth. A new actuation approach for human friendly robot design. In *Proc. 2004 IEEE Int. Conf. Robot. Autom. (ICRA)*, volume 1, pages 249–254, April-1 May 2004.